Theoretical Investigations of Properties of Low Dimensional Systems and Nanomaterials

A Thesis

Submitted For the Degree of

DOCTOR OF PHILOSOPHY

by

Prasenjit Ghosh

THEORETICAL SCIENCES UNIT
JAWAHARLAL NEHRU CENTRE FOR ADVANCED SCIENTIFIC RESEARCH
Bangalore – 560 064
(A Deemed University)

DECEMBER 2007

DECLARATION

I hereby declare that the matter embodied in the thesis entitled "**Theoretical Investigations of Properties of Low Dimensional Systems and Nanomaterials**" is the result of investigations carried out by me at the Theoretical Sciences Unit, Jawaharlal Nehru Centre for Advanced Scientific Research, Bangalore, India under the supervision of Prof. Umesh V. Waghmare and Prof. Shobhana Narasimhan and that it has not been submitted elsewhere for the award of any degree or diploma.

In keeping with the general practice in reporting scientific observations, due acknowledgement has been made whenever the work described is based on the findings of other investigators.

Prasenjit Ghosh

CERTIFICATE

We hereby certify that the matter embodied in this thesis entitled "**Theoretical Investigations of Properties of Low Dimensional Systems and Nanomaterials**" has been carried out by Mr. Prasenjit Ghosh at the Theoretical Sciences Unit, Jawaharlal Nehru Centre for Advanced Scientific Research, Bangalore, India under our supervision and that it has not been submitted elsewhere for the award of any degree or diploma.

Prof. Umesh V. Waghmare Prof. Shobhana Narasimhan

(Research Supervisors)

Acknowledgements

First of all I would like to thank my parents and my wife for providing me support and staying beside me throughout.

I would like to thank my thesis advisors, Prof. Shobhana Narasimhan and Prof. Umesh V. Waghmare, not only for introducing me to several interesting problems, but also for the encouraging scientific discussion. I would also like to thank them for their support throughout the entire tenure.

My respectful gratitude towards Prof. M. R. S. Rao, the President of JNCASR and Prof. C. N. R. Rao, the founding president of JNCASR for providing excellent research facilities and creating a good scientific environment.

Many thanks to Prof. Rahul Pandit, Prof. H. R. Krishnamurthy, Prof. Srikanth Sastry, Prof. Swapan K. Pati, Dr. N. S. Vidhyadhiraja, Prof. Chandrabhas Narayana, Prof. S. Balasubramanian, Prof. K. S. Narayan Prof. Rama Govindrajan for all the things they have taught me through the courses they offered.

Also I would like to acknowledge my collaborators Prof. Sir D. A. King and Dr. Stephen J. Jenkins, Department of Chemistry, University of Cambridge and Prof. Stefano de Gironcoli and Dr. Pushpa Raghani, SISSA.

I would like to thank CSIR, India for providing me with a research scholarship.

Nonetheless I would also like to thank the staffs of the computer laboratory,

library, academic section and the administrative office.

Last but not the least my heartiest thanks to all my friends and my colleagues.

Synopsis

The work presented in this thesis involves theoretical investigations of nano-structured materials and low-dimensional systems. Nano-structured materials form a broad class of materials in which the building blocks are nanometer sized particles, whose size determines the properties of these materials. These materials do not have any long range order, making it unfeasible to perform quantum mechanical calculations. We have replaced the actual system by a model system wherein interatomic interactions have been described by a classical potential. We have also studied nano-materials and low-dimensional systems: clusters (zero-dimensional) of Rh and Te, nanowires (one-dimensional) of Te and {100} surfaces (two-dimensional) of Ir and Rh. The study of such systems is motivated by interesting experimental findings and the fundamental physics involved in the understanding of their properties. For the low-dimensional systems we have performed purely quantum mechanical calculations using density functional theory (DFT) and density functional perturbation theory (DFPT).

The thesis is divided into eight chapters.

In Chapter 1 we motivate why low-dimensional and nano-structured materials are interesting to study.

The second chapter contains brief descriptions of DFT and DFPT.

Bulk Te possesses interesting optical properties and an intriguing structure. It consists of parallel helices of Te stacked on a triangular lattice in a plane perpendicular to the helical axis. The aim is to study how the properties of the

nanowires vary as a function of their diameter. In the third chapter we present a comparative study of atomic and electronic structures, Young's modulus and optical conductivity of trigonal bulk tellurium and its nanowires of different diameters. In Te nanowires, interhelical distances change by about 1% of their bulk value due to rearrangement of atoms at the surfaces. Due to a decrease in the overlap between electronic states of neighboring helices, the band gap of nanowires increases with reducing diameter, whereas their Young's modulus decreases. The optical conductivity of nanowires depends on their diameter and exhibits a marked anisotropy due to quantum confinement of electronic states in the plane perpendicular to the helical axis.

In Chapter 4 we present first-principles investigations of the origin of stability of the helical structure of Te through determination of the structure and energetics of its clusters, the largest one comprising of twelve Te atoms, and helical forms. Among all the clusters we have studied, Te_8 with a closed ring-like helical structure is the most stable one; it is even more stable than an infinitely long helix. The stability of the Te structures depends on the Te-Te-Te bond angle and coordination number of Te atoms. Wannier function-based analysis of chemical bonding in Te-helix reveals *sp* hybridization giving rise to a σ and a three-centre-π-like bonding between neighboring Te atoms. While the former stabilizes a two-fold coordination in the helix, the latter stabilizes a specific Te-Te-Te angle. As a result, the helical structure is stabilized and closed loops of helices are more stable than the open helical chains. A comparative study of the vibrational modes of bulk Te and that of a single helix shows that the rotational mode of bulk Te is significantly softened in the case of a single helix due to the absence of inter-helical interactions in the latter. We estimate the inter-helical interaction strength in bulk Te to be about 3.0 meV/helix. Relative energies of an infinite helix of Te with respect to a linear chain show that the coupling of transverse chiral acoustic wave with strain plays a crucial role in the formation of the helix. We find that bulk Te is more

stable to slip deformation than stretch deformation.

CO adsorption and oxidation on Ir and Pt {100} surfaces are of great industrial significance and present some intriguing features. The study of the adsorption of CO on unreconstructed and reconstructed Ir{100}, using a combination of DFT and thermodynamics, to determine the relative stability of the two phases as a function of CO coverage, temperature and pressure has been presented in Chapter 5. At zero temperature, the (5×1) reconstruction becomes less stable than the unreconstructed (1×1) surface when the CO coverage exceeds a critical value of 0.09 ML. The higher heat of CO adsorption on the growing unreconstructed surface (including the cost of lifting of the reconstruction) compared to that of the reconstructed one provides the driving force for lifting of the reconstruction. At all temperatures and pressures, we find only two possible stable states: 0.5 ML CO c(2×2) overlayer on the (1×1) substrate, and the clean (5×1) reconstructed surface. All these results are in good agreement with experimental observations.

As a part of an effort to determine the relative importance of charge transfer, strain, coordination number and magnetism in determining catalytic barriers, we have studied NO adsorption on Rh{100} surfaces, the results of which are presented in Chapter 6. We have studied four systems, namely, (i) Rh{100} at Rh lattice constant, (ii) Rh{100} at MgO lattice constant (about 10% strain), (iii) 1 ML of Rh on an MgO{100} substrate at Rh lattice constant, and (iv) 1 ML of Rh on an MgO{100} substrate at MgO lattice constant. We find that for Rh supported on an MgO substrate charge transfer is insignificant. For the surfaces which are magnetic, we find that upon adsorption, magnetism is substantially quenched on the Rh atoms to which NO binds. Our results suggest that magnetism weakens the metal-adsorbate bond. From our studies we find that NO adsorption energy is mainly affected by strain and the number of nearest meighbor Rh atoms. An effective coordination number of the Rh

atoms on the different systems has been calculated. It has been found that the NO adsorption energy increases almost linearly as effective coordination number decreases.

In continuation of our efforts to understand the effects of coordination number and magnetism on catalytic barriers, we have studied the adsorption of NO on small Rh clusters, containing one to five atoms, using density functional theory in both spin-polarized and non-spin polarized forms. We find that NO bonds more strongly to Rh clusters than it does to Rh(100) or Rh(111); however, it also quenches the magnetism of the clusters. This (local) effect results in reducing the magnitude of the adsorption energy, and also washes out the clear size-dependent trend observed in the non-magnetic case. Our results illustrate the competition present between the tendencies to bond and to magnetize, in small clusters.

Motivated by the unusual soft mode anomalies in the relaxor ferroelectrics, we present, in the last chapter, a numerical study of vibrational excitations of a disordered lattice model with chemical order on the nano-scale. An Ioffe-Regel crossover in the acoustic modes has been found which separates the propagating low-frequency modes from the intermediate frequency diffusons and localized modes at the high-frequency end of the spectrum. At a fixed degree of disorder, we observe an increasing uncertainty in the momentum of long wave-length optical modes with decrease in the size of the nano-ordered regions, as a result of strong mixing between acoustic and optical modes, believed to be central to the model of waterfall phonon anomalies.

Abbreviations

0D : zero-dimensional

1D : one-dimensional

2D : two-dimensional

3D : three-dimensional

e : charge of an electron

fcc : face centered cube

hcp : hexagonal close packed

BE : binding energy

BFGS : Broyden, Fletcher, Goldfarb, Shannon

BO : Born and Oppenheimer

CB : conduction band

DFT : density funtional theory

DFPT : density functional perturbation theory

DOF : degrees of freedom

DOS : density of states

EELS : energy loss spectroscopy

EXAFS : extended X-ray absorption fine structure spectroscopy

FLAPW : full potential linearized augmented-plane-wave

FWHM : full width at half maximum

GGA : feneralized gradient approximation

HK : Hohenberg and Kohn

HREELS : high resolution electron energy loss spectroscopy

I-R : Ioffe-Regel

IBZ : irreducible Brillouin zone

IPR : inverse participation ratio

JDOS : joint density of states

LA : longitudinal acoustic

LDA : local density approximation

LEED : low energy electron diffraction

LO : longitudinal optic

LSD : level spacing distribution

ML : monolayer

NOR : nano-ordered region

NSP : non-spin-polarized

PBE : Perdew, Burke and Ernzerhof exchange-correlation functional

PES : potential energy surface

PMN : $PbMg_{\frac{1}{3}}Nb_{\frac{2}{3}}O_3$

PNR : polar nano-regions

PSN : $PbSc_{\frac{1}{2}}Nb_{\frac{1}{2}}O_3$

PW91 : Perdew and Wang exchange-correlation functional

RAIRS : reflection absorption infrared spectroscopy

SFEM : scanning field electron emission microscope

SP : spin-polarized

STM : scanning tunnelling microscopy

Te-h : a single Te helix

Te-lc : a linear chain of Te atoms

Te-w1 : Te wire with one shell

Te-w2 : Te wire with two shells

TA : transverse acoustic

TBS : transformed band structure

TO : transverse optic

TPD : temperature programmed desorption

VB : valence band

Symbols

α, β : Cartesian indices

$\vec{\alpha}$: eigenvector of real space dynamical matrix

a : lattice spacing

A : area

$\chi_n(\mathbf{R})$: coefficients of the electronic states $\Psi_n(\mathbf{R}, \mathbf{r})$

δ : disorder parameter

d : bond length

d^i_{rum} : rumpling parameter

ϵ : dielectric constant

$\epsilon^s_{\alpha\beta}$: strain tensor

$\epsilon^{\text{hom}}_{\text{XC}}(n(\mathbf{r}))$: exchange-correlation density at $\mathbf{r}$ of a homogeneous electron gas of density $n(\mathbf{r})$

ε_n : energy eigenfunctions of $\hat{H}$

E : total energy of a system

E_{ads} : adsorption energy

E_{bind} : binding energy

E_{cut} : Plane wave energy cut-off

E_{e-e} : electron-electron interaction energy

$E_n(\mathbf{R})$: BO potential energy surface

$E_{tot}[n]$: Total energy functional

E_{Ewald} : nuclear-nuclear interaction for a particular ionic configuration

E_{HK} : HK functional

$E_{\mathrm{XC}}[n]$: exchange-correlation energy

$E_{\mathrm{XC}}^{\mathrm{LDA}}$: exchange-correlation energy within the LDA

$E_{\mathrm{XC}}^{\mathrm{GGA}}$: exchange-correlation energy within the GGA

$f(\omega, \omega^{'})$: energy correlation function

f_i^k : Fermi-Dirac occupation

F : free energy

F_I : force acting on the I^{th} atom

$F_{KS}[n]$: Kohn-Sham energy functional

$F[n]$: $T[n] + E_{e-e}$

γ_{us} : unstable stacking fault energy

Γ : surface energy

$\mathbf{G}$: reciprocal lattice vector

h : Planck's constant

$\hbar$: $h/2\pi$

$\hat{H}$: Hamiltonian

H : enthalpy

κ : force constant for model I

k : force constant for model II

$\mathbf{k}$: wave vector

k_B : Boltzmann constant

μ : chemical potential

μ_B : Bohr magneton

m_e : mass of an electron

M_I : mass of nuclei

∇ : spatial derivative

$n(\mathbf{r})$: electronic charge density

$n_0(\mathbf{r})$: ground state electronic charge density

N : number of electrons

N_{eff} : effective coordination number

$\langle N_{eff} \rangle$: average coordination number

N_Z : number of nuclei

ω : frequency

Ω : volume of the unit cell

$\psi_n(\mathbf{r})$: auxiliary Kohn-Sham orbitals

$\Psi_n(\mathbf{R}, \mathbf{r})$: energy eigenvalues of $\hat{H}$

P : pressure

r_c : cut-off radius

$\mathbf{r}_i$: position of i^{th} electron

$\mathbf{R}_I$: position of I^{th} ion

R : radius of nanowire

σ : conductivity tensor

σ^s : stress tensor

S : entropy

$S_{\mathbf{k}}(\omega)$: spectral density function

θ : bond angle

Θ : coverage

T : temperature

$T[n]$: kinetic energy functional

$T_0[n]$: ground state kinetic energy functional

v_{XC} : functional derivative of the exchange-correlation energy

$v_{\text{XC}}^{\text{LDA}}$: exchange-correlation potential within LDA

$v_{\text{XC}}^{\text{GGA}}$: exchange-correlation energy within the GGA

$V_{\text{ext}}(\mathbf{r})$: external potential

V : volume

V_0 : equilibrium volume

$V_{\mathbf{R}}(\mathbf{r})$: electron-nucleus interaction potential

$V_{SCF}(\mathbf{r})$: effective potential acting on non-interacting potential

Y : Young's modulus

$< z_i >$: position of center of mass of i^{th} layer

Z_I: charge of nuclei

Contents

Chapter 1

Introduction

In this thesis, we present theoretical studies of the properties of some examples of low-dimensional systems and nanomaterials. Both these classes of materials have properties which may be different, both quantitatively and qualitatively, from those of the corresponding three dimensional homogeneous bulk systems. For this reason, the study of such materials is of both fundamental and technological interest. This has led to a surge in research activity in this area in recent years. In the case of nano-materials, the technological impetus comes from not only their (possibly) novel properties, but also the prospect that their use will lead to an easy miniaturization of devices. Moreover, in some cases, the technological motivation is the prospect that smaller quantities of expensive materials may be required to obtain a desired effect.

1.1 Low-dimensional systems and nano-structured materials

Both low-dimensional systems and nano-structured materials can exhibit novel properties which may arise from interesting physics.

1.1.1 Low-dimensional systems

Those systems whose properties are significantly affected by the fact that they are finite along at least one dimension fall under the category of low-dimensional materials. They can be two-, one- or zero-dimensional. Surfaces, thin films and monolayers are typical examples of two-dimensional systems. One-dimensional systems include nanotubes, nanowires and nanorods, while clusters and quantum dots are examples of zero-dimensional systems. The reduction in dimensionality usually results in a reduction of atomic coordination number. This leads to properties which are different from those of the corresponding bulk material, and also, sometimes, drastic structural rearrangement.

Some or all of the features mentioned in the previous paragraph will be displayed by the low-dimensional systems studied in this thesis: Te nanowires, Te clusters, the Ir{100} surface, Rh{100} surface and a monolayer of Rh on MgO{100}, and Rh clusters. For example, zero-dimensional Rh clusters are ferromagnetic and thus possess properties that are absent in the non-magnetic bulk [1]. An example of structural rearrangement due to reduced coordination is presented by the two-dimensional Ir{100} surface which reconstructs [2]. A contrasting example is the case of one-dimensional Te nanowires, which possess similar structural features to Te bulk.

Our general approach to the study of such low-dimensional systems will be first to compute their structure, accompanied by an effort to understand the factors that determine their structure. Having obtained structures, we will next attempt to accurately calculate properties (vibrational, elastic, optical, magnetic and chemical). We will also then look for trends (size-dependent, reconstructed vs. unreconstructed, cluster vs. bulk, nanowires vs. bulk, etc.).

1.1.2 Nano-structured materials

This thesis also includes one chapter in which we have studied nano-structured materials; such materials, though macroscopic, are comprised of the building blocks of nanometer sized particles. The properties of these materials are governed by the size of the particles and are often completely different from the parent material. For example, Al_2O_3-Cr and Al_2O_3-Cr/Ni composites have been shown to be much tougher than parent alumina [3].

In this thesis, we are interested in studying an interesting property observed in a special class of nano-materials called relaxor ferroelectrics. $PbMg_{\frac{1}{3}}Nb_{\frac{2}{3}}O_3$ (PMN) is a typical example of a relaxor ferroelectric, in which the Ti ion in $PbTiO_3$ has been replaced stoichiometrically by Mg and Nb. This replacement of Ti ions has introduced chemical disorder in the system which results in the formation of tiny regions (of the order of a few nanometers) of local and randomly-oriented electric polarization, also known as polar nano-regions (PNR). These PNRs lead to a completely different dielectric behavior of PZN, as a function of temperature (T). While the dielectric constant vs. T plot of the parent material ($PbTiO_3$) shows a sharp peak denoting a ferroelectric phase transition, PMN shows a broad peak. This new type of phase transition is called a diffusive phase transition. In some relaxors, experimentalists have observed a substantial softening of long wave length optical vibrations, which they named the "waterfall phonon" phenomenon. We hope to provide a microscopic understanding of this effect, whose origin has not yet been clearly established.

1.1.3 Experiment or theory or both?

Over the years there has been substantial development in experimental techniques, which has led to many new discoveries. At the same times, theory has

been an effective tool to understand such discoveries, both microscopically and macroscopically. With the help of theory, one can not only explain structure-property relationships (as we will do for the Te nanowires) but can also go beyond this to explain why a particular structure is favored over others (as we will do in our study of the origin of helical structures in Te). Moreover, a schematic theoretical study of a property of interest of a material may enable one to separate out the effects of different factors on that particular property; this may not be feasible in experiments. For example, it is well known that strain, magnetism, coordination number and charge transfer affect the metal-adsorbate binding, which in turn may affect the reaction barrier in a catalytic reaction taking place with the help of a metal catalyst. To tune each of these contributing factors separately in experiments is challenging if not impossible. However, we can (and will) attempt to do this by theoretically studying adsorption on four systems, two of which are real, the remaining two being hypothetical. In general, research in the broad areas covered by this thesis is driven both by experiment and theory: new experimental results motivate theoretical studies, which in turn may provoke further experiments. As will become evident, much of the work in this thesis was motivated by the desire to explain experimental results. However, we hope that our work will also stimulate further experimental studies.

1.2 Theoretical tools

Nowadays many theoretical tools are available to study different phenomena, depending on the time/length scales involved. In this thesis, we will use both quantum mechanical and classical tools. While quantum mechanical calculations (density functional theory) will be used to study the properties of low-dimensional systems, we will use a classical model to study the "waterfall phonons".

For the low-dimensional systems, as we are interested in properties which are affected by reduced coordination, we require a sophisticated theoretical treatment: we cannot, for example, use classical pair potentials for these systems, as such potentials depend only on the distance between pairs of atoms, and are therefore insensitive to reduced coordination. Moreover, in some cases we are interested in differences in energies which are very small. Hence we cannot use semi-empirical potentials, like glue potentials, embedded atom potentials, or effective medium theory. We need a sophisticated and accurate theoretical technique that can easily handle and describe changes in coordination.

Density functional theory (DFT), formulated initially by W. Kohn, P. Hohenberg and L. J. Sham [4, 5], is perhaps one of the most sophisticated techniques currently available. It is (at least formally) exact, allows one to calculate several properties with reasonable accuracy and *ab initio*, i.e., we need to know beforehand only the atomic number of the elements, and do not require any empirical input. In this thesis we have made use of DFT, as well as its extension in the form of density functional perturbation theory (DFPT). Both these theories have been implemented in many software packages which are available both freely and commercially. For our studies on low-dimensional systems we have used the ABINIT, CASTEP and Quantum-ESPRESSO packages. These three packages are more-or-less equivalent, sharing many features, though some details of implementation differ.

However, for our study of the waterfall phonons observed in relaxor ferroelectrics, we have used classical modeling. In nano-structured materials, the absence of long range order makes size unfeasible to perform quantum mechanical calculations. Hence we have replaced the complex system with a simplified model, with the interatomic interactions being described by classical potentials.

1.3 Outline of Thesis

The rest of this thesis is divided into seven chapters:

Chapter 2 provides a detailed description of DFT , DFPT and the technical issues related to performing DFT/DFPT-based calculations, such as pseudopotentials, smearing, choice of basis sets, calculation of forces, etc.

In Chapter 3 we present studies on the size dependence of the properties of Te nanowires as a function of their radius. This study was motivated by the fact that though Te nanowires can be readily synthesized in laboratories [6–8], it is very difficult to characterize them. Bulk Te consists of helical chains arranged in an hexagonal lattice. We are interested in understanding how system properties change from the large-size limit of the bulk form down to the smallest-size limit of a single helix (this has not yet been synthesized). In this chapter we have made use of DFT to study structure-property relationships.

In Chapter 4, we go a step ahead and try to determine the origin of the stability of the helical structures found in Te, through studies of Te clusters, nanowires and an infinitely long chain of Te atoms.

The study of the lifting of reconstruction in Ir{100} by CO adsorption, in Chapter 5, was motivated by experimental observations. The Ir{100} surface undergoes reconstruction to form a quasi-hexagonal (5×1) surface unit cell, with an atomic density increase of 20%. However, upon adsorption of atomic or molecular adsorbates on this surface, the reconstruction is lifted. Although it seems to be experimentally well established that the process of structural change is governed by a non-linear growth law, the mechanism is not well understood. It is not known whether the origin of the growth law is thermodynamics or kinetics. As a first step to addressing this question, in this chapter we study the issue of thermodynamic stability.

Motivated by a desire to design better catalysts, we have tried to understand the effects of strain, charge transfer, magnetism and coordination number on NO adsorption on Rh{100} surfaces (in Chapter 6) and small Rh clusters (in Chapter 7). In order to incorporate all these effects of the environment into a single quantity we have defined an effective coordination number. However we also try to separate out these effects and determine their relative importance.

Finally, in Chapter 8 we study "waterfall phonons" and try to provide a microscopic understanding of their origin.

Chapter 2

Computational Methods

2.1 Density functional theory

2.1.1 Introduction

A piece of matter can be imagined as a collection of interacting nuclei and electrons, sometimes under the influence of an external field. This ensemble of particles may be in the gas phase or in a condensed matter phase. The Hamiltonian ($\hat{H}$) for such a system of particles can be written as:

$$\hat{H} = -\frac{\hbar^2}{2m_e}\sum_i \nabla_i^2 + \sum_{i,I}\frac{Z_I e^2}{\mid \mathbf{r}_i - \mathbf{R}_I \mid} + \frac{1}{2}\sum_{i\neq j}\frac{e^2}{\mid \mathbf{r}_i - \mathbf{r}_j \mid} - \sum_I \frac{\hbar^2}{2M_I}\nabla_I^2 + \frac{1}{2}\sum_{I\neq J}\frac{Z_I Z_J e^2}{\mid \mathbf{R}_I - \mathbf{R}_J \mid}, \tag{2.1}$$

where h is the Planck's constant and $\hbar = h/2\pi$. m_e is the mass of electrons and $\mathbf{R}_I$ and $\mathbf{r}_i$ are the positions of the I^{th} nucleus and i^{th} electron respectively. The summation indices for the electrons are denoted by lower case and that of nuclei of mass M_I and charge Z_I are denoted by upper case subscripts. In

principle all the properties of the system under investigation can be derived by solving the time-independent Schrödinger equation:

$$\hat{H}\Psi_n(\mathbf{R},\mathbf{r}) = \varepsilon_n\Psi_n(\mathbf{R},\mathbf{r}), \tag{2.2}$$

where ε_n are the energy eigenfunctions and $\Psi_n(\mathbf{R},\mathbf{r})$ are the corresponding energy eigenvalues of the total system.

However the number of particles constituting a piece of matter is usually very large (of the order of Avogadro's number), resulting in a large number of degrees of freedom (DOF). For example, if there are N electrons and N_Z nuclei in the system, there are $3(N + N_Z)$ DOF. The fact that electrons are fermions and hence their wavefunctions should be anti-symmetric with respect to interchange of their positions makes the problem much more complicated. Moreover, the presence of the Coulomb interaction prevents the separation of the electronic and the nuclear degrees of freedom. All these problems, as well as other technical reasons, make it impossible to solve Eqn. 2.2 within a full quantum mechanical framework. As a result,it is necessary to make certain approximations to solve the above equation.

2.1.2 Adiabatic or Born-Oppenheimer approximation

Born and Oppenheimer [190] (BO) observed that the nuclei are much heavier than the electrons. As a result, electrons can move much faster than nuclei. Therefore the time scale associated with the motion of nuclei is much slower than that associated with the electrons. Hence it can be assumed that electrons instantaneously follow the nuclear motion while remaining in the same stationary state of the electronic Hamiltonian, i.e. the nuclei follow their dynamics and the electrons instantaneously adjust their wavefuctions according to the nuclear wavefunction.

Keeping the above approximation in mind, the fourth term in Eqn. 2.1 is very small and can be treated as a perturbation to $\hat{H}$. Thus the eigenfunctions and the eigenvalues of the electrons can be defined in such a way that they depend upon the nuclear positions $\mathbf{R}$ as parameters. The eigenfunctions of the coupled system can now be written as:

$$\Psi(\mathbf{R}, \mathbf{r}) = \sum_n \chi_n(\mathbf{R}) \Psi_n(\mathbf{R}, \mathbf{r}), \tag{2.3}$$

where $\Psi_n(\mathbf{R}, \mathbf{r})$ defines a complete set of states for the electrons at each $\mathbf{R}$ and $\chi_n(\mathbf{R})$ are the coefficients of the electronic states. Using the above equation, Eqn. 2.2 can be rewritten as two coupled differential equations:

$$\begin{aligned}
[-\frac{\hbar^2}{2m_e}\sum_i \nabla_i^2 + \sum_{i,I} \frac{Z_i e^2}{\mid \mathbf{r}_i - \mathbf{R}_I \mid} + \frac{1}{2}\sum_{i \neq j} \frac{e^2}{\mid \mathbf{r}_i - \mathbf{r}_j \mid} \\
+\frac{1}{2}\sum_{I \neq J} \frac{Z_I Z_J e^2}{\mid \mathbf{R}_I - \mathbf{R}_J \mid}]\Psi_n(\mathbf{R}, \mathbf{r}) = E_n(\mathbf{R})\Psi_n(\mathbf{R}, \mathbf{r}) \qquad (2.4) \\
[-\sum_I \frac{\hbar^2}{2M_I}\nabla_I^2 + E_n(\mathbf{R})]\chi_n(\mathbf{R}) = \varepsilon \chi_n(\mathbf{R}). \qquad (2.5)
\end{aligned}$$

Thus within the full BO approximation, nuclei in polyatomic systems are subject to an effective potential $E_n(\mathbf{R})$ determined by the solution of the electronic problem. The vibrational DOF are now decoupled from those of the electronic DOF. $E_n(\mathbf{R})$ is also called the BO potential energy surface (PES).

Eqn. 2.5 is easily solvable if $E_n(\mathbf{R})$ is known. However, to obtain $E_n(\mathbf{R})$ we need to solve Eqn. 2.4 which still has the Coulomb two-body terms and the exchange correlation. This equation is still not solvable within a full quantum mechanical framework, giving rise to the necessity of further approximations.

2.1.3 Hohenberg-Kohn theorems

In 1964 Hohenberg and Kohn [4] (HK) proposed two theorems in an attempt to provide an exact theory for a system of interacting particles. They are [9]:

1. **Theorem I**: For any system of interacting particles in an external potential $V_{\text{ext}}(\mathbf{r})$, the potential $V_{\text{ext}}(\mathbf{r})$ is determined uniquely, except for a constant, by the ground state particle density $n_0(\mathbf{r})$.

2. **Theorem II**: A *universal functional* for the energy $E[n]$ in terms of the density $n(\mathbf{r})$ can be defined, valid for any external potential $V_{\text{ext}}(\mathbf{r})$. For any particular $V_{\text{ext}}(\mathbf{r})$, the exact ground state energy of the system is the global minimum value of this functional, and the density $n(\mathbf{r})$ that minimizes the functional is the exact ground state density $n_0(\mathbf{r})$.

According to the HK theorems, since all properties such as kinetic energy, etc., are uniquely determined if $n(\mathbf{r})$ is specified, then each such property can be viewed as a functional of $n(\mathbf{r})$, including the total energy functional. Thus for a given potential $V_{\text{ext}}(\mathbf{r})$, this energy functional [also known as HK functional (E_{HK})] is given by:

$$E_{HK}[n] = F[n] + \int V_{\text{ext}}(\mathbf{r})n(\mathbf{r})d\mathbf{r}, \tag{2.6}$$

where the functional $F[n]$ contains the kinetic energy $(T[n])$ of the electrons and the electron-electron interaction (E_{e-e}). Thus, $F[n]$ can be written as:

$$F[n] = T[n] + E_{e-e}. \tag{2.7}$$

It is to be noted that by the above formalism we get only the ground state density and energy exactly. E_{HK} is minimized by the electron charge density of the ground state corresponding to the external potential $V_{\text{ext}}(\mathbf{r})$, under the

constraint that the integral of $n(\mathbf{r})$ equals the total number of electrons. Thus the HK theorem replaces the traditional description based on wavefunctions (which depend on $3N$ independent variables, N being the number of electrons) with a much more tractable description in terms of the charge density which depends only on three variables. This results in enormous simplification of the quantum mechanical problem of searching for the ground-state properties of a system of interacting particles. However the functional form of $F[n]$ is not known, the HK theorem proves that it exists, but does not give its form.

2.1.4 The Kohn-Sham ansatz

Kohn and Sham [5] came up with a form of $F[n]$ in 1965. Their approach is to replace the difficult interacting many-body system obeying the Hamiltonian of Eqn. 2.1 with an auxiliary system that can be solved more easily. The Kohn-Sham ansatz rests on two assumptions [9]:

1. The exact ground state density can be represented by the ground state density of an auxiliary system of non-interacting particles.

2. The auxiliary Hamiltonian is chosen to have the usual kinetic operator and an effective local potential $V_{\text{eff}}(\mathbf{r})$ acting on an electron at point $\mathbf{r}$.

Using the above two assumptions, the Kohn-Sham approach is to replace the Hohenberg-Kohn expression for the ground state energy functional with:

$$F_{KS}[n] = T_0[n] + E_{\text{H}}[n] + E_{\text{XC}}[n], \tag{2.8}$$

where $T_0[n]$ is the ground state kinetic energy of a system of non-interacting electrons as a function of its ground state charge density distribution. $E_{\text{H}}[n]$, which is given by

$$E_{\mathrm{H}}[n] = \frac{e^2}{2}\int \frac{n(\mathbf{r})n(\mathbf{r}^{'})}{\mid \mathbf{r}-\mathbf{r}^{'} \mid} d\mathbf{r}d\mathbf{r}^{'}, \tag{2.9}$$

is the Hartree energy and $E_{\mathrm{XC}}[n]$ is the exchange- correlation energy. Therefore the KS total energy functional,$E_{KS}[n]$, is given by:

$$E_{KS}[n] = F_{KS}[n] + \int n(\mathbf{r})V_{\mathrm{eff}}(\mathbf{r})d\mathbf{r}. \tag{2.10}$$

The variation of $E_{KS}[n]$ with the constraint that the total number of electrons is kept fixed, leads to the same equation as would hold for a system of non-interacting electrons subject to an effective potential $V_{SCF}(\mathbf{r})$, whose form is

$$V_{SCF}(\mathbf{r}) = V_{\mathrm{ext}}(\mathbf{r}) + e^2\int \frac{n(\mathbf{r}^{'})}{\mid \mathbf{r}-\mathbf{r}^{'} \mid} d\mathbf{r}^{'} + v_{XC}(\mathbf{r}), \tag{2.11}$$

where

$$v_{XC}(\mathbf{r}) \equiv \frac{\delta E_{XC}}{\delta n(\mathbf{r})}, \tag{2.12}$$

is the functional derivative of the exchange-correlation energy.

Thus if V_{SCF} is known one needs to solve only the one electron Schrödinger equation:

$$(-\frac{\hbar^2}{2m}\nabla^2 + V_{SCF}(\mathbf{r}))\psi_n(\mathbf{r}) = \epsilon_n\psi_n(\mathbf{r}). \tag{2.13}$$

$\psi_n(\mathbf{r})$ are the auxiliary Kohn-Sham orbitals. The charge density $n(\mathbf{r})$ is given by:

$$n(\mathbf{r}) = \sum_{n=1}^{N} \mid \psi_n(\mathbf{r}) \mid^2 . \tag{2.14}$$

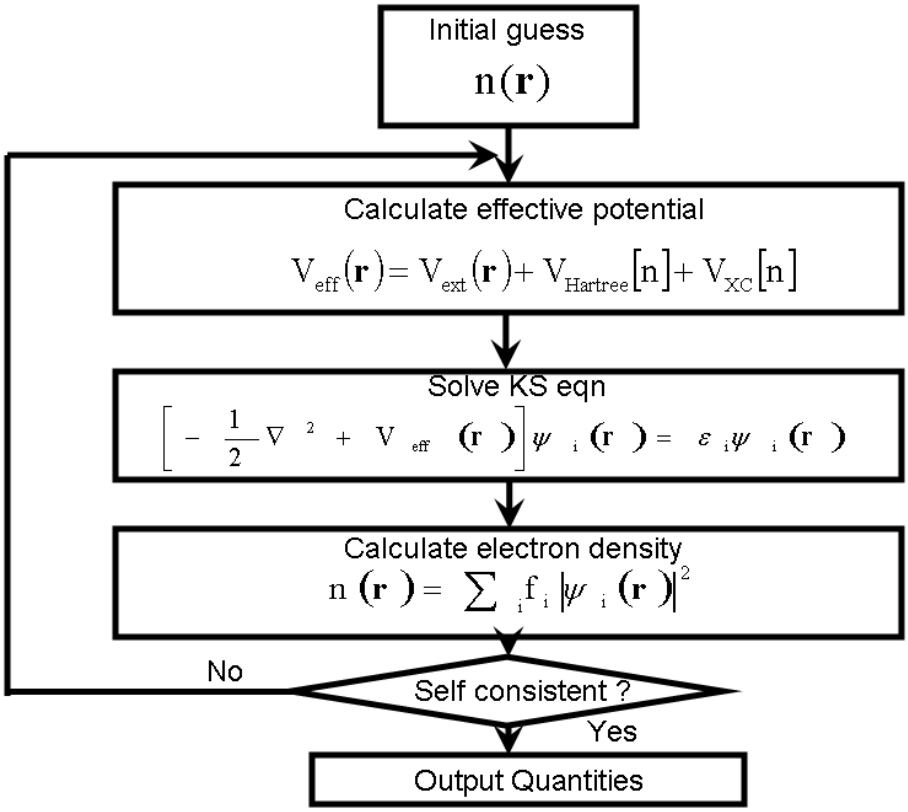

Figure 2.1: Flow chart showing the self consisting loop used to solve the KS equation (Eqn. 2.13).

The total energy of the system can be obtained by solving the system of effective one particle equations. Thus the Kohn-Sham equations map a many body problem to a single particle non-interacting problem. Eqn. 2.13 can be solved in a self-consistent way, the procedure of which is shown in Fig. 2.1. However, the exact form of the exchange-correlation energy is not known and needs to be approximated. This will be discussed in the next section.

2.1.5 Exchange-Correlation

The many body effects of a system of N particles are incorporated in the exchange correlation potential. Other than the Coulomb interaction between

the electrons there exists another type of interaction between them which arises because of their spin. Since electrons obey the Pauli exclusion principle, if there is an electron with spin up (or down) at $\mathbf{r}$, and another electron with the same spin comes in the vicinity of $\mathbf{r}$, it experiences a repulsive potential. This repulsive interaction between electrons of the same spin is called the exchange interaction. The exchange energy is defined as the difference between the Hartree and the Hartree-Fock energy.

The remaining many-body effects are included in the correlation interaction. The correlation energy is defined as the difference between the exact energy and the Hartree-Fock energy.

Since the exact form of the exchange-correlation potential is not known, it is generally approximated as a local or semilocal functional of the density. The local approximation is popularly known as the Local Density Approximation (LDA) and the semi-local one is known as the Generalized Gradient Approximation (GGA).

The LDA of the exchange correlation energy is an integral over space with an approximation that the exchange-correlation density at each point is the same as in a homogeneous electron gas with that density. Mathematically the exchange-correlation energy within the LDA ($E_{\mathrm{XC}}^{\mathrm{LDA}}$) can be written as:

$$E_{\mathrm{XC}}^{\mathrm{LDA}}[n] = \int n(\mathbf{r})\epsilon_{\mathrm{XC}}^{\mathrm{hom}}(n(\mathbf{r}))d\mathbf{r}, \tag{2.15}$$

where $\epsilon_{\mathrm{XC}}^{\mathrm{hom}}(n(\mathbf{r}))$ is the exchange-correlation density at $\mathbf{r}$ of a homogeneous electron gas of density $n(\mathbf{r})$. The exchange-correlation potential ($v_{\mathrm{XC}}^{\mathrm{LDA}}$) is given by:

$$v_{\mathrm{XC}}^{\mathrm{LDA}}(\mathbf{r}) = \frac{\delta E_{\mathrm{XC}}^{\mathrm{LDA}}[n]}{\delta n(\mathbf{r})}. \tag{2.16}$$

Approximate forms of $\epsilon_{\mathrm{XC}}^{\mathrm{hom}}$ have been obtained from Quantum Monte Carlo

calculations by Ceperley and Alder [10], which were later parametrized by Perdew and Zunger [11] using a simple analytical form.

Although the LDA approximtion can adequately describe properties of weakly correlated systems like semiconductors and simple metals, it fails miserably in estimating binding energies and for strongly correlated systems such as transition metal oxides. To overcome these failures of the LDA, the exchange-correlation energy is evaluated with an approximation that at each point in space it is not only a functional of $n(\mathbf{r})$ but also of its gradient and higher derivatives. This is known as the Generalized Gradient Approximation (GGA). Within the GGA, the exchange-correlation energy ($E_{\mathrm{XC}}^{\mathrm{GGA}}$) is given by:

$$E_{\mathrm{XC}}^{\mathrm{GGA}} = \int n(\mathbf{r})\epsilon_{\mathrm{XC}}^{\mathrm{hom}}(n(\mathbf{r}), \mid \nabla n(\mathbf{r}) \mid, \mid \nabla^2 n(\mathbf{r}) \mid d\mathbf{r}, ...). \tag{2.17}$$

Within the GGA, there are many approximations of the exchange-correlation energy functional. The most widely used ones are those developed by Becke (B88) [12], Perdew and Wang (PW91) [13] and Perdew, Burke and Ernzerhof (PBE) [14]. GGAs are found to improve the treatment of electron correlations in finite or semi-infinite systems. However they are still unable to provide a proper description of strongly correlated infinite solids.

2.1.6 Total energy calculation

Using the eigenvalues obtained from the self consistent solution of the KS equations, the total energy of a system of N electrons is obtained using the following equation:

$$E_{tot}[n] = \sum_{i=1}^{N} \varepsilon_i - \frac{1}{2}\int \frac{n(\mathbf{r})n(\mathbf{r}')}{\mid \mathbf{r} - \mathbf{r}' \mid} d\mathbf{r}' d\mathbf{r} + E_{\mathrm{XC}}[n] - \int n(\mathbf{r})V_{\mathrm{XC}}(\mathbf{r})d\mathbf{r} + E_{Ewald}. \tag{2.18}$$

Because of the double counting of electrons in the calculation of energy eigenvalues, we substract half of the Hartree energy. The contribution to ε_i from exchange-correlation interaction ($\langle\psi_i \mid V_{\rm XC} \mid \psi_i\rangle$) is not equal to $E_{\rm XC}$. Hence in order to calculate E_{tot} we will subtract $\langle\psi_i \mid V_{\rm XC} \mid \psi_i\rangle$ and add $E_{\rm XC}$. E_{Ewald} is the energy of the nuclear-nuclear interaction for a particular ionic configuration $\mathbf{R}$, evaluated using Ewald summation method [15–17].

2.1.7 Basis

In order to solve the K-S equations, the electronic wavefunctions are usually expanded in a basis. Many types of basis sets can be used to do so, e. g., plane-wave, atomic-orbital and mixed-(atomic + plane wave) basis sets. The calculations in the present thesis have been done using a plane wave basis set, $e^{i(\mathbf{k}+\mathbf{G}).\mathbf{r}}$, where $\mathbf{k}$ is the wavevector at which the K-S equations are solved and $\mathbf{G}$ is a reciprocal lattice vector. The plane waves become discrete only when periodic boundary conditions are used. The number of plane waves in a basis set is determined by an energy parameter E_{cut} using the following equation:

$$\frac{\hbar \mid \mathbf{k}+\mathbf{G} \mid^2}{2m_e} < E_{cut}. \tag{2.19}$$

E_{cut} is determined by checking the convergence of the quantity of interest with E_{cut}.

The advantages of using a plane wave basis set are: (i) Pulay forces [18] being absent, as the basis is independent of atomic position, it is easy to evaluate forces using the Hellmann-Feynman theorem [19, 20], (ii) the quality of the basis is controlled by a single parameter and (iii) it is easy to implement while coding.

However, while using a plane wave basis, a large number of plane waves is

required to expand the wavefunctions in the core region, where the core electrons' wavefunctions are highly peaked, and valence electron wavefunctions have several oscillations. This problem can be removed by using pseudopotentials as described below.

2.1.8 Pseudopotentials

The effective potential experienced by the valence electrons when the core electrons are frozen is called the pseudopotential. It is obtained by pseudizing the wavefunction of the valence electrons, i.e., the oscillations of the valence electrons in the core region are removed. The pseudo wavefunction and all-electron wavefunction match each other beyond a particular value of radial distance r_c. r_c is chosen such that the last node of the all electron wave function lies within it. If the same pseudopotential can be used in different environments of the atom, the pseudopotential is said to be transferable. As r_c increases, the number of plane waves required to represent a pseudo wavefunction generally decreases, but the transferability also decreases. There are many types of pseudopotentials like norm-conserving, ultrasoft etc.

In norm-conserving pseudopotentials, in the core region, the norm of the pseudo-wavefunction is equal to the norm of the all electron wavefunction. This ensures the transferability of the pseudopotential.

Relaxation of the norm-conservation condition leads to Vanderbilt's ultrasoft potential [21] which allows one to use a very low energy cut-off. However, this is done at the expense of losing the orthonormality requirements of the atomic orbitals and the condition of norm conservation. The first problem is solved by considering a generalised eigenvalue problem, with a generalised orthogonality constraint expressed in terms of an overlap operator. The second problem is remedied by the addition of an augmentation charge localised within the core regions to the system's charge.

2.1.9 k-point sampling and smearing

Numerical integrals over the Brilluoin zone are obtained through a sum over a finite mesh of k-points. Generally the most widely used k-point mesh is the Monkhorst-Pack [22] grid. For metals this approximation is extremely delicate because the abrupt change in occupancy near the Fermi surface can make the sampling inadequate. Moreover, in order to capture the finite features of band crossing, one needs quite a fine k-point mesh for metals, making the calculations computationally expensive.

The use of the number of k-points for metals can be reduced by slightly broadening the energy levels. There are many ways to do this such as Gaussian broadening [23], Methfessel-Paxton smearing [24], Marzari-Vanderbilt cold smearing [25] etc.

2.1.10 Calculation of forces and stresses

In order to find out the relaxed geometry we need to calculate the forces and stresses acting on the individual atoms, so as to optimize the unit cell vectors and positions of the atoms in the unit cell. When the forces acting on the atoms are zero, it signifies that the atomic coordinates are relaxed. Zero stress implies that the unit cell lattice vectors have been optimized.

The forces are calculated by following the prescription provided by the Hellmann-Feynman theorem [19, 20] which says that the forces can be calculated using the following equations:

$$F_I = -\frac{\delta E(\mathbf{R})}{\delta \mathbf{R}_I} = -\langle \Psi(\mathbf{R}) \mid \frac{\delta E(\mathbf{R})}{\delta \mathbf{R}_I} \mid \Psi(\mathbf{R}) \rangle, \tag{2.20}$$

where $\Psi(\mathbf{R})$ are the electronic eigenstates of H_{BO} for a given configuration $\mathbf{R}$, F_I is the force acting on the I^{th} atom.

The advantage of this method is that we do not need to calculate the energies of the system at many configurations and can extract the information of the force constants for the bonds easily. There should be an additional term to Eqn. 2.20, which is the derivative of the basis set with respect to the position of the ion. This term, which is called the Pulay force, vanishes if we use a complete basis set and the Hellmann-Feynman forces become exactly equal to the derivative of the total enery with respect to the position of the ions. However, we usually use an incomplete basis set. As a result the Pulay force does not vanish, introducing an error in the calculated Hellmann-Feynman forces. Using a plane wave basis set one can easily get rid of these forces.

Stresses are calculated using the "stress theorem" of Nielsen and Martin [26, 27]. The stress tensor, $\sigma^s_{\alpha\beta}$, is the derivative of total energy with respect to the strain tensor, $\epsilon^s_{\alpha\beta}$:

$$\sigma^s_{\alpha\beta} = -\frac{1}{\Omega}\frac{\delta E_{tot}}{\epsilon_{\alpha\beta}}, \tag{2.21}$$

where α and β are the Cartesian indices and Ω is the volume of the unit cell. The above equation can also be written as:

$$\sigma^s_{\alpha\beta} = -\langle \Psi \mid \frac{\delta H_{BO}}{\delta \epsilon_{\alpha\beta}} \mid \Psi \rangle. \tag{2.22}$$

2.2 Phonons from density functional perturbation theory

A wide variety of physical properties of solids, such as infrared, Raman and neutron diffraction spectra, specific heats, thermal expansions, etc., depend on the lattice-dynamical behaviour of the solids. The basic theory of lattice vibrations was first developed by Born and Huang [28]. Over the last few

years, with the development of DFT and density functional perturbation theory (DFPT) [29–31], a large number of *ab initio* calculations [32, 33] based on linear response theory of lattice vibrations have been done.

2.2.1 Lattice dynamics from electronic-structure theory

We have seen before that the adiabatic approximation enables us to decouple the vibrational degrees of freedom (DOF) from the electronic DOF.

The vibrational frequencies ω are determined by the eigenvalues of the Hessian matrix of the Born-Oppenheimer energy (also called the matrix of the interatomic force constants), scaled by their nuclear masses:

$$\det|\frac{1}{\sqrt{\mathrm{M_I M_J}}}\frac{\partial^2 \mathrm{E}(\mathbf{R})}{\partial \mathbf{R}_\mathrm{I}\partial \mathbf{R}_\mathrm{J}} - \omega^2| = 0. \tag{2.23}$$

As mentioned in the Section 2.1.10, the forces are given by the Hellmann-Feynman theorem. The Hamiltonian depends on $\mathbf{R}$ via the electron-ion interaction that couples to the electronic degrees of freedom only through the electron charge density. The force acting on I^{th} nucleus is given by:

$$\mathbf{F}_I = -\int n_{\mathbf{R}}(\mathbf{r})\frac{\partial V_{\mathbf{R}}(\mathbf{r})}{\partial \mathbf{R}_I}d\mathbf{r} - \frac{\partial E_{Ewald}(\mathbf{R})}{\partial \mathbf{R}_I}, \tag{2.24}$$

where $V_{\mathbf{R}}(\mathbf{r})$ is the electron-nucleus interaction,

$$V_{\mathbf{R}}(\mathbf{r}) = -\sum_I \frac{Z_I e^2}{\mid \mathbf{r} - \mathbf{R}_I \mid}. \tag{2.25}$$

The Hessian of the B-O energy surface appearing in Eqn. 2.23 is given by:

$$\frac{\partial^2 E(\mathbf{R})}{\partial \mathbf{R}_I \partial \mathbf{R}_J} \equiv -\frac{\partial \mathbf{F}_I}{\partial \mathbf{R}_J} = \int \frac{\partial n_{\mathbf{R}}(\mathbf{r})}{\partial \mathbf{R}_J}\frac{\partial V_{\mathbf{R}}(\mathbf{r})}{\partial \mathbf{R}_J}d\mathbf{r} + \int n_{\mathbf{R}}(\mathbf{r})\frac{\partial^2 V_{\mathbf{R}}(\mathbf{r})}{\partial \mathbf{R}_I \partial \mathbf{R}_J}d\mathbf{r} + \frac{\partial^2 E_N(\mathbf{R})}{\partial \mathbf{R}_I \partial \mathbf{R}_J}.$$

Eqn. 2.26 states that in order to calculate the Hessian of the BO surface one needs to calculate $n_{\mathbf{R}}(\mathbf{r})$ and its linear response to a distortion of the nuclear geometry $\partial n_{\mathbf{R}}(\mathbf{r})/\partial \mathbf{R}_I$. While $n_{\mathbf{R}}(\mathbf{r})$ can be evaluated using DFT, DFPT is used to evaluate $n_{\mathbf{R}}(\mathbf{r})$.

2.2.2 Density-functional linear response

The electron response $(\partial n_{\mathbf{R}}/\partial \mathbf{R})$ appearing in Eqn. 2.26 can be obtained within the framework of DFPT. This is achieved by linearizing Eqns. 2.11, 2.13 and 2.14. Linearization of Eqn. 2.14 leads to

$$\Delta n(\mathbf{r}) = 2\mathrm{Re}\sum_{n=1}^{N} \psi_n^*(\mathbf{r})\Delta\psi_n(\mathbf{r}). \tag{2.26}$$

Variation of KS orbitals $\Delta\psi_n(\mathbf{r})$ is obtained by standard first-order perturbation theory:

$$(H_{SCF} - \epsilon_n) \mid \Delta\psi_n\rangle = -(\Delta V_{SCF} - \Delta\epsilon_n) \mid \psi_n\rangle, \tag{2.27}$$

where H_{SCF} is the unperturbed KS Hamiltonian and $\Delta\epsilon_n = \langle\psi_n \mid \Delta V_{SCF} \mid \psi_n\rangle$ is the first order variation of the KS eigenvalues. The first order correction to the self consistent potential ΔV_{SCF} is given by:

$$\Delta V_{SCF}(\mathbf{r}) = \Delta V(\mathbf{r}) + e^2 \int \frac{\Delta n(\mathbf{r}')}{\mid \mathbf{r} - \mathbf{r}' \mid} + \frac{dv_{XC}(n)}{dn}|_{n=n(r)}\Delta n(\mathbf{r}). \tag{2.28}$$

Eqns. 2.26, 2.27 and 2.28 form a set of self-consistent equations for the perturbed system, completely analogous to the KS equation in the unperturbed case, with the KS eigenvalue equation being replaced by the solution of a linear system. The value of $\partial n_{\mathbf{R}}(\mathbf{r})/\partial \mathbf{R}_I$ is then fed bcak to Eq. 2.26 to get the

dynamical matrix.

Usually the first order correction to a given eigenfunction of the Schrödinger equation is given by:

$$\Delta\psi_n(\mathbf{r}) = \sum_{m \neq n} \psi_m(\mathbf{r}) \frac{\langle \psi_m \mid \Delta V_{SCF} \mid \psi_n \rangle}{\epsilon_n - \epsilon_m}, \tag{2.29}$$

the summation running over all the states of the system, occupied or empty. Thus in the explicit evaluation of $\Delta\psi_n(\mathbf{r})$ from Eqn. 2.29 we need to have the knowledge of the full spectrum of the KS Hamiltonian and extensive summations over conduction bands. Instead, if we evaluate $\Delta\psi_n(\mathbf{r})$ using Eqn. 2.27, only knowledge of the occupied states of the system is necessary, and many efficient algorithms can be used for the solution of the linear system. Therefore, in this way the computational cost of determining the density response to a single perturbation is of the same order as that needed to calculate the unperturbed ground state density.

The method discussed so far holds good for systems with band gaps. However for metals one needs to take into account the presence of finite density of states at the Fermi level and the change in orbital occupation number which may occur upon the application of an infinitesimal perturbation.

Chapter 3

Atomic and Electronic Structures, Elastic Properties and Optical Conductivity of Bulk Te and Te Nanowires

3.1 Introduction

One-dimensional nanostructures such as nanowires, nanorods, or nanotubes have been subject of intensive research for the past few years due to their potential use as interconnects and active components in fabricating nanoscale electronic or optoelectronic devices [34]. They represent interesting systems for investigating the dependence of optical, electrical, electrochemical and mechanical properties on size [35]. There has been a surge in research activities related to synthesis, characterization and theoretical studies of nanowires of various inorganic materials like oxides, sulfides and nitrides as well as elemental metals.

One of the elemental materials of interest is tellurium (Te) which has several interesting physical and chemical properties like photo conductivity, thermoelectric effect, non-linear optical responses and catalytic activity [36], which make it useful in applications like electronic and optoelectronic devices and xerography [37]. Unlike other elements of Group VI (O, S, Se), bulk Te exhibits only one crystalline form, namely trigonal. The crystal structure of t-Te consists of parallel helical chains stacked on a triangular lattice, with their axes parallel to the crystalline c axis. The space group of the crystal is D_3^4 and D_3^6 depending on the sense of rotation of the helical chain. Structure and properties of Te show anisotropy (though less than the isostructural trigonal selenium) which arises from the disparity between a strong covalent bonding between neighboring atoms belonging to a single helix (intrachain) and a relatively weaker bonding interactions between atoms on the neighboring chains (interchain).

Recently research groups have synthesized nanowires and nanotubes of t-Te [6–8]. The availability of Te nanowires has opened up possibilities of new types of applications and has made it important to know how the properties of Te nanowires depend on their diameter and affect their performance in the present devices. Fundamentally, it is interesting to understand the stability of Te nanowires as bundles of helices and how the quantum size effects manifest in the size dependence of their properties.

We have used first-principles calculations to determine the atomic and electronic structures and various properties of bulk Te, its nanowires and single helix. In Section 3.2, we describe details of the first-principles calculations and results for the bulk to benchmark our calculations through comparison with earlier first principles calculations and experiments. A comparative study of atomic structures, binding energy and Young's modulus is presented in Section 3.3. We present the study of size dependence of electronic structures in Section

3.4. We report and discuss results for optical conductivity in Section 3.5 and summarize in Section 3.6.

3.2 Methods

We used the ABINIT [38, 39] package, an implementation of the density functional theory [4], based on first-principles optimized pseudo-potential and a generalized gradient approximation of the exchange correlation energy given by the Perdew-Burke-Ernzerhof (PBE) functional [14, 43, 44]. Our calculations are based on solution of the Kohn-Sham equations [5] by a fixed potential-based iterative conjugate-gradient minimizations [40] of one-electron energies and a mixing of potentials towards self-consistency. Optimized pseudo-potentials [41] were constructed using the OPIUM [42] and treating six electrons in the outermost s and p states as valence with cutoff radius of 2.1 Å and optimizing wave-vector of 5.5 a.u. An energy cutoff of 30 Ry was used on a plane-wave basis converging total energies within 1 mRy per atom.

We simulated bulk Te (3 atoms/cell), a double-shelled Te nanowire (Te-w2) with 57 atoms per cell and a diameter of about 22 Å, a single-shelled Te wire (Te-w1) with 21 atoms per cell and a diameter of about 14 Å and a single helix (Te-h) with 3 atoms per cell and a diameter of about 3.2 Å. The nanowires and helix are periodic in the $c-$direction but are confined in the $ab-$plane. We used hexagonal supercells with the in-plane lattice parameter a up to 40 Å, with a vacuum of about 10 Å separating the periodic images of the nanowires. This ensures negligible interaction between the periodic images.

Integrations over the Brillouin zone were evaluated with a $5\times5\times5$ Monkhorst-Pack mesh [22] (19 k points in the irreducible Brillouin zone (IBZ)) for bulk Te and $1\times1\times5$ grid (3 k-points in IBZ) for the wires of different diameters and the helix, with total energies converging within 2 meV/atom. As bulk Te is known

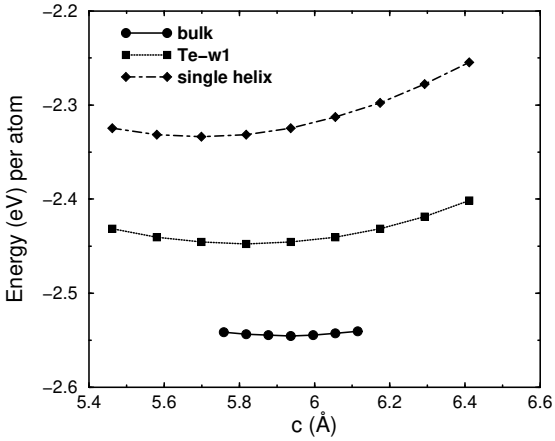

Figure 3.1: Cohesive energy per atom (with a negative sign) vs. lattice constant c for bulk Te, Te-w1 and a helix.

to be semi-metallic, we use a smearing of occupation numbers of states with a Gaussian function, corresponding to the zeroth order Hermite polynomial of Methfessel and Paxton [24], with a smearing temperature of 473 K for bulk Te and Te-h, 1136 K for Te-w1 and Te-w2. Structural optimization was carried out using the Hellmann-Feynman forces and the Broyden, Fletcher, Goldfarb, Shanno (BFGS)-based method [45] for the minimization of energy.

Structure of bulk Te is characterized by three parameters: a, c/a ratio and a reduced coordinate u giving the position of atoms projected onto the ab-plane from the axis of the helix; c is also the pitch of the helical chains. Structural optimization is carried out by keeping c fixed and relaxing a and u to minimize the total energy. Cohesive energy of a given Te structure is obtained by subtracting the total energy of free Te atoms from the total energy of the structure. In order to test the importance of zero-point motion we calculate the contribution of zero-point motion to the total energy of bulk Te. We find that the zero-point motion changes the total energy of Te bulk by about 5 meV. These changes are so small that they do not affect the equilibrium geometry. Henceforth, in our calculations, we will neglect the contributions to the total energy from zero-point motion. From the cohesive energy as a

Table 3.1: Comparison of minimum energy structure (unit cell volume Ω, c/a, internal structure parameter u, bond angle (θ), ratio d_2/d_1 of interchain and intrachain distances), bulk modulus (B) and cohesive energy (E) of Te with experiments and other calculations.

	$\Omega(\text{Å}^3)$	c/a	u	d_2/d_1	θ(in degrees)	B (Kbar)	E (eV/atom)
PBE-Ours	33.95	1.33	0.276	1.18	101.3	330	2.54
PB-Kresse [52]	36.11	1.31	0.269	1.21	101.0	180	2.35
Experimental [53, 54]	33.74	1.33	0.264	1.23	103.0	230	2.19

function of c (Fig. 3.1), the minimum energy structure and Young's modulus are readily obtained (Table 3.1). Our calculations yield a bulk structure that is slightly over-bound than the earlier calculation of Kresse et al [52], reflected in higher cohesive energy and bulk modulus, and smaller volume. Our estimates of the unit cell volume and the c/a ratio are in closer agreement with the experiment. The internal structural parameter u is overestimated by 4.5 % w.r.t. the experimental value, translating into similar errors in the ratio of interchain to intrachain distances (d_2/d_1) and the intrachain Te-Te-Te bond angle (θ).

3.3 Structure, cohesive energy and Young's modulus of Te nanowires

The cohesive energies (Fig. 3.1) clearly bear that bulk Te is most stable whereas Te-h is least stable. Coordination number of atoms in the bulk Te is 6, whereas it reduces to 2 in the case of a helix. Due to lower coordination of atoms at the surface of nanowires, intrachain-bond lengths are shorter (see Table 3.2) and hence their $c-$ parameter reduces with reducing diameter. As the presence of a surface in a nanowire costs energy and the fraction of atoms at the surface increases with reducing diameter, the cohesive energy per atom correspondingly reduces from 2.54 eV/atom of the bulk to 2.33 eV/atom of the helix.

The radius of a nanowire is an important parameter because estimation of many properties of the nanowires like surface energy, Young's modulus, etc., is sensitive to this radius. There are many ways of defining the radii of nanowires [46–48], which depend on their atomic radii, bond-lengths or charge distribution. We define here the radius of a wire R as the radius of a cylinder in which 99% of the total electronic charge in the system is enclosed,

i.e. $\int_0^R \int_0^c \rho(r) 2\pi r dz dr = 0.99 e N_e$, where $\rho(r)$ and N_e are the charge density and total number of electrons in the system respectively. Consistent with the reduction in the $c-$parameter, radius per helix of nanowires is found to increase with reducing diameter (given in Table 3.2). To check whether the trends of different physical properties of the nanowires are dependent on the definition of the radius, we have also evaluated the radius of Te-h, Te-w1 and Te-w2 using the definition given in Ref. 48. With this definition, we obtain radii of Te-h, Te-w1 and Te-w2 as 3.1 Å, 6.39 Åand 10.22 Årespectively [49].

We calculate the surface energy per unit area (Γ_s) of nanowires which is defined as:

$$\Gamma_s = \frac{E_{NW} - n_{NW} E_{bulk}}{A} \tag{3.1}$$

where E_{NW} and n_{NW} represent the total energy and the number of atoms of a nanowire respectively. E_{bulk} denotes the energy of a Te atom in bulk and $A(= 2\pi Rc)$ is the surface area of the nanowire. Surface energies of Te-w2, Te-w1 and Te-h are 0.14 J/m^2, 0.12 J/m^2 and 0.09 J/m^2 respectively.

Unlike bulk Te, which is a periodic lattice of helices, different helices of Te-w1 and Te-w2 are not identical. For example, while the point symmetry of Te-w1 nanowire is the same as that of the bulk (Spg. $P3_221$), the helices at its surface form two groups of three identical helices each, maintaining the three-fold rotational symmetry. Structural relaxation through displacements of Te atoms in the $ab-$plane results in variation of bond lengths and bond angles, listed in Table 3.2. The distance between a helix from the first group (marked by solid arrows in Fig. 3.2) and the central helix of Te-w1 d increases by 1.6% while that from the second group (marked by dashed arrows in Fig. 3.2) decreases by 0.7%. While the structure of the helix at the centre of Te-w1 is unchanged and its bond-lengths remain the same as those in the bulk Te ((2.91 Å)), Te-Te bond-lengths of Te atoms in helices at the periphery change due to structural relaxation. For the first group of helices (marked by the

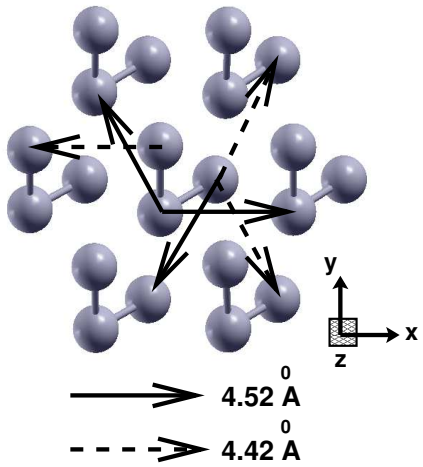

Figure 3.2: Variation of inter-helical distances d of Te-w1 due to surface effect.

solid arrows), relaxation results in two short (2.74 Å) and one long (2.86 Å) bonds, whereas it leads to two long (2.86 Å) and one short (2.79 Å) bonds in the second set of helices. In a given $ab-$plane, the long bonds of the former line up with the short bonds of the latter. For both the group of helices, atoms come close to each other compared to those of the bulk, resulting in the contraction of Te-w1 along the $c-$axis. Similar features are observed in the helices of Te-w2.

In order to estimate the strength of nanowires and compare them with that of the bulk, we determine their Young's modulus Y:

$$Y = \frac{1}{V_0} \left. \frac{\partial^2 E}{\partial \epsilon_{zz}^2} \right|_{\epsilon_{zz}=0} \tag{3.2}$$

where E is the relaxed total energy, ϵ_{zz} is the strain applied on the system ($= \frac{\delta c}{c}$) at an equilibrium volume V_0. The wires are treated as cylinders with radii R as defined earlier in this section and their volume per unit cell is given by $V_0 = \pi R^2 c$. The Young's modulus of bulk Te is 45.8 GPa, in close agreement with an experimental estimate of 43 GPa [50]. Our calculations predict that Y reduces, with reducing diameter, to 35.1 GPa and 28.5 GPa for the Te-w1 and

Table 3.2: Comparison of structural parameters, cohesive energy (E) and Young's modulus (Y) of bulk Te, Te-w2, Te-w1 and Te-h. R, R_{helix}, d, and θ are the radii of nanowires, radius of each helix constituting the bulk and the nanowires ($R_{helix} = (n)^{1/2}R$, n is the number of helices for each nanowire), inter-helical distances and Te-Te-Te intra-helix bond angle respectively.

System	R (Å)	R_{helix} (Å)	d (Å)	c (Å)	θ(degrees)	bond length (Å)	E (eV/atom)	Y(GPa)
bulk	-	2.3	4.45	5.93	101.3	2.91	2.54	45.8
Te-w2	10.98	2.52	4.45,4.52	5.86	98.9-105.1	2.74-2.9	2.48	-
Te-w1	6.88	2.6	4.42,4.52	5.82	98.3-104.1	2.74,2.79,2.85,2.86,2.91	2.44	35.1
Te-h	3.2	3.2	-	5.69	102.7	2.74	2.33	28.5

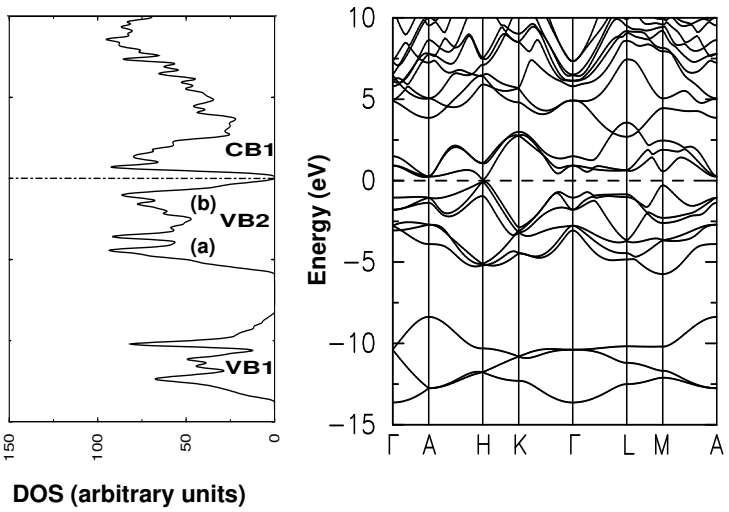

Figure 3.3: Electronic structure of bulk Te along high symmetry directions in the BZ of a hexagonal lattice (right panel). Density of states (DOS) of electrons is given in the left panel.

the helix respectively. Earlier in this section we showed that the intrachain bond lengths in the nanowires are shorter than that in bulk. This implies stronger intra-chain bonds in nanowires. If the helices in nanowires or bulk were non-interacting, the Young's modulus of the nanowires would have been higher than that of bulk. Smaller Young's modulus of nanowires is clearly an effect of changes in the bonding between atoms in different helices. For the bulk Te, each helix is surrounded by six nearest neighbor helices, whereas a helix at the surface of Te-w1 has only three neighboring helices and its separation from the neighboring helices is different than that in bulk. This results in fewer and weaker bonds between atoms in neighboring helices particularly at the surface of nanowires and hence their lower Young's moduli.

3.4 Electronic structure

Our calculated electronic structure of bulk Te (Fig. 3.3) compares quite well with earlier calculations [55, 61]. Valence bands occur in two groups: (i) VB1,

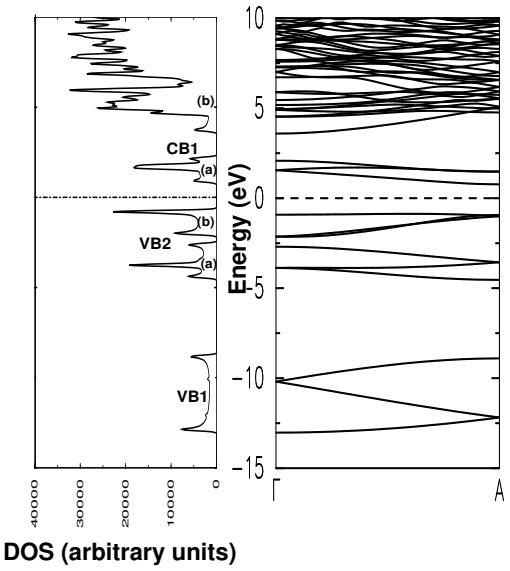

Figure 3.4: Density of states and electronic structure of Te-h. "a" and "b" denote the different sub bands of VB2 and CB1.

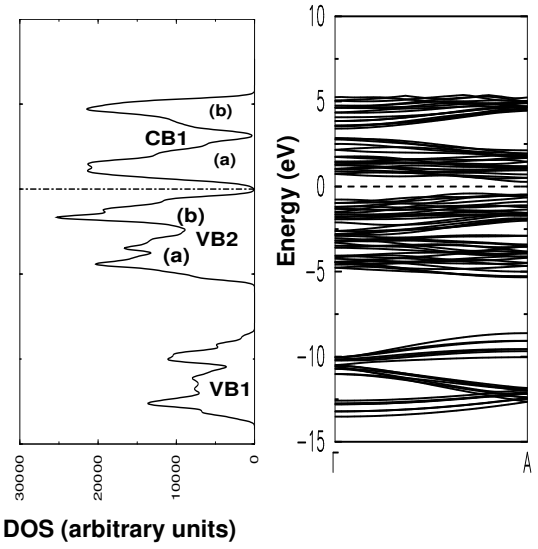

Figure 3.5: Density of states and electronic structure of Te-w1. "a" and "b" denote the different sub bands of VB2 and CB1 VB2(a) and VB2(b) merge into one band.

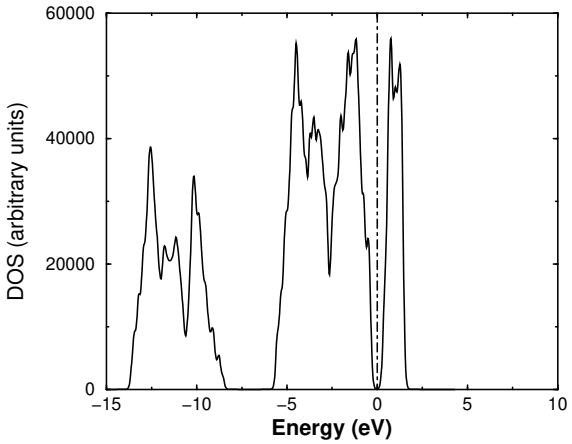

Figure 3.6: Density of states of Te-w2.

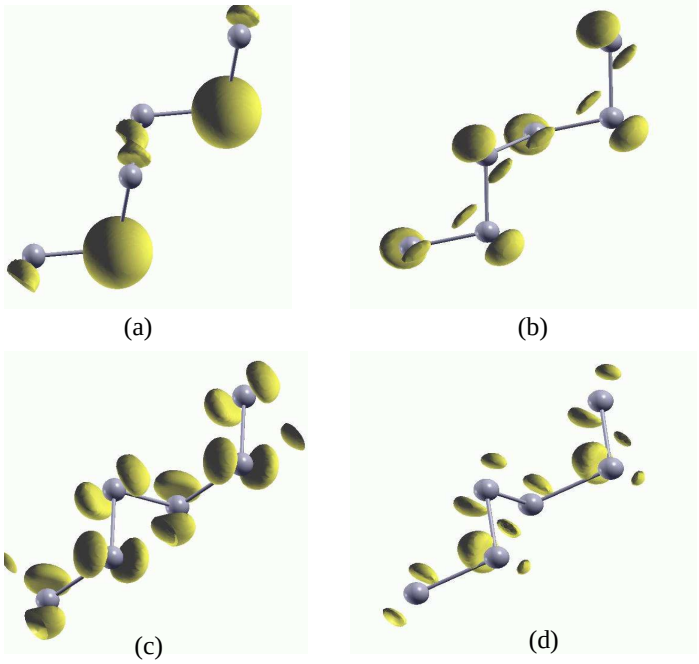

Figure 3.7: Isosurfaces of charge density for Te-h. The isovalue corresponding to the isosurfaces is 50% of the maximum isovalue. (a), (b), (c) and (d) are for VB1, VB2(a) VB2(b) and CB1(a) respectively. The helices are aligned such that the z-axis is parallel to the axis of the helix. These pictures have been generated using a software called Xcrysden [57].

with a band-width of about 5.5 eV, and (ii) VB2, higher in energy than VB1, with a band-width of 6.0 eV. The conduction band forms a continuum of states. The band VB2 and the conduction band are separated by a tiny direct gap of 0.15 eV at the H point, the experimental value of band gap being 0.33 eV [56]. This is consistent with typical under-estimation of gaps in the DFT calculations.

Band structure and DOS of Te-h (Fig. 3.4) show five distinct bands: (i) three valence bands, VB1, VB2(a) and VB2(b) and (ii) two conduction bands CB1(a) and CB2(b). The bands are flat resulting in sharp van Hove singularities in the DOS. For the nanowires (Te-w1 and Te-w2), if the neighboring helices are not interacting, the band structure would have been identical to that of Te-h. The interaction between neighboring helices of Te-w1 and Te-w2 causes an increase in overlap of the wave functions, as a consequence of which the band width increases. This is evident from Fig. 3.4, 3.5 and 3.6. For example in Te-h, VB2 consists of two bands, VB2(a) and VB2(b) while for the wires they merge into one band, namely VB2. The band widths of VB1 and VB2 bands of Te-w1 and Te-w2 are close to those of bulk Te while those of Te-h are smaller (Table 3.3). An increase in the bandwidth of the bands results in decrease of the band gaps with increasing thickness of the nanowires, which is consistent with the experimental findings [6]. Band gaps for all the three cases, namely Te-h, Te-w1 and Te-w2 are indirect ones.

Conduction bands of the nanowires, CB1, also show significant variations from that of the bulk. In bulk Te, CB1 forms a continuum with an infinite band width. For the wires and Te-h, CB1 splits into two bands, CB1(a) and CB2(b) , the bandwidth of CB2(b) for Te-h being infinite. For Te-w2, bands beyond 2.0 eV have not been obtained because of the intensive computational efforts involved.

The isosurfaces of charge density for Te-h arising from the states (-15 eV to

Table 3.3: Summary of band structure results. 'a' and 'b' denote the different VB2 and CB1 of Te-h and Te-w1, as shown in Figs. 3.4 and 3.5 respectively.

System	Band gap (eV)	Band width (eV)		
		VB1	VB2	CB1
Te bulk	0.15	5.44	5.83	∞
Te-w2	0.45	5.42	5.81	1.65
Te-w1	0.75	5.40	5.62	3.1 for (a) 2.6 for (b)
Te-h	1.64	4.43	2.21 for (a) 1.53 for (b)	1.63 for (a) ∞ for (b)

2.5 eV) at Γ point of the BZ are shown in Fig. 3.7. The VB1 band (Fig. 3.7(a)) describes electrons of predominantly s orbital character with slight mixing with the p orbital. Figs. 3.7(b) and (c) show the p-bonding and the p-lone pair orbitals character of the electrons. The electrons from p-antibonding orbital (with slight mixing of s orbital) are shown in Fig. 3.7(d). For Te-w1, Te-w2 and bulk Te the isosurfaces show similar features because the interaction between the atoms in the neighboring helices are very weak compared to intrahelical interactions.

3.5 Optical conductivity

Optical conductivity of nanowires strongly depends on their diameter and the direction of polarization of the incident light. We used Kubo-Greenwood [58, 59] formula to compute the optical conductivity tensor:

$$\sigma_{\alpha\beta}(\omega) = \frac{2\pi}{3\omega}\int_{BZ} dk \Sigma_{i,j}(f_i^k - f_j^k) \times \mid \langle\psi_i^k \mid \frac{\partial}{\partial x_\alpha} \mid \psi_j^k\rangle\langle\psi_i^k \mid \frac{\partial}{\partial x_\beta} \mid \psi_j^k\rangle \mid \delta(\varepsilon_j^k - \varepsilon_i^k - \omega) \tag{3.3}$$

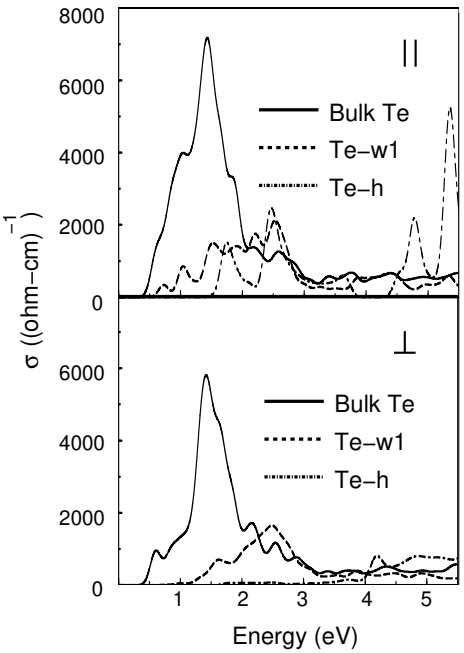

Figure 3.8: Optical conductivity plot for bulk Te, Te-w1 and a single helix at 300K for two directions of polarization of E: (a) E $\parallel$ c and (b) E $\perp$ to c.

where f_i^k is the Fermi-Dirac occupation, ω the energy of the incident photon, ε_i^k and $\mid \psi_i^k \rangle$ are the energy eigenvalue and the energy eigenfunction of the i^{th} band at the Bloch wavevector k, x_α is the α-component of position vector $\mathbf{r}$ and $\langle \psi_i^k \mid \frac{\partial}{\partial x_\alpha} \mid \psi_j^k \rangle$ is the interband transition matrix element. Eigenvalues of σ yield the optical conductivity along the three principal axes. The transition matrix elements are obtained using d/dk linear response module of the ABINIT code [38]. Whenever the energy of an incident photon matches a van Hove singularity in the DOS, subject to the selection rules given by the interband transition matrix element and the Pauli's exclusion principle, there is a resonant enhancement in the optical conductivity giving rise to its peaks. In our calculations of σ and imaginary part of the dielectric constant [see Eqn. (3.4) and Fig. 3.9 later] we employ a smoothening technique that replaces the delta function in Eqn. (3.3) with a Gaussian of width 0.01 eV.

Optical properties of bulk Te depend on the direction of polarization of incident light with respect to the c axis. The three principal components

of the conductivity tensor are: (i) σ_{cc}, along c axis, when the polarization direction of incident light and the current are parallel ($\|$) to the c axis, and (ii) $\sigma_{aa} = \sigma_{bb}$ (from crystal symmetry $a = b$), i.e., when the polarization of incident light and current are perpendicular ($\perp$) to c . For both directions of polarization, there is a distinct peak at around 1.43 eV (see Fig. 3.8). In addition to this peak, σ of bulk Te exhibits a hump at about 0.61 eV and a shoulder at about 1.03 eV when the polarization of incident light is $\|$ to c, and a peak at about 0.61 eV when the polarization of incident light is $\perp$ to c.

To compare our results with experimental data and other theoretical calculations, we compute the imaginary part of the dielectric constant ($\epsilon_{im}(\omega)$):

$$\epsilon_{im}(\omega) = \frac{4\pi}{\omega}\sigma^{real}(\omega). \tag{3.4}$$

Our results (see Fig. 3.9) are in good agreement with the experiments performed by Tutihasi *et al.* [60] except for the facts that (i) the theoretical peak is red shifted by about 0.5 eV and (ii) the value of ϵ_{im} corresponding to the peak is nearly twice that of the experimental value. To understand the origin of differences in the estimates of ϵ_{im} obtained from experiment and our calculations, we separate out the effects of the matrix elements and the density of states on ϵ_{im}. We determine the joint density of states (JDOS), given by the convolution of electronic DOS. From the comparison of JDOS with the work of Starkloff *et al.* [61] we find the interband transitions that give rise to various peaks. Overall features of the JDOS obtained from our calculations agree fairly well with that of Starkloff *et al.* The red shift in the position of peaks and the factor of about two in the value ϵ_{im} corresponding to these peaks primarily arise from the underestimation of band gap, typical of DFT calculations. While our calculations predict a band gap of 0.15 eV, the experimentally measured value of band gap is 0.33 eV. We note that our finding of the peak in ϵ_{im} at 1.43 eV is consistent with previous experimental measurements [60]

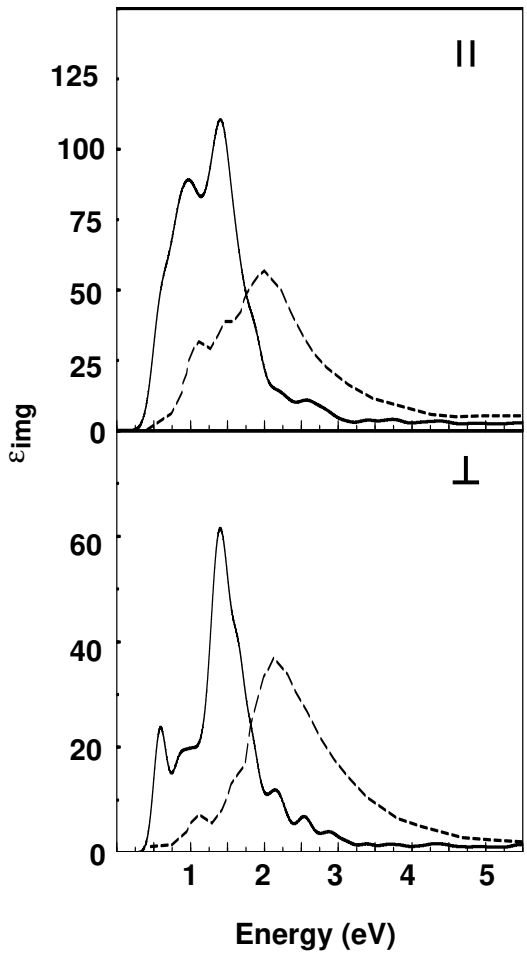

Figure 3.9: Imaginary part of dielectric constant ϵ for bulk Te at 300K, the upper and lower panel show ϵ when polarization directions of incident light are $\parallel$ and $\perp$ to c respectively. The solid line shows the theoretically calculated ϵ while the dashed ones are the experimentally measured value [60].

and calculations, [61] though it was not observed in the absorption spectra of bulk Te by Goutam *et al.* [6].

For nanowires, the splitting of bands results in sharper peaks than that of the bulk. Optical conductivity of Te-w1 and Te-h (Fig. 3.8) for polarization along the c axis exhibit many peaks. Positions of the peaks in σ for these two systems and the corresponding interband transitions are listed in Table 3.4. For both the directions of polarization of incident light, there is significant decrease in the magnitude of σ in comparison to that of bulk, which can be

Table 3.4: Transitions corresponding to different peaks in optical conductivity plot for E ∥ c.

System	Position of peak (eV)	Transitions
Bulk Te	0.61 1.03 1.43	VB2(b) → CB1
Te-w1	0.71 1.03 1.53 1.90 2.20 2.52	VB2(b) → CB1(a)
Single helix	1.75 2.48 3.63	VB2(b) → CB1(a)
	4.79 5.36	VB2(a) → CB1(a)

largely explained by the changes in band gap. In contrast to bulk Te and Te-w1, Te-h shows two distinct peaks at 4.8 eV and 5.4 eV, when direction of polarization of incident light and current are ∥ to c (top panel of Fig. 3.8). These peaks correspond to the electronic transitions from VB2(a) to CB1(a) and their origin can be explained from the band structure of Te-h (right panel of 3.4). VB2(a) and CB1(a) being almost parallel, cause an increase in the JDOS of Te-h, which results in the peaks in σ at the above mentioned values of ω.

In contrast to bulk Te, optical conductivity spectra of the nanowires exhibit very strong dependence on the direction of polarization of the incident light. For polarization of light ∥ to c, there are no peaks for Te-h below 1.49 eV (top panel of Fig 3.8). Peaks seen in bulk and Te-w1 below 1.49 eV arise from the interchain hopping of electrons. Since Te-h has a single helix, there is no contribution in optical conductivity from interchain hopping of electrons, resulting in the absence of those peaks. The spectra for Te-h for σ_{aa} (lower

panel of Fig 3.8) shows negligible optical conductivity below 4.0 eV, followed by a small peak at 4.19 eV, whereas Te-w1 and bulk shows noticeable conductivity below 4 eV. This shows that the interchain interactions play a prominent role in the size dependance of σ_{aa} of nanowires.

3.6 Summary

We have studied effects of the thickness of the nanowires of Te on their geometry, surface energy, Young's modulus, electronic structure and optical conductivity using the *ab initio* density functional theory calculations.

Reduction in the coordination number of the atoms at the surfaces of nanowires result in (a) rearrangement of atoms at the surface, (b) stronger intra-helical Te-Te bonds and reduction in the lattice parameter c with decreasing size, (c) changes in the inter helical distances d by approximately 1% and (d) subsequently in the reduction in Young's modulus. These structural changes correlate with decreasing overlap of electronic wavefunctions of different helices, and the electronic structure of nano-wires exhibits a blue shift in the band gap with decreasing diameter of the wires. In contrast to the bulk Te, optical conductivity of its nano-wires is strongly dependent on the direction of polarization of the incident light. Due to lack of hopping between helices, for light polarized perpendicular to its axis, optical conductivity of Te-h is significantly lower in comparison with other nano-wires or bulk Te.

Chapter 4

The Origin of Stability of Helical Structure of Tellurium

4.1 Introduction

The presence of helical structures among inorganic solids is an intriguing rarity. Elemental Tellurium (also Selenium), a group VI-A element with filled $5s$ and a partially filled $5p$ orbital, shows an interesting crystal structure: bulk Te forms trigonal crystal (t-Te) consisting of parallel helical chains stacked on a triangular lattice, with their axes parallel to the crystalline c axis. The space group of the crystal is D_3^4 and D_3^6 depending on the sense of rotation of the helical chain. Te nanowires, synthesized recently [6], also exhibit helical structure. It is fundamentally interesting to investigate the cause for stability of helical structure of Te.

In addition to the presence of helical chains in bulk Te and Se, S, Se and Te also form stable clusters with helical ring-like structures. S_8 cluster of sulphur in which the S atoms are arranged in a puckered ring-like structure is known to be highly stable. It can occur in solid, liquid and gaseous states. S_8 also forms the building blocks of bulk S in its stable rhombic phase. Se

clusters occur in a vapor phase, in crystalline modifications and also in liquids. Steudel *et al.* [62, 63] found that at 800 K, Se vapor consists primarily of Se_5, Se_6 and Se_8 rings. Mass spectroscopic studies of Willey *et al.* [64], Benamar *et al.* [65] and Ito *et al.* [66] on Te vapor suggested that Te vapor consists of Te_2 and Te_5 predominantly. There had been several theoretical studies on the determination of ground state structures of small Te clusters [67–69, 71]. From their theoretical calculations, Li *et al.* [70] showed that Se_6 and Se_8 are more stable than their adjacent molecules and suggested that these clusters can be used as building blocks to assemble various low dimensional new materials. While understanding the stability of the helical structure of bulk Te, it is also interesting to understand the stability of Te clusters.

In this work, we use first-principles (non-empirical) calculations to understand the origin of stability of helical structure in terms of electronic orbitals and bonding, and also probe the potential of Te nanowires for practical applications. In Section 4.2, we describe the details of the first principles calculations, and present a comparison of our results for structural parameters and cohesive energy of bulk Te with other calculations and experiments. We present our results on the stability and energetics of Te clusters in Section 4.3. In Section 4.4 we determine the chemical origin of the stability of the helical structure through use of Wannier functions. We present results for vibrational spectra of bulk Te and an infinite Te helix in Section 4.5.1. In Section 4.5.2 we examine evolution of helical structures of Te from an infinite linear chain of Te atoms. We discuss the stability of bulk Te with respect to slip and stretch deformation in Section 4.6, and conclude in Section 4.7.

4.2 Details of first-principles calculations

We have used ABINIT [38, 39] implementation of density functional theory. The details regarding the pseudopotential and the exchange-correlation functional used to perform these calculations are the same as those presented in Chapter 3. For bulk Te and the nanowires, we have used 5×5×5 and 1×1×5 Monkhorst-Pack [22] k-point meshes respectively to sample integrations over the Brillouin zone (BZ). For calculations of clusters we have used the $\Gamma-$point [k=(0,0,0)] only.

For a comparative analysis, we have carried out calculations for bulk Te (3 atoms/cell), a single-shelled Te wire (Te-w1) with 21 atoms per cell and a diameter of about 14 Å, an infinite helix (Te-h) with 3 atoms per unit cell and a diameter of about 3.2 Å a linear chain of Te atoms (Te-lc) having only one atom per unit cell and Te clusters of different sizes ($n \leq 12$, n denotes the number of Te atoms in the cluster). Te-w1, Te-h and Te-lc are periodic in $c-$direction but confined in the $ab-$plane for which we used hexagonal supercell with an in-plane lattice parameter a of about 40 Å, with a vacuum of about 10 Å. For helices of finite length, this supercell is expanded along the c-axis to 28 Å. For other clusters cubic supercells of size varying from 15 Å to 27 Å have been used. The size of supercells ensures negligible interaction among periodic images of clusters separated by vacuum.

To benchmark our method, we have first determined the bulk structure of t-Te. Our results for bulk Te have been presented in the previous chapter.

In order to determine the lowest energy structures of clusters we have tried several initial geometries, based on results of previous calculations available in the literature [71]. For Te_2 the question of choosing initial configurations does not arise. For clusters with $n \geq 4$ we have chosen three types of initial guesses: (i) the atoms arranged in a finite helix (FH), (ii) the atoms arranged in a non-planar ring-like geometry (RC), which represents a FH with its open

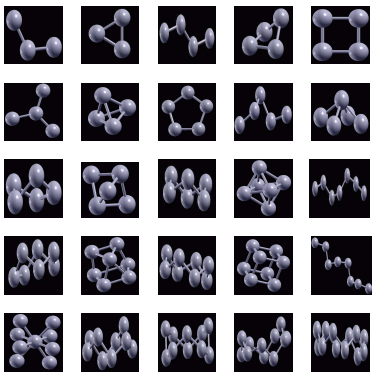

Figure 4.1: Different geometries for clusters, n≤12

ends closed and (iii) various polyhedral cage (PC) structures. For $n \leq 5$ we have also considered high symmetry planar geometries such as triangular for Te_3, square for Te_4 and pentagon for Te_5.

4.3 Clusters: energetics and stability

From the final geometries obtained after minimization of energy (see Fig. 4.1) and the cohesive energies of the clusters (listed in Table 4.1), we determine the factors affecting the stability of different Te structures. Among the various structures of Te_4 clusters, the tetrahedral (tet-PC) structure is the least stable with the smallest cohesive energy (E_c), followed by the planar, square and FH. The reason behind a lower E_c of PC and the planar geometries can be attributed to a higher coordination number (CN) of 3 of Te atoms compared to the preferred CN of 2. Among the Te_4 structures with the CN of 2, the square one is least stable. This suggests that an angle of 90^0 is not energetically favored. Between FH and RC, the RC is the most stable configuration because unlike FH it does not have free ends, i.e., in RC all Te atoms have a CN of 2 while in FH the Te atoms at the two ends of the helix have a CN of 1.

Based on the same line of argument, stability of clusters with different geometries for a particular n can be understood. For clusters with six atoms,

Table 4.1: Cohesive energy of Te clusters. For the infinite helix (Te-h) the cohesive energy is 2.33 eV/atom.

No. of atoms	E_c (eV/atom)
2	1.54
3 (RC)	1.95
3 (FH)	1.89
4 (RC)	2.08
4 (FH)	2.07
4 (square)	1.95
4 (planar)	1.71
4 (tet-PC)	1.36
5 (RC)	2.26
5 (FH)	2.07
5 (planar)	1.96
5 (sqp-PC)	1.84
5 (radial)	1.72
6 (RC)	2.30
6 (oct-PC)	1.52
7 (RC)	2.32
7 (FH)	2.17
8 (RC)	2.36
8 (FH)	2.12
8 (cube-PC)	1.91
9 (RC)	2.33
9 (nan)	1.61
10 (RC)	2.30
11 (RC)	2.32
12 (RC)	2.33

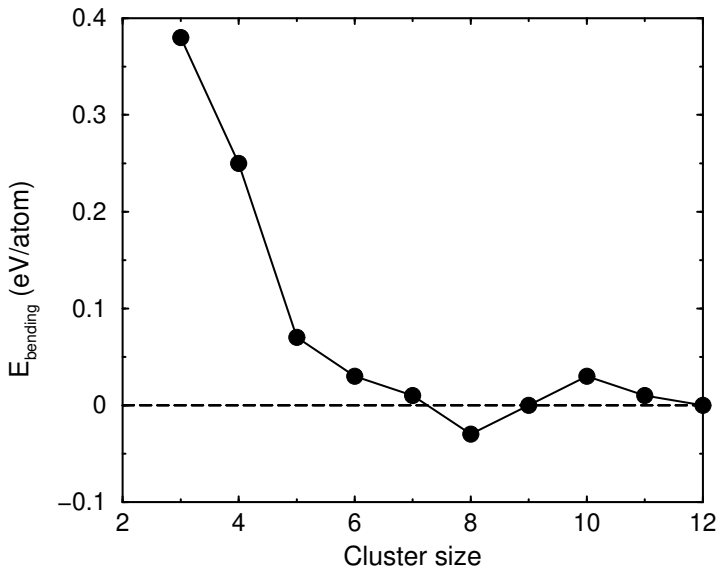

Figure 4.2: The bending energy, as a function of cluster size required to form RCs from FHs.

there is a large difference in cohesive energy (ΔE_c) between RC and an octahedral (oct-PC) structure (Table 4.1). This is also because of a greater coordination number of Te atoms in oct-PC (4 for each atoms). Thus, two factors affect the stability of Te clusters with different geometries (a) the Te-Te-Te bond angle and (b) the coordination no of Te atoms in the clusters, with preference to two. Since an RC can be thought of as a bend FH with their ends joined, it is interesting to calculate the energy cost ($E_{bending}$) associated with bending an FH. In terms of the cohesive energy per atom, $E_{bending}$ is given by:

$$E_{bending} = -(E_c^{RC} - E_c^{Te\text{-}h}) \tag{4.1}$$

where E_c^{RC} and $E_c^{Te\text{-}h}$ are the cohesive energy per atom of an RC of n atoms and an infinitely long helix respectively. Interestingly $E_{bending}$ of Te_8 is -0.03 eV/atom (Fig. 4.2), revealing the instability of a finite helix structure of Te_8 with respect to bending. Like Se_8 and S_8, the RC structure of Te_8 is most

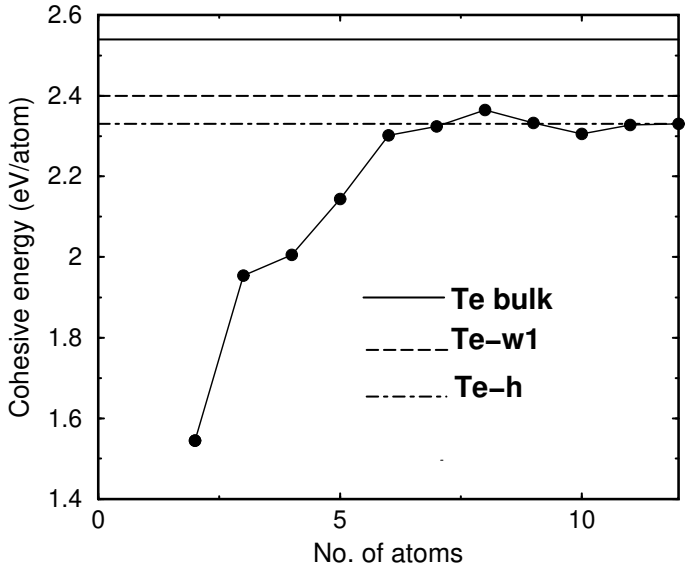

Figure 4.3: Cohesive energies of clusters of different sizes and their comparison with bulk Te (solid line), Te-w1 (dashed line) Te-h (dashed-dot line).

stable among the Te_n clusters. It lies lower in energy compared to that of FH, the one with cubic structure and even Te-h (Fig. 4.3).

4.4 Bonding orbitals and stability of helical structure

With the knowledge that the Te-Te-Te bond angle and the coordination number of Te atoms play an important role in the stability of the Te clusters, we now determine its chemical origin in terms of the nature of bonding in Te-h. Character of chemical bonds in extended systems can be determined by constructing Wannier functions(WF) which naturally represent the bonding orbitals. As Te-h is a one dimensional system we obtain its WFs for composite bands using an approach based on parallel transport and non-abelian geometric phases [72]. We obtain the transformed band structure (TBS) where the energy bands labeled by WFs indices describe energy eigenvalues in the given

subspace of bonding orbitals, analogous to term energies of bonding orbitals. In contrast to the usual energy band structure (Fig 4.4(c)), the TBS [Fig. 4.4(d)] reveals two distinct group of bands. The bands in the electronic band structure arise from mixing among bonds, i.e., bands in TBS. Higher energy band in the TBS has contributions mainly (73%) from the upper 6 bands in the electronic structure. The lower energy band in the TBS has almost equal contributions from the group of 3 bands lower in energy and 6 high energy bands in the electronic band structure. We find three σ bonds (Fig. 4.4(a)) formed by sp hybridized orbitals of Te atoms, which correspond to the three lower energy bands in the TBS which are almost degenerate. WFs corresponding to the upper band having a degeneracy of six are predominantly p like (Fig. 4.4(b)) exhibit two-lobe structure and involve three neighboring Te atoms. For each of them, one of the two lobes occupies the space surrounded by the three atoms, reflecting character of a π-like bonding between p states of three Te atoms. The presence of σ bonds results in the preference of coordination number of 2 for Te. The three center π-like bonding character results in the Te-Te-Te bond angle which makes the helical structures stable.

For Te-w1 the WFs are modified due to the presence of interhelical interactions as shown in Fig. 4.5. The lobes of σ bonds get distorted [Fig. 4.5(a)]. The lobe of the π-like lone pair orbitals which spreads over the neighboring Te atoms are also modified. Moreover there is a reduction in the spread of the WFs (Fig. 4.5(b)).

4.5 Local stability: structural distortions

4.5.1 Vibrational spectra of bulk Te and Te-h

To analyze the stability with respect to internal structural distortions, we have computed the vibrational spectra of Te-h and compared it with that of bulk

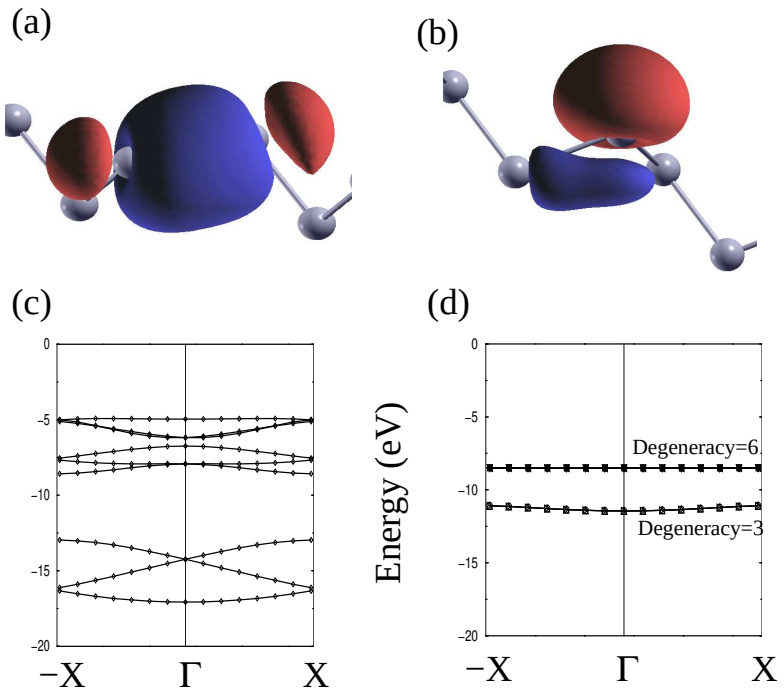

Figure 4.4: WFs of Te-h showing σ bonds (a) and p like lone pair orbitals (b). The lower panels show its electronic structure (c) and the TBS (d).

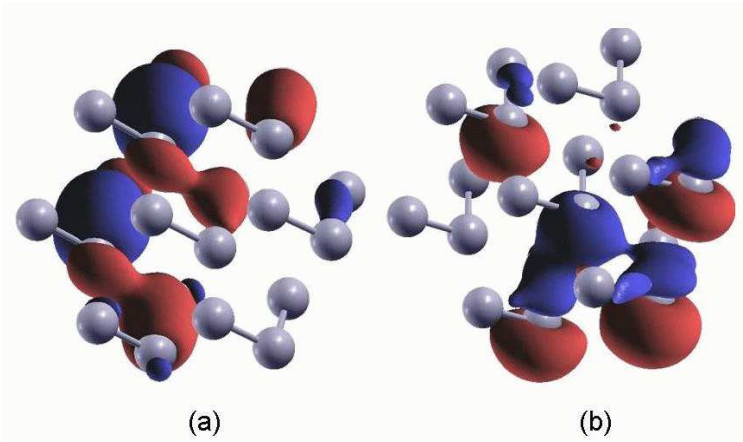

Figure 4.5: WFs of Te-w1 showing the modified σ bonds (a) and p like lone pair orbitals (b) due to interhelical interactions.

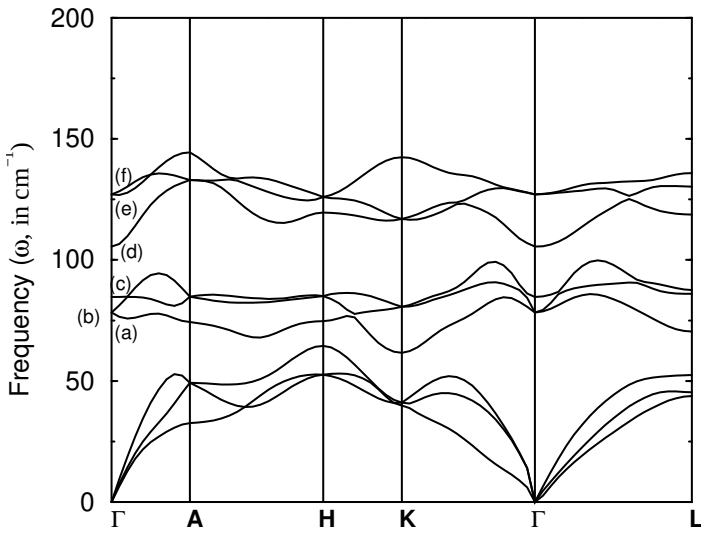

Figure 4.6: Phonon dispersion curves of bulk Te along the high symmetry directions of the BZ. (a)-(f) denote the optical modes at Γ−point.

Te.

Our calculated phonon spectrum of bulk Te along the high symmetry directions (see Fig. 4.6) agrees reasonably well with that of Martin *et al.* [73]. Among the displacement patterns corresponding to the six optical modes at the Γ−point (shown in Fig. 4.7), (a) and (b), and (e) and (f) form pairs of doubly degenerate modes. These modes correspond to a mixture of bond-stretching and bond-bending. Mode (c) corresponds to rotational motion of the helix. Mode (d) is the mode in which each atom moves in the radial direction in the basal plane leading to diametric expansion/contraction.

We present phonon dispersion curves and the displacement patterns corresponding to the optical modes of Te-h in Fig. 4.8 and Fig 4.9 respectively. We find that Te-h has stable modes throughout the BZ. The absence of unstable modes (no modes having imaginary frequency) confirms that Te-h structure is locally stable. We find that frequencies of two of the acoustic branches vary quadratically with wave vector near Γ. This type of variation is typical for one-dimensional systems. Through comparison of modes of Te-h at Γ with those of bulk Te, we find that certain modes are softened (lower in energy)

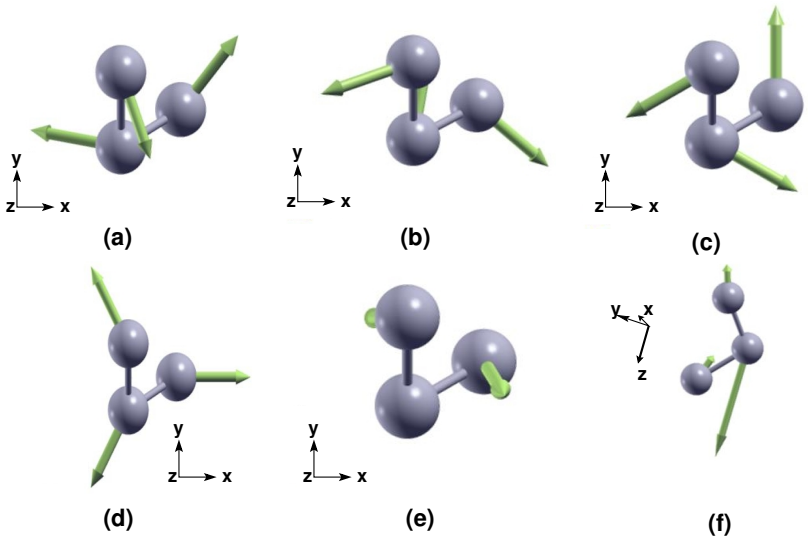

Figure 4.7: Displacement patterns of phonon modes at Γ for bulk Te.

while others are hardened (higher in energy) in Te-h with respect to those of bulk Te. The rotational mode (c) with energy 78.32 cm^{-1} in bulk is lowered drastically to 3.77 cm^{-1} in Te-h. The softening of this mode is due to the absence of inter-helical interactions in Te-h. The difference in energy between these two modes (∼9 meV) gives an estimate of the strength of inter-helical interactions in bulk Te (3 meV). The modes which corresponds to the mixture of bond-stretching and bond-bending are hardened because the Te-Te bonds are stiffer in Te-h (Te-Te bond length of 2.74 Å [74]) than in the bulk Te (Te-Te bond length of 2.91 Å [74]). We note that the chain expansion mode [mode (d)] observed in bulk Te is absent in Te-h.

4.5.2 From linear chain to the helical structure

To gain further insight into how helices are stabilized in Te, we have studied how the helical structure evolves from an infinite linear chain of Te atoms (Te-lc). While the Te-h, with 3 Te atoms in the unit cell, has optimized c and u of 5.69 Å and 1.14 Å respectively, Te-lc has one atom per unit cell, with $u = 0.0$. The position of the atoms of Te-h in the unit cell are $(u, 0.0, 0.0)$,

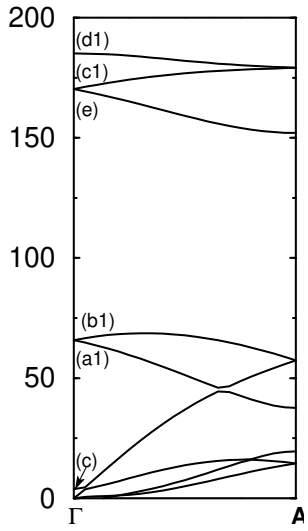

Figure 4.8: Phonon dispersion curves of Te-h. a1, b1, c1, d1, c and f denote the optical modes at Γ−point.

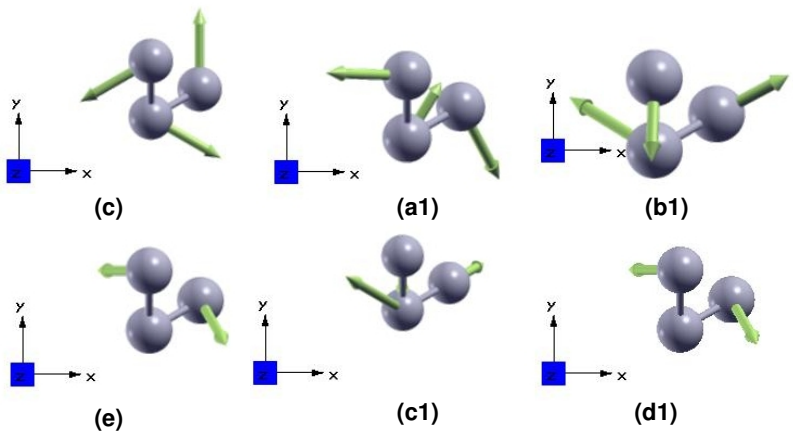

Figure 4.9: Displacement patterns of phonon modes at Γ for Te-h

$(-\frac{u}{2}, -\frac{\sqrt{3}u}{2}, \frac{c}{3})$ and $(-\frac{u}{2}, \frac{\sqrt{3}u}{2}, \frac{2c}{3})$. As mentioned before, u corresponds to the displacement of atoms in the $ab-$plane and a non-zero value of u results in introduction of chirality in Te-lc. We determine c (also bond length) of Te-lc to be 2.76 Å. Corresponding value of c for a 3-atom supercell of Te-lc (c=8.28 Å) is much greater than that of Te-h. To investigate the stability of Te-lc we calculated its phonon frequencies. We find unstable modes at the phonon wave vectors $q = 0.33\frac{2\pi}{c}$ and $0.50\frac{2\pi}{c}$, showing that Te-lc is not stable. While at $q = 0.33\frac{2\pi}{c}$ there are two unstable modes which are energetically degenerate, at $q = 0.50\frac{2\pi}{c}$ all the three acoustic modes are unstable. A linear combination of the two transverse degenerate modes represent a chiral acoustic wave. Keeping c of Te-lc fixed at 2.76 Å and taking a super cell comprising of three unit cells along c, we displaced the atoms in the $ab-$plane located at $(0.0, 0.0, 0.0)$, $(0.0, 0.0, \frac{c}{3})$ and $(0.0, 0.0, \frac{2c}{3})$ to $(u, 0.0, 0.0)$, $(-\frac{u}{2}, -\frac{\sqrt{3}u}{2}, \frac{c}{3})$ and $(-\frac{u}{2}, \frac{\sqrt{3}u}{2}, \frac{2c}{3})$ respectively, and determined its energetics (see inset of Fig 4.10). We find that Te-lc relaxes to a geometry with $u = \pm 0.32$ Å. However in that geometry the σ_{zz} component of the stress tensor is about 0.63 GPa, suggesting that: (i) there is a coupling between u and the strain tensor (ϵ_{zz}) and (ii) c is not fully relaxed. If we now fix the c of the supercell of Te-lc to 5.69 Å (c of Te-h), and displace the three Te atoms as before, we find that at u=0.0 the total energy of the linear chain (see Fig 4.10) is much higher than its value when Te-lc is at its own optimized c value. The increase in energy of the strained Te-lc reflects the effect of the huge compressive strain (31.28%) the linear chain is subject to when it is forced to be at c=5.69 Å. The effects of the strain are also reflected in the phonon frequencies: the phonon frequencies at $q = 0.33\frac{2\pi}{c}$ of the Te-lc at its optimized c are $82.66i$ and 178.09 cm^{-1}. However, when Te-lc is compressed to the c of 5.69 Å, the phonon frequencies increase to -403.63i and 916.81 cm^{-1} respectively. On distorting the compressed Te-lc, we find that the system is at its minimum when u=1.14 Å, attaining the geometry of Te-h. A comparison of the energetics (Fig. 4.10) of strained and unstrained Te-lc clearly shows the

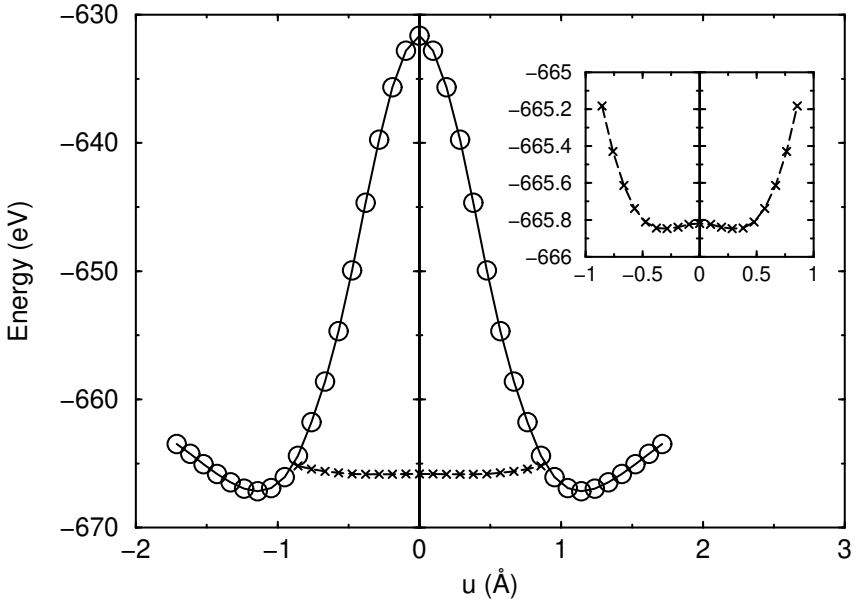

Figure 4.10: Total energy vs. u for a supercell of Te-lc consisting of three unit cells along the c axis at two values of c: (i) the solid black line with open circles corresponds to case when c=5.69 Å and (ii) the dashed line with crosses corresponds to the case when c of supercell is three times the optimized value of c for Te-lc. The inset shows the magnified form of case (ii).

spectacular effects of strain on Te-lc. Unlike the unstrained Te-lc, in which the atoms are displaced in the $ab-$plane by 0.32 Å, the stress corresponding to the structure of the compressed Te-lc in which the atoms are displaced by u=1.14 Å is zero, and the latter is also lower in energy. We therefore conclude that a strong coupling between strain and the transverse chiral acoustic wave stabilizes the structure of Te-h.

4.6 Stability of slip and stretch deformation

Te nanowires exhibit optical conductivity at high frequencies (beyond 2 eV) [74] opening up a possibility of their use in devices. For feasibility of device applications, mechanical stability plays an important role.

We determine two energies relevant to mechanical stability: (a) surface

energy (γ_s, energy per unit area of the surface) and (b) an energy analogous to the unstable stacking fault energy (γ_{us}, defined here as the lowest energy barrier that must be overcome when one helical chain slides over the the others, while the crystal is brought from one equilibrium position to another) have been calculated. In order to determine γ_{us} of the, bulk we consider a supercell as shown in Fig. 4.11(a) and a helix at one of the corners is pulled along c axis. γ_s is obtained by simulating crystal with a periodic supercell (Fig. 4.11(b)) and introducing vacuum between neighboring planes and increasing c axis till a cleavage occurs at the ab-plane of the crystal. These energies are fit to the universal binding energy (UBE) function [75]

$$e(d) = \frac{E(d)}{A} = e_\infty - 2\gamma_s(1+f)e^{-f}, \tag{4.2}$$

where $f = (d - d_0)/\lambda$, e_∞ is the energy per unit area (A) of the cleaved crystal, d_0 is the interplanar separation in the equilibrium bulk crystal and λ a fitting parameter. For bulk Te, we find γ_{us} and γ_s to be of 0.52 and 0.42 J/m^2 respectively.

For Te-h (which is 1-D) γ_{us} cannot be defined. So we focus only on γ_s with a supercell similar to that of Fig. 4.11(a), with c of Te-h. Interestingly the UBE function (Eqn. 4.2) does not fit our calculated data (Fig. 4.11(d)), departing from the UBE curve when d-d$_0$ $\approx$ 1.37Å. The γ_s for Te-h is 0.13 J/m^2. Examining the structure we find that the helix breaks up when d-d$_0$ is increased beyond 24% of c.

4.7 Conclusion

We have investigated the stability of helical structure of Te in its bulk, and nanowire forms, and its electronic origin. Amongst the Te clusters which we have studied, the ring like geometry is most stable for all n. The cohesive

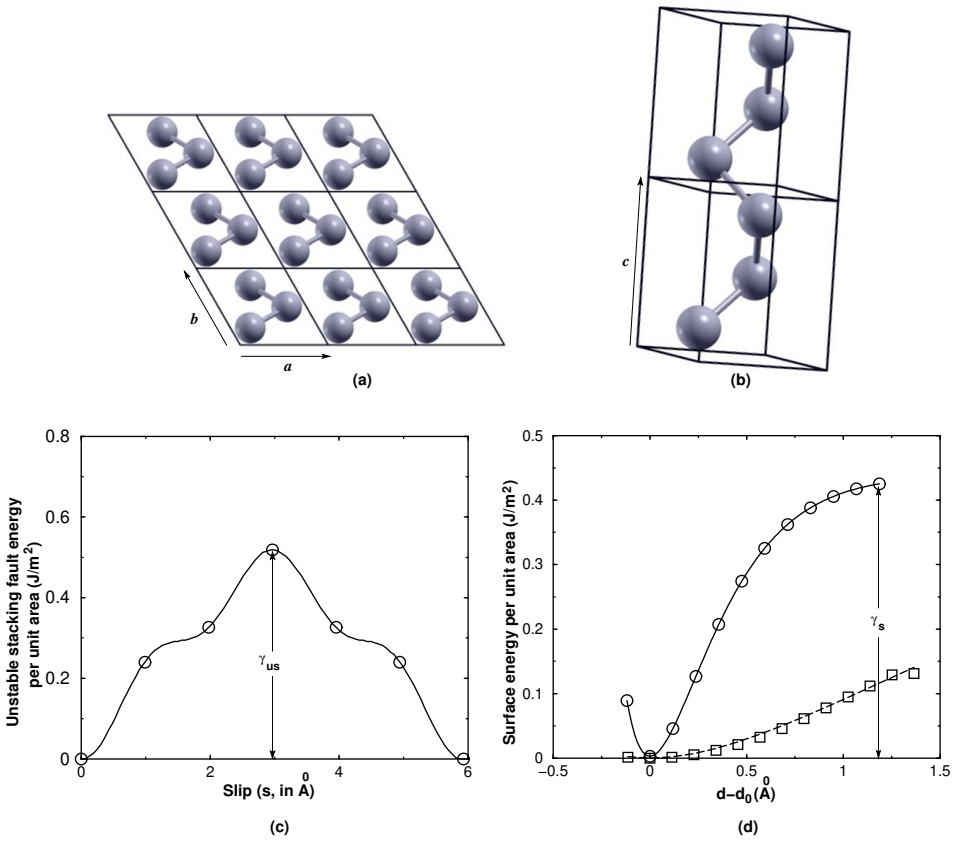

Figure 4.11: (a) and (b) show the supercells used to calculate γ_{us} and γ_s respectively, for bulk Te. (c) gives γ_{us} for bulk Te. In (c) the open circles are the calculated values of unstable stacking fault energy per unit area for different s and the solid line is the fitted curve. (d) gives γ_s for bulk Te. In (d) the open circles are the calculated values of surface energy per unit area for different (d-d_0) and the solid line is the fit to the universal binding energy equation (Eqn. 4.2) for bulk Te. The open squares and the dashed line are the calculated and fitted values of the surface energy per unit area at different (d-d_0) respectively for Te-h.

energy of Te_8 is highest; it is even higher than that of Te-h. From the study of WF's, we find that σ bonds between two Te atoms favor a 2-fold CN and 3-centre π-like bond favors the angle essential to the helical structure of Te. To asses the local stability of Te-h we have studied its vibrational spectrum. The absence of imaginary frequency modes throughout the BZ confirms that Te-h is locally stable. In comparison with bulk, certain modes are softened while others are hardened. From the energy difference between the rotational modes of Te-h and bulk Te we estimate of the inter-helical interaction energy to be about 3.0 meV. Through the study of the stability of Te atoms arranged in a linear chain we suggest that the coupling between strain and chiral acoustic wave plays an important role in stabilizing the helical structure.

Chapter 5

Lifting of Ir{100} Reconstruction by CO Adsorption

5.1 Introduction

Transition metals such as Rh, Pt and Ir act as catalysts in many important reactions. The catalytic oxidation of harmful vehicular exhausts such as CO on these metal surfaces is certainly one of the most important reactions. Moreover, in response to reduced coordination, the {100} surfaces of face centered cubic (fcc) metals Au, Pt and Ir reconstruct to form a corrugated quasi-hexagonal overlayer (hex) on top of the square fcc substrate. Surface adsorbates like CO, NO and O_2 are known to lift the reconstruction on Pt{100} and Ir{100} (A brief summary of the previous experimental and theoretical studies related to the reconstruction of Ir{100} surfaces is given in Section 5.2.1). The onset of lifting of the reconstruction depends on the adsorbate coverage. During a catalytic cycle the surface alternates rapidly between being CO-rich and (after the CO has combined with oxygen to form CO_2) being

clean. Thus, the surface alternates also between being unreconstructed and reconstructed, and the thermodynamics and kinetics governing this process are of great interest if one wishes to gain a better understanding of the catalytic cycle.

The parameters that characterize the process by which the reconstruction is lifted are: (i) the adsorbate coverage on the metal surface, (ii) the nucleation of unreconstructed (1×1) islands, and (iii) the growth rate of these islands. The mechanism behind the lifting of the reconstruction is not well understood. It has been observed that even though the lifting of the reconstruction sets in at a low total coverage of about 0.1 ML, the local coverage on the growing (1×1) islands is very high (0.5 ML). It is also not clear from the literature whether the nucleation of the (1×1) islands is homogeneous or heterogeneous. The growth rate of (1×1) islands follow a non-linear power law which results in oscillations in the reaction rates.

As a first step towards understanding the phenomenon of the lifting of the reconstruction of Ir{100} by CO adsorption, our work aims at understanding the thermodynamics behind this process. In the rest of the chapter we will address the following questions: (i) what is the total CO coverage for the onset of restructuring? (ii) why is the local CO coverage on the growing (1×1) islands so high?, (iii) what is the driving force behind the lifting of the reconstruction? To extend the conclusions to finite temperature and pressure conditions, the results are fed into an analysis using the entropy and the chemical potential.

The rest of the chapter is divided as follows: Section 5.2.1 gives a brief review of the previous experimental and theoretical work related to the reconstruction of the Ir{100} surface and the lifting of its reconstruction by molecular adsorbates; in Section 5.3 we provide a description of how we model the surface unit cells of the unreconstructed and reconstructed surfaces, and other related details of the DFT calculations; we present our results in Section

5.4. Finally we discuss the implications of our results and summarize them in Section 5.5.

5.2 Previous work

5.2.1 Reconstruction of Ir{100} surface

When a surface is created there is a reduction in coordination number of the surface atoms in comparison with that of the bulk. As a result, the atoms rearrange themselves, sometimes producing a structure that differs from that of the bulk terminated surface. This rearrangement of surface atoms is called *surface reconstruction*. Surfaces undergo different types of reconstruction [2]. There may be lateral displacements of atoms within the surface layers at constant layer density (e.g., displacive reconstruction) or change in the surface layer atomic density (e.g., hex reconstruction or missing row reconstruction). The present work deals with a Ir{100} surface which undergoes a hex reconstruction.

In hex reconstruction, the increase in the surface layer atomic density results in a considerable buckling of the surface layers. This type of reconstruction was first observed in Pt{100} surfaces [80]. In addition to Pt{100}, Au and Ir {100} surfaces also undergo similar reconstruction. While Pt{100} and Au{100} display complex periodic patterns [with (5×29) and c(26×68) unit cells respectively], Ir{100} has a similar structure with a comparatively small (5×1) unit cell. Since the smaller unit cell of Ir{100} makes it easily accessible to *ab initio* calculations, we have chosen to study the lifting of the reconstruction by CO on Ir{100}. However, the structural similarity of the reconstructions on Pt{100} and Ir{100} suggests that the chemical reactions and physical processes taking place on the two surfaces might have similar mechanisms.

In the (5×1) unit cell of Ir{100}, the density of atoms in the surface layer increases by 20%. While the (5×1) unit cell of the bulk truncated surface has five atoms in the outermost layer, the outermost layer of a similar unit cell of hex-reconstructed Ir{100} surface has six Ir atoms in it. There are two possible top-to-second layer registries: (a) "two-bridge model", in which two of the six atoms occupy precise bridge positions and (b) "centre-top model", in which out of the six atoms, two atoms occupy an atop position and a hollow position. However, low energy electron diffraction (LEED) studies by several groups [81–83] have shown that the "two-bridge model" is favoured. They have also quantitatively determined the top layer's buckling which has been induced by the incommensurate substrate. Similar observations have also been made by Gilarowsky *et al.* [84] using scanning tunnelling microscopy (STM). From LEED measurements, Gruyters *et al.* [85] have observed that in addition to the top layer, the layer below it (second layer) is also buckled. They measured the overall buckling amplitude of the top layer and the second layer as 0.5 and 0.09 Å respectively. Recent LEED measurements by Schmidt *et al.* [86] have shown that the lack of registry between overlayer and substrate atoms results in a perceptible buckling in the top four layers, as well as a lateral shift in the topmost layer and the layer below it. In order to find out the driving force behind the reconstruction, Lehwald *et al.* [87] have measured the frequencies of surface phonons using high resolution electron energy loss spectroscopy (HREELS), and fed the phonon frequencies into a lattice dynamical calculation in a second-nearest-neighbor force-constant model. From their studies they have concluded that the release of surface stress is the driving force for the surface reconstruction of Ir{100}.

In addition to the above mentioned experimental studies, the reconstruction of Ir{100} has also been theoretically studied using DFT. A comparative study of {100} fcc transition metal surfaces of 5*d* (Ir, Pt and Au) and 4*d* (Rh, Pd and Ag) elements, using DFT, has been performed by Fiorentini *et*

al. [88] to understand the driving mechanism for the reconstruction. Their study suggests that the reconstruction results from a balance between surface-substrate mismatch and stress related energy gain. They found that only for the 5*d* {100} metal surfaces the stress related energy gain is large enough to drive the reconstruction against the substrate resistance to misregistry. Further calculations by Filippetti *et al.* [89] have shown that on the reconstructed surface, even though there is relief of stress along the [110] direction, the stress along $[1\bar{1}0]$ increases. They have argued that the in-plane stress in the surface layer of the reconstructed phase contains contributions from both the driving force and the resisting forces in proportions that cannot be disentangled. Hence a direct comparison of the in-plane stress of the clean and reconstructed surface may not be really helpful in determining the driving force for the hex-reconstruction. Ge *et al.* [90] have performed DFT calculations to determine the energy and structure of the two phases of Ir{100}. They have reported the reconstruction energy [energy difference between the (1×1) phase and the (5×1) phase] to be -0.01 eV/(1×1 area) and 0.06 eV/(1×1 area) using LDA and GGA respectively. Thus the use of LDA incorrectly predicts clean Ir{100} to be stable against reconstruction. Their results differ from that of Filippetti *et al.* [89] who have reported a surface energy difference of 0.14 eV/(1×1 area) using LDA. However it is to be noted that Filippetti *et al.* used a very small vacuum (equivalent to three layers) for the (5×1) phase which may introduce errors in their calculations.

5.2.2 Lifting of reconstruction by CO adsorption on Ir{100} surface

As mentioned above, surface adsorbates such as CO, NO and O_2 are known to lift the reconstruction on Pt{100} and Ir{100}. For Pt{100}, the adsorbate-induced lifting of the reconstruction has been widely investigated [91–95].

There have also been a few studies on the lifting of reconstruction on Ir{100} by molecular adsorbates [96–100]. Measurements of heats of adsorption, on both unreconstructed and reconstructed Pt{100} and Ir{100}, by Hopkinson *et al.* [93], Yeo *et al.* [99] and Ali *et al.* [96], have shown that the binding energy of CO is greater on the unreconstructed surface than the reconstructed one; this provides the driving force for the lifting of the reconstruction upon adsorption of CO. In the next few paragraphs we summarize the present state of knowledge regarding lifting of the reconstruction in the light of CO coverage, the nucleation of unreconstructed (1×1) islands, the growth rate of these islands and the mechanism behind the lifting of the reconstruction.

Coverage: What is the coverage of CO on the (1×1) islands, and at what critical coverage is the lifting initiated? Is the critical parameter the *global* CO coverage, or is it a *local* CO coverage (that differs from the average value) that is important? In experimental investigations of the restructuring process on Ir{100} and Pt{100}, it has been reported that the local CO coverage on the growing (1×1) islands is 0.5 ML [96]. However, the critical value of the total CO coverage, for the onset of the transition, has been found to be much lower than this, on both Ir{100} and Pt{100}. For example, thermal energy atomic scattering measurements on Ir{100} and Pt{100} suggest that the restructuring begins somewhere between 0.05 and 0.13 ML on Ir{100} [96], and between 0.01 and 0.03 ML on Pt{100} [93]; while electron energy loss spectroscopy measurements by Behm *et al.* [101] and Rutherford back scattering measurements by Jackman *et al.* [102] on Pt{100} have indicated that the lifting of the reconstruction is initiated at a critical CO coverage of 0.05 ML and 0.08 ± 0.05 ML respectively. When the total CO coverage is 0.5 ML, the entire surface appears to be in the (1×1) phase.

Nucleation: It is not clear from the literature whether the nucleation of (1×1) islands is homogeneous or heterogeneous. On the one hand, the finding

of similar CO adsorption energies on steps and terraces reported by Hopster *et al.* [103] indicates that the nucleation may be homogeneous. Using STM, Ritter *et al.* [94] have proposed that homogeneous nucleation of the (1×1) islands takes place due to fluctuations in the density of CO molecules. According to them, when the islands grow beyond a critical size, they become stable and act as nucleation centers. The spatial progress of the transformation occurs when the rate of growth of the islands becomes large compared to their rate of nucleation. On the other hand, STM studies by Borg *et al.* [104] suggest that the restructuring is initiated by heterogeneous nucleation, the nucleation centers being step edges and structural irregularities disrupting the hexagonal structure along a direction close to the [$\overline{1}$ 5] In agreement with this, molecular dynamics (MD) simulations by van Beurden *et al.* [95,105] of the lifting of the reconstruction on Pt{100}, at CO coverages between 0.4 and 0.5 ML, indicate that the transformation is heterogeneously nucleated at step edges aligned along the [011] direction.

Growth rate: From their molecular beam experiments, Hopkinson *et al.* deduced how $r_{1\times1}$, the growth rate of the (1×1) islands, depends on the local CO coverage on the hex-surface ($\Theta_{CO}^{\mathrm{hex}}$). They obtained a non-linear variation of the growth rate: $r_{1\times1} = k(\Theta_{CO}^{\mathrm{hex}})^n\Theta_{hex}$, where k is independent of $\Theta_{CO}^{\mathrm{hex}}$, Θ_{hex} is the fraction of surface remaining in the reconstructed form, and the reaction order n was found to be 4.5 ± 0.4. From this, they concluded that 4 to 5 CO molecules must be involved *cooperatively* in the growth of the (1×1) phase. Similar studies by Ali *et al.* [96] of the CO-induced lifting of reconstruction on Ir{100} also showed a power law behavior for the growth of (1×1) islands, with $3.9 \leq n \leq 5.8$. Recent time-resolved reflection absorption infrared spectroscopy (RAIRS) results indicate a similar power law relationship by an alternative, and very direct, technique [106].

For the Pt surface, the presence of a non-linear term in the growth law

appears to be crucial to the appearance of oscillations in many catalytic processes, e.g., CO oxidation with NO [107, 108], CO oxidation with O_2 [109, 110] and NO reduction with H_2 [85, 111]. Under reaction conditions, the catalyst surfaces undergo transformation; these are non-equilibrium processes. Moreover the reaction rate may not remain constant but changes periodically or exhibits chaotic behavior. There can also be the formation of spatial patterns on the catalyst surface [112], and these have been modelled recently within a sophisticated reaction-diffusion scheme [113]. Although we are not aware of any literature concerning oscillatory reactions on Ir{100}, the experimental findings by Ali *et al.* suggest that such oscillatory behavior may be present at temperatures above 900 K.

Mechanism: What is the underlying mechanism that is responsible for the non-linear growth law? Hopkinson *et al.* [92] and Ali *et al.* [96] have proposed a simple mechanism for the restructuring process which involves a cooperative phenomenon among CO molecules: due to statistical fluctuations of the local CO coverage on the hex phase, 4-5 CO molecules come together at the boundary of the growing (1×1) domain, or at a step, and convert 8-10 Pt atoms from a hex to square arrangement; however it is not clear *why* 4-5 CO molecules are needed or precisely *how* they cooperate. One explanation for the 'magic' value has been suggested by Passerone *et al.*, [114] who performed MD simulations on Au{100}, and found that when islands/craters are formed by adsorbing/desorbing Au atoms, they do not remain stable unless they exceed a critical size of 8-10 Au atoms. However, it is not clear that this number will translate to Pt or Ir surfaces, especially in the presence of CO. The restructuring of Pt{100} has also been studied in more recent MD simulations by van Beurden and coworkers [95], who have found that the CO molecules initiate surface relaxations and lead to a shear tension between adjacent $[0\bar{1}1]$ rows due to the preference for a square rather than a hexagonal coordination sphere, and the restructuring proceeds through the ejection of chains of Pt

atoms, and a rearrangement of the remaining surface atoms. Their simulations showed no evidence of a cooperative phenomenon between 4-5 CO molecules, and the source of the non-linear growth law remains a mystery. However, it is important to note that their MD simulations were done at much higher CO coverages (0.4-0.5 ML) than the critical coverage at which the experiments showing the fourth-order power law dependence of the rate of (1×1) formation were conducted. The mechanism for the lifting of the reconstruction is may not be the same for low and high CO coverage. At low coverage, lifting of the reconstruction occurs when random statistical fluctuations bring about a sufficiently high local coverage to instigate nucleation of (1×1) islands; at the high total coverages studied in the MD simulations, such high local coverage would be found across the whole surface at all times. The experimentally observed power law dependence may stem from the probability of bringing together 4-5 CO molecules within a sufficiently small area at low overall coverage.

5.3 Details of calculations

It is known that the lifting of the reconstruction in the systems under study is governed by very small differences in the energies of the competing structures; it is therefore vital to do as accurate a calculation as possible. For this reason, we have chosen to perform *ab initio* calculations within the framework of DFT, since this is perhaps the most reliable method currently available for obtaining accurate values of ground state properties such as structures, surface energies and adsorption energies.

Our calculations have been performed using the CASTEP package. We have used a plane wave basis set cut-off of 25 Ry (340) eV, and ultrasoft pseudopotentials. The pseudopotentials for Ir, C and O are Ir_OO.usp, C_OO.usp

and O_OO.usp respectively which are provided along with the CASTEP distribution (Version 4.2). We have used the Perdew-Wang form of the generalized gradient approximation (GGA), [13] which is known to predict correctly the reconstruction energy of Ir{100} and the preferred sites for CO adsorption on both the reconstructed and the unreconstructed surfaces.

In order to test the reliability of the pseudopotentials used in our calculations, we first performed calculations on bulk Ir and a CO molecule in the gas phase. For the former we obtain a lattice constant of 3.86 Å which is in excellent agreement with the experimental value of 3.84 Å, while for the latter, we obtained a C-O bond length of 1.14 Å which also agrees very well with the experimental value of 1.13 Å [116].

For surface calculations, we use a supercell consisting of a slab of six layers of Ir atoms separated by a vacuum thickness of about 10 Å. The top four Ir layers are allowed to relax their positions, whereas the bottom two are fixed at the bulk separation ('asymmetric' slab). Since the slabs are asymmetric but periodic, there could be a residual dipole field in the cell that interacts with the adsorbates. To check whether this contribution is important we also calculate the CO adsorption energy on an unreconstructed symmetric slab having a CO coverage of 0.5 ML. We find that the adsorption energies obtained from the two slab calculations differ by 0.007 eV. Thus, we find that the error introduced by the use of an asymmetric slab corresponds to a negligible error of 0.3%. Therefore, all our subsequent calculations were carried out using asymmetric slabs. Further, only the top surface is allowed to reconstruct; note that the density of atoms is different on a reconstructed and unreconstructed surface. Thus, all such asymmetric slabs will contain one surface that is of interest to us, while the other side consists of a bulk-truncated (unrelaxed and unreconstructed) Ir{100} surface. In order to determine the surface energy of the latter, we also perform a calulation on a 'symmetric' slab, comprised of

eight layers, of which the middle two are fixed at the bulk spacing, while the top three and bottom three layers are allowed to relax. A comparison of the symmetric and asymmetric slabs for the unreconstructed structure enables one to determine separately the surface energies of a relaxed and bulk-truncated (1×1) surface.

The size of the surface unit cell used depends upon whether whether we are looking at an unreconstructed surface or a reconstructed one, and what CO coverage we are considering. Calculations for the clean unreconstructed surface were carried out using both (1×1) and (5×1) cells; the results obtained with the two were almost identical. For the clean reconstructed surface, we use a (5×1) cell. To study CO adsorption on the unreconstructed and reconstructed surface we adsorb CO on only one side (the side which we are allowing to relax) of the 'asymmetric slab'. For adsorption of CO on the unreconstructed surface, we consider coverages of 0.11, 0.125, 0.2, 0.25, 0.5 and 1.0 ML. The unit cells used for these calculations are shown in Fig. 5.1; note that (i) all the unit cells are square, i.e., the distance between adjacent CO molecules is the same in both directions, and (ii) the cells for different coverages are not necessarily commensurate with one another. Finally, for studying adsorption of CO on the reconstructed surface, we use a (5×2) cell, within which we consider CO coverages of 0.1, 0.2 and 0.6 ML. (Note that all CO coverages in this chapter are given with respect to the density of atoms in the topmost layer of the unreconstructed surface.)

An important consideration is the choice of k-point meshes for Brillouin zone (BZ) sampling. For the surface cells, we have used Monkhorst-Pack meshes, of the form $(n_1 \times n_2 \times 1)$, where n_1 and n_2 determine the fineness of the mesh. This issue becomes particularly crucial in the present problem, since we are interested in computing energy differences that are comparable to the errors introduced by incorrect (unconverged) BZ sampling. Such errors

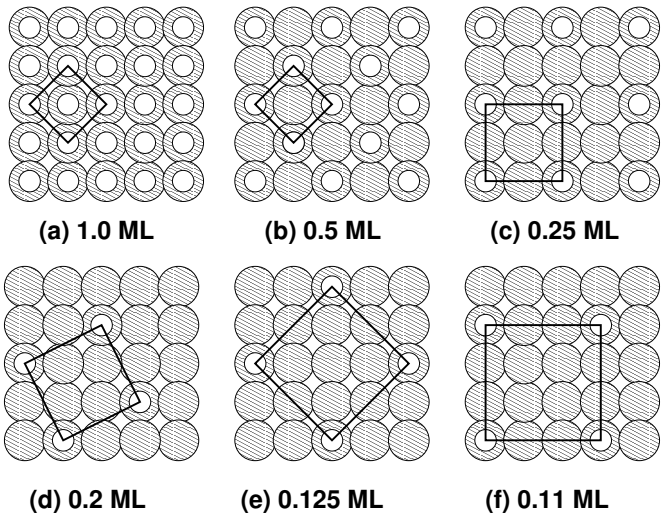

Figure 5.1: Schematic top views of the surface unit cells for different CO coverages. The large shaded circles and the small white ones denote Ir atoms on the topmost layer and CO molecules respectively. The unit cells are indicated by solid black lines: (a) and (b) $\sqrt{2} \times \sqrt{2}$ for 1.0 and 0.5 ML coverages respectively, (c) 2×2, (d)$\sqrt{5} \times \sqrt{5}$, (e) $2\sqrt{2}\times 2\sqrt{2}$ and (f) 3×3. Note that we used a bigger surface unit cell for 1.0 ML coverage in order to reduce the k-point sampling error.

can be reduced by using a k-point mesh that is as fine as possible, while keeping computational feasibility in mind. We have found that, as expected, the convergence is faster when one uses a mesh that does not include high symmetry points [the Brillouin zone center (BZC) and the k-points on the edges of the BZ]; this corresponds to choosing n_1 and n_2 to be even numbers. Examples of this are presented below in Section 5.4.3.

The specific choices made for n_1 and n_2 for the various surface cells used in the present paper are given in Table 5.1; we emphasize that convergence with respect to k-point sampling has been carefully established. Note also that computing surface energies and adsorption energies requires comparing the total energies of two systems (bulk and clean surface, or clean and covered surface); in such cases, we are careful to make sure that the unit cells and k-point meshes used for the two systems are either identical or related by folding, thereby further reducing the errors introduced by incomplete k-point

Table 5.1: Parameters for the Monkhorst-Pack k-point meshes used for different surface cells.

Surface unit cell	k-point mesh
1×1	10×10
$\sqrt{2} \times \sqrt{2}$	12×12
2×2	8×8
$\sqrt{5} \times \sqrt{5}$	8×8
$2\sqrt{2} \times 2\sqrt{2}$	6×6
3×3	6×6
5×1	2×10
5×2	2×5

sampling.

5.4 Results

5.4.1 Unreconstructed clean surface

Using the asymmetric six-layer slab described above, we find that the first interlayer distance d_{12} is contracted (with respect to the bulk interlayer separation) by 6.14%. This result compares well with that obtained from *ab initio* calculations by Ge *et al.* [90] (6.5%), but is larger than the reported experimental value ($\sim$ 3.6%). [115] Upon comparing the total energy of this asymmetric slab with that of the bulk structure, we find that the *sum* of the surface energies of the two surfaces (one relaxed and the other unrelaxed) is 3.01 eV per (1×1) area. Next, using the symmetric eight-layer slab, which possesses two relaxed surfaces, we determine the energy of the relaxed unreconstructed surface, $\Gamma_{1\times1}^{rel}$, to be 1.50 eV per (1×1) area, while the energy of the unrelaxed (bulk-truncated) unreconstructed surface, $\Gamma_{1\times1}^{unrel}$, is 1.51 eV per (1×1) area. This latter quantity is subtracted out when determining surface energies for slabs that are reconstructed and/or have CO adsorbed on only one side.

5.4.2 Reconstructed clean surface

In the reconstructed surface, the topmost layer forms a quasi-hexagonal layer on top of the square substrate, as can be seen in Fig. 5.2(a). The surface unit cell is (5×1). The reconstruction results in buckling within the layers, as well as lateral shifts of the atoms with respect to their bulk-truncated positions. The parameters used to specify these structural rearrangements are indicated in Fig. 5.2(b), and the values we obtain for them are presented in Table 5.2. It can be seen that our results are in excellent agreement with those obtained from LEED and STM by Schmidt *et al.* [86]. In accordance with their observations, we find that in addition to the reconstruction of the topmost layer, there is significant buckling in the three layers below. The two topmost layers also show lateral shifts. The only (minor) difference between our results and theirs is that our calculations yield a very small lateral shift of the third atom in the second layer (p_2^3) in a direction opposite to that determined by them.

The value we obtain for the surface energy of the reconstructed surface is $\Gamma_{5\times1}^{rel} = 1.45$ eV per (1×1) area, and we thus correctly obtain the result that the clean surface would prefer to reconstruct. Note also that the energy of reconstruction for Ir{100} is very small, viz. 0.05 eV/(1×1) area. This is in reasonably good agreement with the value of 0.07 eV/(1×1) area obtained by Ge *et al.* The slight difference between our results and theirs presumably arise from the use of slabs of different thicknesses and different k-point meshes. (Note that the energy difference here is somewhat smaller than the value of 0.21 eV/(1×1) area found experimentally for the Pt{100} surface. [99])

5.4.3 CO on unreconstructed Ir{100}

As discussed in Section 5.3 the choice of a proper k-point mesh is very crucial for our calculations. Even values of n_1 and n_2 lead to better sampling of the BZ

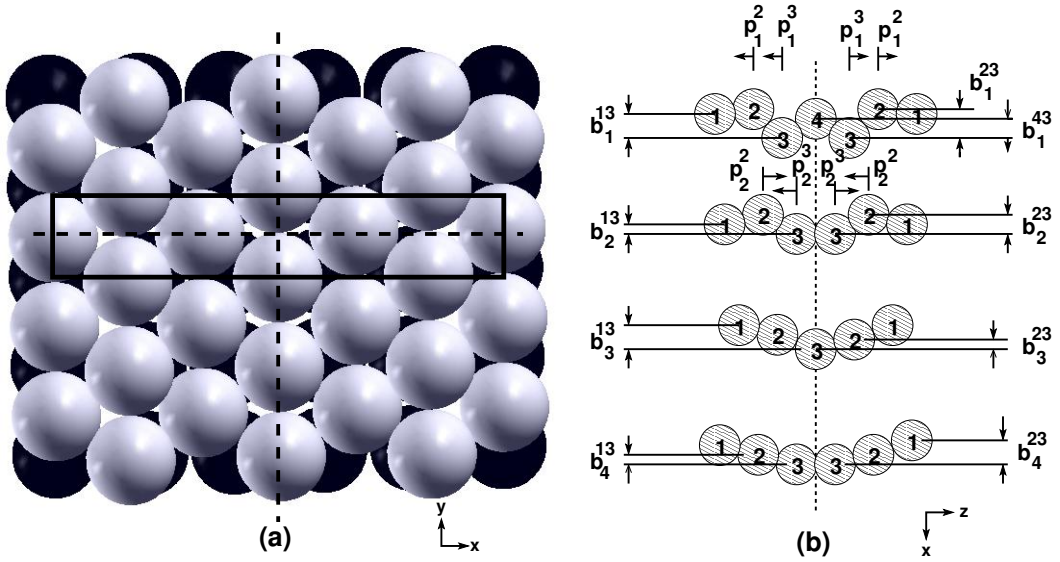

Figure 5.2: (a) Exact top view and (b) schematic side view of the reconstructed Ir{100} surface. In (a) the grey spheres are atoms in the topmost layer, whereas the black ones are atoms in the second layer. The surface unit cell is demarcated by the solid black rectangle. The horizontal and dashed lines denote the planes of reflection of the unit cell. In (b), b_n^{i3} is the distance along the z-direction between atoms i and 3 in the n^{th} layer and p denotes the lateral shift of the atoms from their bulk truncated position. The arrows denote the direction of the shift. The actual values of different parameters are listed in Table 5.2.

Table 5.2: Structure of Ir{100}-5×1 described by the parameters defined in Fig. 5.2. $\overline{d}_{ik}$'s denote average interlayer spacings between the centre of mass planes of the layers, while d_{ik}'s give the smallest spacing between their subplanes. $\overline{d}^{b}_{ik}$ describes the percent change in $\overline{d}_{ik}$ with respect to the bulk interlayer spacing (d_b). Note that our calculations are in excellent agreement with experiment, except for a slight difference in the lateral shift for the third atom in layer two (p^3_2), which we find to be negligible and in the opposite direction compared to the experimental findings.

Parameters	Our Calculations	Expt. [86]	Ge et al. [90]
d_b (Å)	1.93	1.92	1.92
d_{12} (Å)	1.96	1.94	1.97
$\overline{d}_{12}$ (Å)	2.24	2.25	-
$\overline{d}^{b}_{12}$ (%)	16.09	16.67	-
d_{23} (Å)	1.82	1.79	-
$\overline{d}_{23}$ (Å)	1.88	1.88	-
$\overline{d}^{b}_{23}$ (%)	-2.56	-2.08	-
d_{34} (Å)	1.88	1.83	-
$\overline{d}_{34}$ (Å)	1.94	1.93	-
$\overline{d}^{b}_{34}$ (%)	0.54	0.52	-
d_{45} (Å)	1.91	1.89	-
$\overline{d}_{45}$ (Å)	1.923	1.91	-
$\overline{d}^{b}_{45}$ (%)	-0.34	-1.01	-
b^{13}_1 (Å)	0.22	0.25	-
b^{23}_1 (Å)	0.53	0.55	0.47
b^{34}_1 (Å)	0.2	0.20	0.20
p^2_1 (Å)	0.03	0.05	0.05
p^3_1 (Å)	0.07	0.07	0.02
b^{13}_2 (Å)	0.04	0.07	-
b^{23}_2 (Å)	0.08	0.10	-
p^2_2 (Å)	0.01	0.01	-
p^3_2 (Å)	0.0004	-0.02	-
b^{13}_3 (Å)	0.06	0.10	-
b^{23}_3 (Å)	0.03	0.05	-
b^{13}_4 (Å)	0.04	0.06	-
b^{23}_4 (Å)	0.01	0.03	-

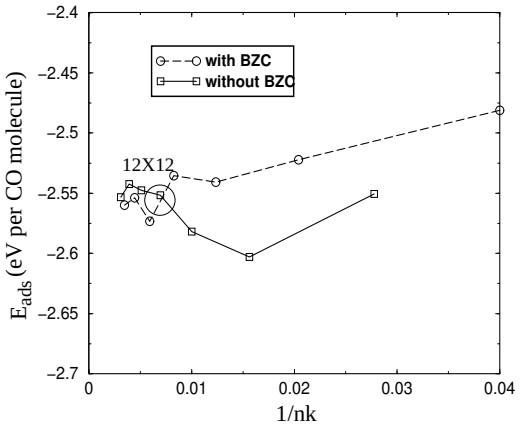

Figure 5.3: Convergence of adsorption energy (E_{ads}) of CO at 0.5 ML on the atop site of the unreconstructed surface, with respect to the k-points used for $\sqrt{2}\times\sqrt{2}$ unit cell. Monkhorst-Pack meshes of the form $(n_1 \times n_2 \times 1)$ were used, meshes that include/do not include the BZC have odd/even values of $n_1 = n_2$. For $n_1 = n_2 =$ 5, 6, 7, 8, 9, 10, 11, 12, 13, 14, 15, 16, 17, and 18 the number of points "nk" in the whole BZ is 25, 36, 49, 64, 81, 100, 121, 144, 169, 196, 225, 256, 289 and 324 respectively. Note that meshes that do not include the BZC (solid line) converge faster than those that include it (dashed line).

and quicker convergence of the adsorption energy. This fact becomes evident on inspecting Fig. 5.3, where we have shown how the adsorption energy, for CO at 0.5 ML and using a $(\sqrt{2} \times \sqrt{2})$ unit cell, converges as a function of k-point sampling. Based on this graph, we use a $(12 \times 12 \times 1)$ mesh for this particular unit cell; similar checks were performed for other coverages and cells.

Experiments and previous theoretical calculations [2] indicate that the atop site is the most probable site for CO adsorption. To verify this, and compare our results with previous DFT calculations and LEED measurements, [2] we calculate the geometry and adsorption energies of CO molecules occupying hollow, bridge and atop sites within a (2×2) surface unit cell, and at 0.5 and 0.25 ML CO coverages. The adsorption energy per CO molecule, E_{ads}, is given by:

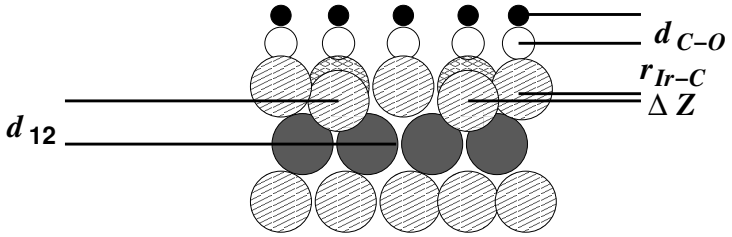

Figure 5.4: Schematic side view of the structure of CO adsorbed on unreconstructed Ir{100}-(2×2) at 0.5 ML coverage. d_{C-O} is the C-O bond length after adsorption, r_{Ir-C} gives the Ir-C bond length, d_{12} is the interlayer distance and ΔZ is the distance along the $z-$direction between two atoms of the same plane. The big, medium and small circles represent Ir, O and C atoms.

$$E_{ads} = \frac{E_{slab+CO} - E_{slab} - n_{CO}E_{CO}}{n_{CO}}, \tag{5.1}$$

where $E_{slab+CO}$, E_{slab} and E_{CO} are the the total energies of the slab with CO adsorbed on it, the clean slab, and a CO molecule in the gas phase, respectively, while n_{CO} is the number of CO molecules adsorbed per surface unit cell. The results obtained for E_{ads}, for different sites at the two coverages considered, are summarized in Table 5.3. Although there are slight numerical differences between the adsorption energies obtained from the present calculations and those of Titmuss *et al.* [2], both sets of calculations predict that CO molecules adsorb on the atop site. The difference in the numerical values of the adsorption energy obtained from the two calculations presumably arise from the use of slabs of different sizes and different k-point meshes. The structural parameters are also in good agreement with both the LEED measurements and theoretical calculations.

We go on to study the variation of the adsorption energy of CO on the atop site as a function of CO coverage. The results are summarized in the second column of Table 5.4. The difference in adsorption energy between 0.5 ML and 0.25 ML CO coverage is 0.04 eV. For lower coverage, ($\Theta \leq 0.25$ ML)

Table 5.3: Summary of our results for the c(2×2) and p(2×2) phases and comparison with experiments and previous theoretical calculations (Prev) [2]. E_{ads} denotes the adsorption energy of CO on Ir{100}; r_{Ir-C} and d_{C-O} represent the Ir-C and C-O bond lengths respectively. ΔZ gives the vertical distance between two Ir atoms in the same layer. d_{12} denotes the distance between the top two surface layers. The different parameters are also shown in Fig. 5.4.

c(2×2) phase, 0.5 ML CO coverage															
Site	E_{ads} eV/ CO molecule			r_{Ir-C} (Å)			d_{C-O} (Å)			ΔZ (Å)			d_{12} (Å)		
	Ours	Prev	Expt	Ours	Prev	Expt	Ours	Prev	Expt	Ours	Prev	Expt	Ours	Prev	Expt
Atop	-2.69	-2.65	-	1.86	1.86	1.81 ± 0.05	1.16	1.16	1.16 ± 0.05	0.14	0.19	0.13 ± 0.05	1.82	1.82	1.82 ± 0.04
Bridge	-2.51	-2.29	-	2.06	2.04	-	1.17	1.18	-	0.0	0.0	-	1.89	1.90	-
Hollow	-2.1	-1.5	-	2.29	2.28	-	1.2	1.2	-	0.0	0.0	-	1.90	1.92	-
p(2×2) phase, 0.25 ML CO coverage															
Atop	-2.83	-2.61	-	1.86	1.86	-	1.16	1.16	-	0.15	0.20	-	1.82	1.83	-
Bridge	-2.71	-	-	2.05	-	-	1.17	-	-	0.06	-	-	1.84	-	-
Hollow	-2.34	-	-	2.46	-	-	1.2	-	-	0.0	-	-	1.84	-	-

Table 5.4: Adsorption energies (E_{ads}) of CO at atop sites on unreconstructed and reconstructed Ir{100} surfaces at different CO coverages. All values of E_{ads} are expressed in units of eV/CO molecule.

CO coverage (ML)	E_{ads} unreconstructed surface	E_{ads} reconstructed surface
1.0	-1.93	-
0.6	-	-1.90
0.5	-2.55	-
0.25	-2.51	-
0.2	-2.51	-2.27
0.125	-2.52	-
0.11	-2.53	-
0.10	-	-2.31

the adsorption energy is more or less constant ($\sim$ 2.51 eV). The slight variation in the numerical values of E_{ads} may be due to numerical errors that arise because the k-point meshes used for different surface unit cells are not exactly commensurate, or may indicate the presence of very weak attractive interactions between nearest-neighbor CO molecules on the unreconstructed surface. At lower coverage, the distance between CO molecules increases, decreasing the interaction between them. At sufficiently low coverage, the CO molecules are so far apart that they do not interact with one another, resulting in a constant value of the adsorption energy. Experimental observations suggest that CO adsorption on the (1x1) phase saturates at a CO coverage of 0.5 ML. In accordance with the experimental observations our calculations yield a CO adsorption energy of 1.93 eV/CO molecule at 1.0 ML coverage, which is much less than that at other (lower) coverages.

In addition to the CO adsorption energies, we also calculate the "surface energies" (Γ_s) at different CO coverages. These "surface energies" will be used below as a measure of the stability of the reconstructed and unreconstructed surfaces. We define the Γ_s of the CO covered surface as:

$$\Gamma_s = \frac{E_{slab+CO} - n_{Ir}E_{bulk} - n_{CO}E_{CO}}{N_s} - \Gamma_s^{unrel}, \tag{5.2}$$

where N_s is the ratio of the area of the surface unit cell to that of the (1×1) cell, n_{Ir} is the number of Ir atoms and the superscript *unrel* represents the unrelaxed and unreconstructed lower surface of the slab.

5.4.4 CO on reconstructed Ir{100}

CO adsorption on the reconstructed surface has been studied for coverages of 0.1, 0.2 and 0.6 ML. In all the cases, we use a (5×2) supercell, so as to minimize the interaction between periodic images of CO molecules in adjacent supercells. Since the reconstructed surface is quasi-hexagonal in nature, there are many possible adsorption sites. The different adsorption sites which we consider for CO adsorption at 0.1 ML coverage are shown in Fig. 5.5. Our result for the adsorption energies for these different sites are given in Table 5.5. Of all the different possibilities, we find that the "atop3" site (T3) is the most probable one. While it is not surprising that CO prefers an atop site, it is somewhat unexpected that the most favoured site is atop the Ir atom that is lies lowest within the buckled surface layer, rather than the Ir atom that protrudes.

For a coverage of 0.2 ML, we have to adsorb two CO molecules in the (5×2) cell. Since CO clearly prefers to adsorb on the "atop3" (T3) sites, we choose a combination of two T3 sites. There are three inequivalent combinations of two T3 sites in the (5×2) cell, namely, A and B, A and C, and A and D (see Fig. 5.6). Our results for the CO adsorption energies at these different sites are listed in Table 5.5. Out of these three possible combination of sites, we find similar adsorption energies for the AB and AC combinations. The fact that the AD combination is disfavored suggests that CO molecules on this surface

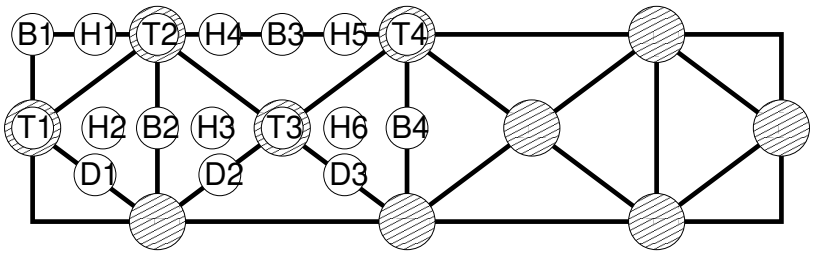

Figure 5.5: Schematic diagram showing different possible CO adsorption sites on the reconstructed Ir {100} surface (top view). Shaded circles are atoms in the topmost Ir layer. B, D, H and T denote cross bridge, diagonal bridge, hex and atop sites respectively. The sites are labelled using the same nomenclature as Deskins *et al.* [98]. Note that T1, T2, T3 and T4 correspond to sites atop the atoms labelled 1, 2, 3 and 4 in Fig. 5.2.

would prefer not to sit too close to each other. Comparing the adsorption energies for coverages of 0.1 and 0.2 ML, we find that the interaction between CO molecules on the reconstructed surface is repulsive in nature, in contrast to the *very weak* attractive interaction on the unreconstructed surface. For a coverage of 0.6 ML, we need to adsorb six CO molecules per (5×2) cell. Since the CO molecules interact repulsively on the unreconstructed surface, they will tend to spread out uniformly even at low temperatures. Hence we assume that at a coverage of 0.6 ML, CO will adsorb at every atop site, as shown in Fig. 5.6.

The variation, with coverage, of the "surface energies" of the reconstructed and unreconstructed surfaces (computed using Equation. (5.2)), is plotted in Fig. 5.7. At zero CO coverage, the reconstructed (5×1) surface is energetically more stable than the unreconstructed (1×1). However, at 0.1 ML coverage the unreconstructed surface is more stable than the reconstructed one by about 0.03 eV per (1×1) area. The crossover between the stability of the two surfaces takes place at around 0.09 ML CO coverage. Thus adsorption of CO switches the stability of the Ir{100} surfaces at a very low total coverage, that appears to be in very good agreement with the experimentally reported values

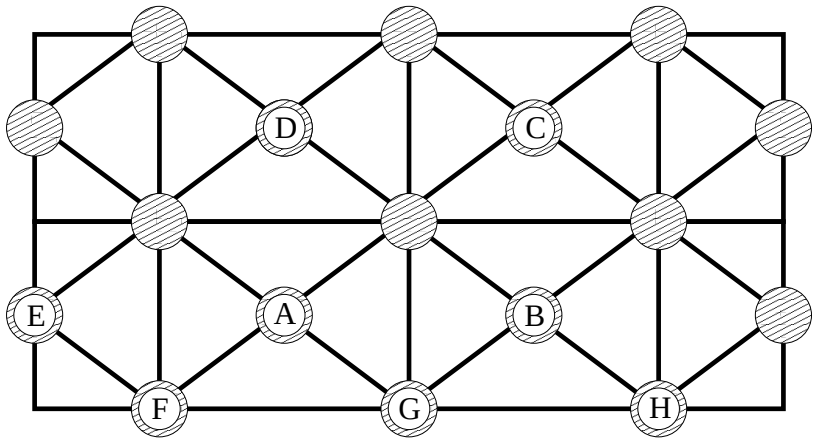

Figure 5.6: Schematic diagram showing different possible CO adsorption sites, within a (5×2) supercell, on the reconstructed Ir $\{100\}$ surface (top view) at 0.2 ML and 0.6 ML CO coverage. Shaded circles are atoms in the topmost Ir layer. For 0.2 ML coverage, possible combinations of adsorption sites are A and B, A and C, and A and D. Sites E, F, A, G, B and H are the sites for CO adsorption at 0.6 ML CO coverage. Note that the positioning of the lateral boundaries for the supercell follows the same convention as used in Fig. 5.5; i.e., E, F and A correspond to T1, T2 and T3 sites, etc.

of Hopkinson *et al.*. However, we note that this analysis has been done at conditions corresponding to zero temperature and pressure. In the next section, we extend this results to finite temperatures and pressures, by performing a thermodynamic analysis.

5.4.5 Thermodynamic analysis

In order to account for the effect of varying gas-phase temperature and pressure upon the surface configuration, we apply concepts from classical thermodynamics. The free energy (F) of a system gives a measure of the stability of the system. For a multi-species system, F is given by:

$$F = E + PV - TS - \sum_i n_i \mu_i, \tag{5.3}$$

where P, V, T and S are the pressure, volume, temperature and entropy,

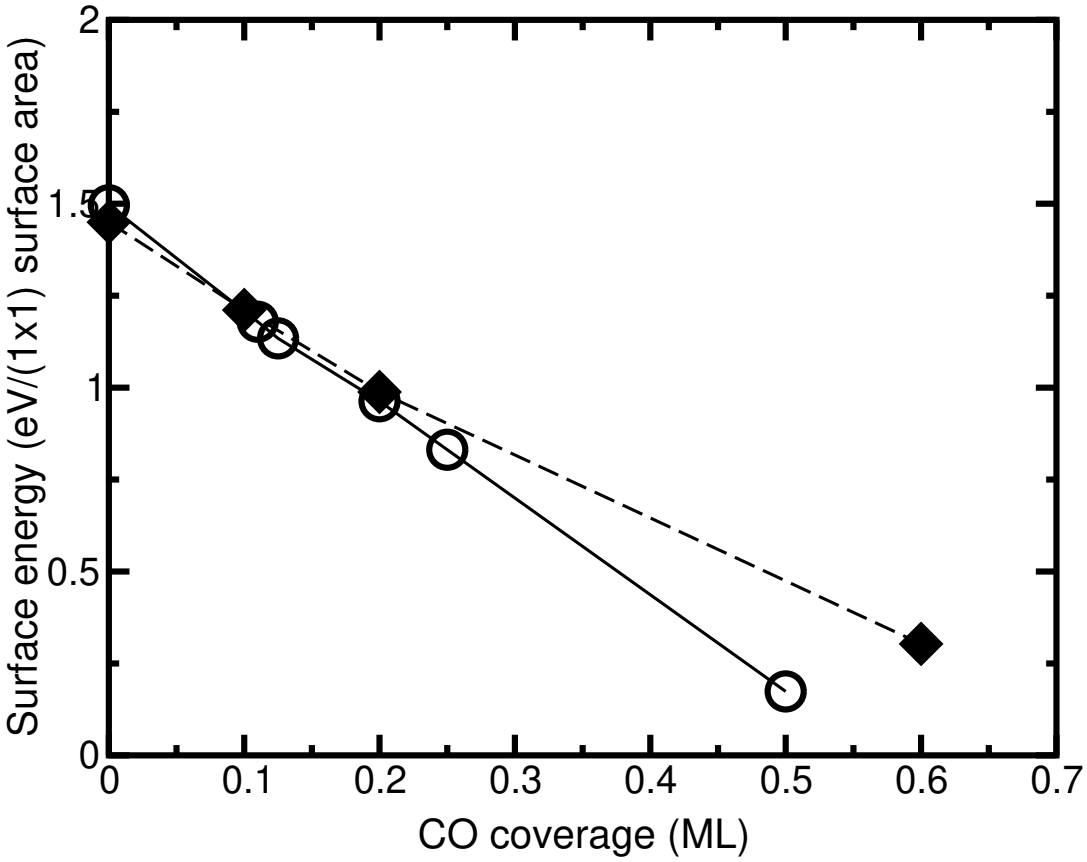

Figure 5.7: Relative stability, at $T = 0$ K, of the reconstructed and the unreconstructed surfaces as a function of CO coverage. The dashed line and the solid line denote the surface energy for the reconstructed and unreconstructed surface respectively. The two lines cross in the neighborhood of 0.09 ML.

Table 5.5: Adsorption energies (E_{ads}) at different sites of the reconstructed surface at 0.1 ML CO coverage. See Figs. 5.5 and 5.6 for the convention used in labelling sites.

coverage (ML)	site	E_{ads} (eV/ CO molecule)
0.1	T1	-2.07
	T2	-2.09
	T3	-2.31
	T4	-1.92
	H1	-1.99
	H2	-1.68
	H3	-1.70
	H4	-2.01
	H5	-2.21
	H6	-1.89
	B1	-2.00
	B2	-1.62
	B3	-2.19
	B4	-1.63
	D1	-1.76
	D2	-1.73
	D3	-2.00
0.2	A and B	-2.27
	A and C	-2.27
	A and D	-2.15
0.6	A, B, E, F, G, H	-1.90

respectively. n_i and μ_i are, respectively, the number of molecules and the chemical potential of species i at the surface. E is the internal energy of the system and is obtained from the DFT calculations.

In order to apply these concepts we need to have a clear demarcation between that which we consider to be a part of the "system" and that which we take to be its "surroundings". For our case this can be achieved in two ways:

(i) *entropy viewpoint*, in which the "system" is considered to include the

surface, the adsorbed molecules on the surface and the gas above the surface; the "surroundings" include only the world beyond some external gas container. Taking this view, the number of particles in the system is now fixed but the entropy is considerably large, since it includes large translational and rotational contributions from the gas molecules which are not adsorbed on the surface. Hence Equation (5.3) is modified as:

$$F^S = E + PV - TS. \tag{5.4}$$

From this viewpoint, the changes in the configuration of the surface are driven by massive changes in entropy between molecules on the surface and in the gas phase; net adsorption (desorption) occurs when the enthalpy of adsorption is greater (less) than this entropy difference.

(ii) *chemical potential viewpoint*, in which the "system" consists of the surface and any molecules adsorbed on the surface. The rest of the world beyond then constitute the "surroundings". Now to a fair approximation the entropy of the system is more or less negligible, since it consists only of vibrational contributions. On the other hand, the number of particles in the system is variable, so the chemical potential of the gas molecules must be included. The thermodynamic potential F now becomes:

$$F^\mu = E + PV - \sum_i n_i \mu_i. \tag{5.5}$$

The changes in surface configuration are driven by the need to maintain the equality of surface and gas-phase chemical potentials; net adsorption (desorption) occurs when the gas-phase chemical potential is instantaneously greater (less) than the surface chemical potential. Note that from both the approaches one should get the same results.

Entropy viewpoint

Taking the viewpoint that our thermodynamic system includes the surface, adsorbed molecules and the gas above it, we calculate the necessary free energy that must be minimized. This is achieved by defining free energies relative to that of the clean unreconstructed surface:

$$\delta F^S = \frac{F^S_{slab+CO} - F^S_{clean(1\times1)} - \Delta n_{Ir} F^S_{bulk} - n_{CO} F^S_{CO}}{N_s}, \tag{5.6}$$

where $F^S_{clean(1\times1)}$ and $F^S_{slab+CO}$ have been evaluated for the same unit cell, thus mitigating any systematic errors that may arise due to different k-point sampling. To evaluate the free energy of the solid phases, slab with CO molecules adsorbed on it ($F^S_{slab+CO}$) and for the clean one ($F^S_{clean(1\times1)}$) we ignore the effects of TS because typically the entropy of the solid phase is negligible compared to that of the gas phase. For the solid phases we ignore the effects of PV and approximate it for CO in the gas phase, by assuming that the gas phase obeys the ideal gas equations. With these approximations the free energy of the solid phases equals the internal energy obtained from DFT calculations. The third term in Equation (5.6) contains the free energy per atom in the Ir bulk (F^S_{bulk}) and the difference in the number of Ir atoms (Δn_{Ir}) between the DFT calculations used to obtain the first two terms. In the last term, F^S_{CO} is the free energy of the CO molecules in the gas phase. The last term accounts for the decrease in entropy of the system due to the adsorption of CO molecules from the gas phase. N_s represents the number of (1×1) cells over which the value of F^S has been calculated. By construction, therefore, δF^S for the clean reconstructed surface is the negative of the reconstruction energy, while for the clean unreconstructed surface $\delta F^S = 0$. The lowest value of δF^S under any temperature and pressure conditions indicates the most thermodynamically stable surface configuration, δF^S_{min}.

In order to evaluate F_{CO}^{S} we need to know the value of S for the gas phase at different temperatures and pressures. The values of S at a pressure of 1 bar and for a temperature range of 298.15 to 1500 K can be obtained from the CRC handbook [116]. We then derive the variation of S with pressure and temperature from the following formula:

$$S(T,P) = S(T,P^0) - R\ln(\mathrm{P}/\mathrm{P}^0). \tag{5.7}$$

P^0(=1 bar) is the reference pressure and R is the universal gas constant. In Fig. 5.8, we plot a series of lines calculated at a variety of pressures, each plotting the value of δF^S as a function of temperature. It is apparent that for all temperatures and pressures considered, there are only two possible configurations of the surface that are thermodynamically stable, the clean unreconstructed (5×1) surface and the 0.5 ML c(2×2) CO overlayer on the unreconstructed substrate. The critical temperature at which the crossover in the stability occurs varies as a function of pressure and is depicted in Fig. 5.9.

Chemical potential viewpoint

In order to evaluate the relative stability of different surface configurations from the chemical potential viewpoint, we evaluate the free energy as given by Equation (5.5). The chemical potential can be obtained by making use of its relationship to the enthalpy (H) and entropy:

$$\mu_i = \frac{1}{n_i}(H - TS). \tag{5.8}$$

The values of entropy at standard pressure can be extracted from the CRC Handbook [116]. The CRC Handbook lists only the change in H at P^0 in going from absolute zero temperature to a variety of finite temperatures ($\Delta H(0 \rightarrow T, P^0)$. Therefore $H(T,P^0)$ can be extracted using the following relation:

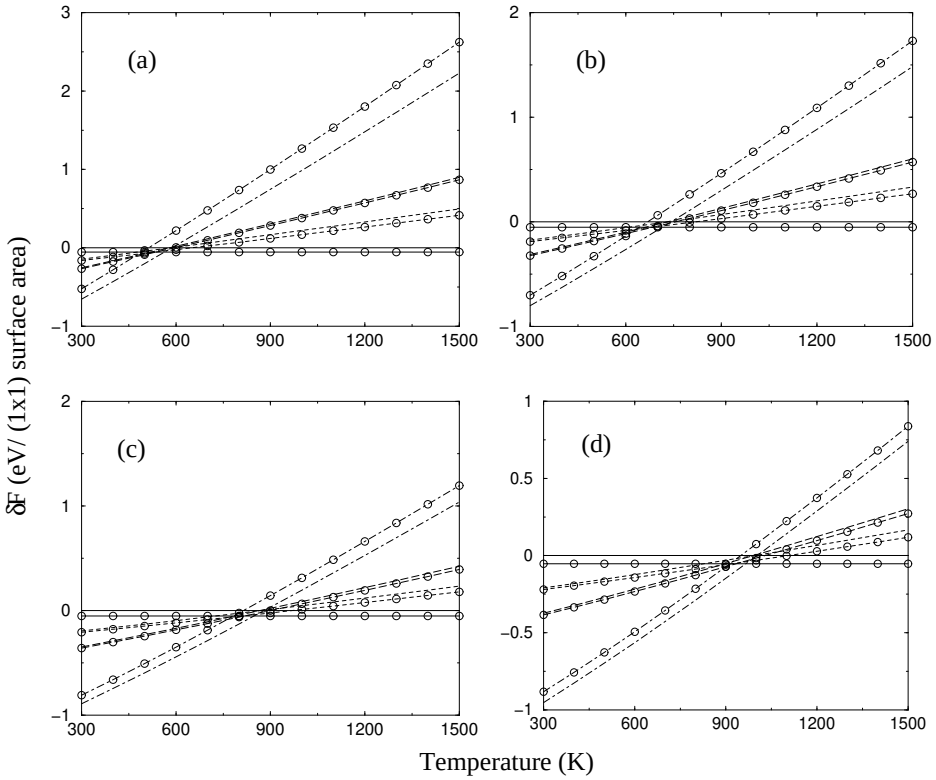

Figure 5.8: Free energies relative to that of the clean unreconstructed surface (δF) as a function of temperature at different pressures: (a) 10^{-8} mbar, (b) 10^{-3} mbar, (c) 1 mbar and (d) 10^{2} mbar. The lines without any symbols on them denote the unreconstructed surface and those with open circles denote the reconstructed one. The solid line, the short-dashed line, and the long-dashed line represent surfaces at a coverage of 0, 0.1 and 0.2 ML respectively. The dot-dashed line and dot-dashed line with open circles represent the unreconstructed surface at 0.5 ML CO coverage and the reconstructed surface at 0.6 ML CO coverage respectively. Note that we have dropped the superscripts S and μ from F since both the approaches (as described in the text) produce the same results. It can be seen that in all the cases, there are only two stable phases, viz., the dot-dashed line (0.5 ML CO on unreconstructed surface) and the solid black line with circles (clean reconstructed surface).

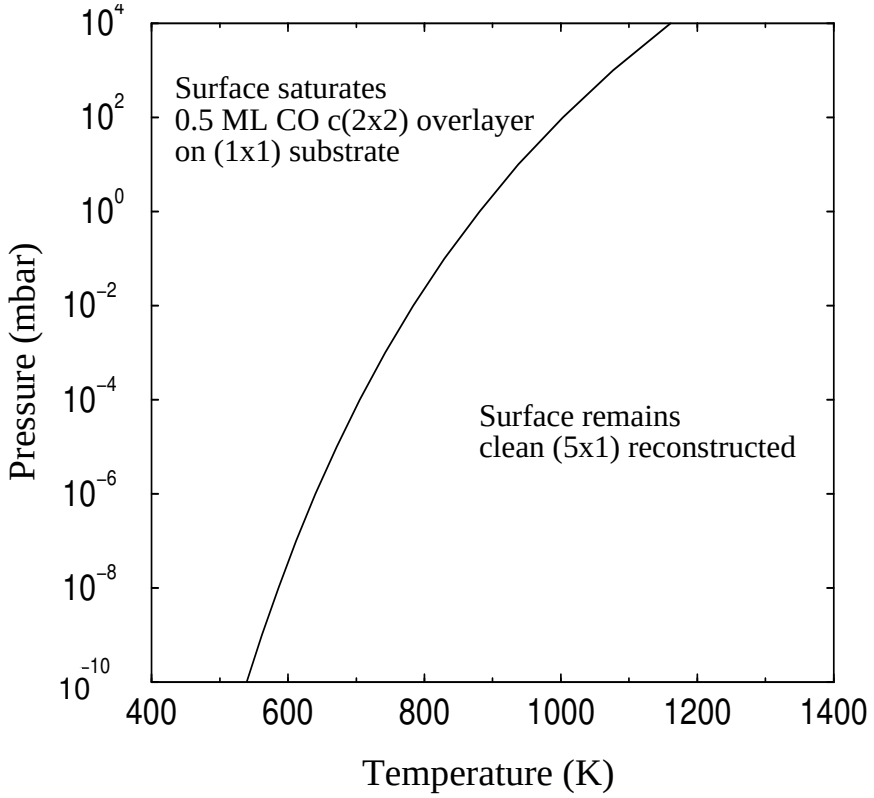

Figure 5.9: Temperature-pressure phase diagram for CO on Ir{100}. The black curve dividing the two phases gives the critical temperature at which the crossover in stability of the two phases occurs, as a function of pressure.

$$H(T, P^0) = H(0, P^0) + \Delta H(0 \rightarrow T, P^0) \tag{5.9}$$

where $H(0, P^0)$ can be obtained from DFT calculations. The variation of μ_i with pressure is computed as:

$$\mu_i(T, P) = \mu_i(T, P^0) + k_B T ln(P/P^0), \tag{5.10}$$

where k_B is the Boltzmann constant. Again we evaluate δF^{μ} the same way as in Equation (5.6) and plot the same quantities as evaluated in Section 5.4.5. The results obtained via the chemical potential approach are exactly the same as those obtained via the entropy approach, plotted in Fig. 5.8 and 5.9.

5.5 Discussion and summary

As in previous calculations, we find that Ir{100} is reconstructed; the stabilization energy being very small, viz. 0.05 eV per (1×1) area. Note that this is comparable to the errors typically introduced by incorrect k-point sampling, emphasizing the need for careful calculations. The structure of the reconstructed surface obtained by us is in excellent agreement with experiment. While the increase in density is confined to the topmost layer, the three layers below also display marked buckling and lateral shifts.

However, as more and more CO is adsorbed on the surface, there is a reversal in phase stability. Our calculations show that at zero temperature and pressure, when CO is adsorbed on Ir{100}, the relative stability of the reconstructed and unreconstructed phases is reversed at a very low total CO coverage of 0.09 ML. This shows that the lifting of the reconstruction is thermodynamically favoured at a low *local* coverage. The need for statistical fluctuations to bring 4-5 molecules together to trigger the lifting of the reconstruction must

be kinetic in origin, rather than thermodynamic.

On the unreconstructed Ir{100} surface, CO adsorbs at atop sites, and there is a *very weak* attractive interaction between CO molecules. Note that in this respect Ir{100} appears to behave differently from Pt{100}, where there is a repulsive interaction between CO molecules [101,117]. The attractive nature of the CO-CO interactions on the unreconstructed (1×1) surface suggests that at sufficiently low temperature, CO molecules would tend to cluster together on being adsorbed on the fully unreconstructed surface in order to maximize their coverage, until a saturation coverage of 0.5 ML is achieved. The weakness of the interaction, however, means that such clustering may not easily be observed in experiments performed at moderate temperature. In contrast, the interaction between CO molecules adsorbed on the reconstructed (5×1) surface is repulsive, and they tend to spread out uniformly over the surface. The difference between the two cases may be due to a change in balance between electrostatic, elastic or chemical interactions; however the effect is weak in either case. Including the cost of lifting the reconstruction, the adsorption energy of CO molecules at any total coverage to form an island of 0.5 ML local coverage on a corresponding patch of (1×1) substrate (2.45 eV per CO molecule) is still higher than the adsorption energy of CO molecules at any coverage on the unreconstructed surface. This suggests that at *any* total coverage, the molecules will prefer to cluster into islands of local 0.5 ML coverage on patches of the unreconstructed (1×1) substrate, rather than remain spread out on the reconstructed (5×1) substrate. This bolsters the interpretation of 0.5 ML *local* CO coverage on the unreconstructed (1×1) islands by Ali *et al.* even at low *total* CO coverage. The higher heat of adsorption and the attractive nature of the interaction between CO molecules on the (1×1) unreconstructed surface provide a driving force to lift the reconstruction. For both Ir{100} (where the interaction between CO molecules on the unreconstructed surface is weakly attractive) and Pt{100} (where this interaction is

weakly repulsive),the main effect is that the heat of adsorption on the unreconstructed surface far exceeds that on the reconstructed surface. As a result, the reconstruction lifting phenomenon remains similar on both Ir{100} and Pt{100}.

Our thermodynamic analysis extends the results obtained from DFT calculations to a range of pressures and temperatures. For the entire temperature and pressure range considered by us, there are only two thermodynamically stable configurations, namely 0.5 ML of CO on the unreconstructed substrate in a c(2×2) structure, and the clean reconstructed substrate. The phase diagram shows that a small change in temperature and/or pressure can result in a very large change in coverage. From experiments, we know that the lifting of the reconstruction sets in at 490 K at very low pressures (10^{-10}-10^{-07} mbar). From our phase diagram we find that at similar pressure ranges, the transition temperature lies between 550 and 600 K. Thus our results from thermodynamic analysis are reasonably consistent with experimental observations. The slight discrepancies may have arisen from our use of the ideal gas equation of state to describe the gas phase. In practical applications such as in catalytic converters in vehicles, the reactions take place at temperatures above about 750 K and at $\sim$ 10 mbar pressure. According to our phase diagram, such temperatures and pressures lie very close to the transition line. Hence slight changes in the reaction conditions may lead to drastic changes in the surface, which in turn will affect the rate of chemical reactions.

To conclude, we have investigated the thermodynamic stability of unreconstructed and reconstructed phases of the Ir{100} surface, in the presence of CO. Though our results for the critical coverage, etc., are in good agreement with experiment, it still remains intriguing to speculate about the role played by kinetic factors in the restructuring process. In particular, the origin of the nonlinear growth law observed in experiments is still a puzzle; further work on

the kinetics of the restructuring mechanism is needed to shed light on this.

Chapter 6

NO Adsorption on Rh{100}

6.1 Introduction

Catalytic reactions play an important role in many industrial and chemical processes. However, to date, catalysts are developed largely by trial and error methods. A catalyst preparation by design is highly desirable. As mentioned in Chapter 5, most catalysts are made of precious transition metals like Rh, Pt, etc. Since the reaction rate depends exponentially on the reaction barrier, the prediction of reaction barriers on catalysts is an important input to design efficient and cheap catalysts. Nevertheless, till now we do not have a clear understanding about all the factors that influence the reaction barriers, and in the last few decades there have been enormous efforts to understand them [118–120]. Both the geometry and electronic structure of the catalysts affect their reactivity. In recent years it has become evident that, in addition to the electronic properties and structure, coordination number can have a large effect on catalytic activity, with a general understanding that lower coordination number leads to higher activity [121]. In practical applications catalysts usually consist of small particles dispersed on a substrate. This introduces additional factors such as charge transfer (between catalyst and substrate) and

geometrical strain (if the catalyst adopts a structure commensurate with that of the substrate).

Perhaps the most important and widely studied catalytic reactions are the conversion of harmful exhausts of incomplete combustion of fuels in automobiles (such as CO, NO, etc.) to less harmful products (like CO_2, N_2, etc.) [124–126]. While in the previous chapter we have studied how adsorption of CO affects the structure of the surface (Ir{100}), in this chapter, we are going to study the effects of the surface structure of Rh{100} on the adsorption of NO.

The process of NO_x conversion to N_2 consists of several intermediate steps, of which NO dissociation acts as the rate-limiting-step (i.e., has the highest reaction barrier) [127–132]. Among the transition metals, the {100} surface of Rh acts as a very good catalyst in NO dissociation with a very low reaction barrier ($\sim$ 0.5 eV at 0.25 ML coverage [133]). However, efforts are still on to design better catalysts. Moreover, Rh being a very costly metal, it is desirable to replace it with something which is cheaper as well as better.

Lowering the reaction barrier implies weakening of the N-O bond. Therefore, intuitively one might expect that the stronger the metal-N bond (higher value of NO adsorption energy (E_{ads}) on the metal), the weaker is the N-O bond. Therefore it may be expected that by theoretically calculating or experimentally measuring E_{ads} on two or more different surfaces one can predict which one of them will act as a better catalyst. In this chapter we present our results on the study of the effects of coordination number, strain and magnetism on NO adsorption on the Rh{100} surface. We have studied four systems, two real and two hypothetical: (i) NO on Rh{100} at its own lattice constant, (ii) NO on Rh{100} strained to MgO lattice constant, (iii) NO on 1 ML Rh/MgO{100} at MgO lattice constant and (iv) NO on 1 ML Rh/MgO{100} at Rh lattice constant.

6.2 Previous work

6.2.1 Clean Rh{100} surface

Rh{100} surfaces are interesting not only from an application point of view but also from a fundamental physics point of view. There are significant discrepancies between first-principles calculations and low energy electron diffraction (LEED) for the relaxation of the {100} surface of Rh. LEED studies by Watson *et al.* [134] and Oed *et al.* [135] suggested that the first interlayer spacing d_{12} is relaxed with respect to the bulk spacing d_b by $+0.5 \pm 1.0\%$. Later, from their LEED studies, Begley *et al.* [136] concluded that the relaxation was $-1.16 \pm 1.6\%$. However, first-principles calculations [137–139] suggested much larger relaxations, ranging from -3.2% to -5.1%. Feibelman *et al.* [137] proposed that in experimental studies the surface may be contaminated by hydrogen which results in the observation of smaller top layer relaxations, but further careful studies by Begley *et al.* [136] and Menzel [140] appeared to rule out this possibility. On the basis of their results from *ab initio* pseudopotential based studies, Morrison *et al.* [141] suggested that Rh{100} is ferromagnetic and attributed this to be the cause for the discrepancies between the experimentally measured surface relaxations and the theoretically calculated ones. They found the surface magnetic moment to be 1.797 μ_B. A further DFT-based study by Cho *et al.* [142] suggested the Rh{100} surface to be non-magnetic. However, measurements of the linear magnetic dichroism in the angular distribution of the Rh-3*d* photoelectrons by Goldoni *et al.* [143] suggested magnetic ordering of the Rh{100} surface. Calculations of Rh overlayers on Ag and Au showed that the overlayer is magnetic [144]. Recent LDA+U calculations by Stojić *et al.* [145] predicted the Rh{100} surface to be magnetic. They observed that the density functional with local density or generalized gradient approximation (GGA) for exchange and correlation yielded a non magnetic ground

state, while the application of the GGA plus on-site Coulomb interaction U method predicted surface magnetism. They also found that the magnetic moment of the outer Rh atom increased as they increased the value of U. The maximum value of magnetic moment obtained by them is 1.24 μ_B.

6.2.2 Rh/MgO{100} surface

Since in practical applications as catalysts, Rh is supported on an MgO substrate, it is important to understand the Rh/MgO{100} interface. To the best of our knowledge there are only a few studies of these interfaces. Extended X-ray absorption fine structure spectroscopy (EXAFS) studies of highly dispersed Rh particles on MgO by Emrich *et al.* [146] suggested the Rh-O bond length to be 1.95 Å. Full potential linearized augmented-plane-wave (FLAPW) method based studies by Wu and Freeman [147] of M/MgO{100} (M =Pd, Rh and Ru) suggested that Rh and Ru monolayers on MgO were able to retain large magnetic spin moments. They also observed significant buckling in the interfacial M-MgO layer. Recent DFT-based calculations by Nobkin *et al.* [148] suggested that Rh atoms prefer to adsorb on the O atoms. They found that the adsorption energy of Rh atoms increased with an increase in their coverage, suggesting the presence of an attractive interaction between them.

6.2.3 NO on Rh{100} surface

NO adsorption and dissociation on Rh{100} surfaces have been widely studied, both experimentally and theoretically, in the last two decades. Energy loss spectroscopy (EELS) and temperature programmed desorption (TPD) experiments of Villarrubia *et al.* [149, 150] suggested that there are two adsorption states of NO on Rh{100}. At low NO coverage, they observed a peak at 114

meV, corresponding to the NO in a lying down or a highly tilted geometry. After saturation coverage has been attained, they observed another NO mode at 196 meV, which they attributed to a bridge coordinated NO. Scanning field electron emission microscope (SFEM) data of van Tol *et al.* [151] support the findings of Villarrubia *et al.*. Recent studies of NO adsorption on Rh{100}, with a combination of X-ray photoelectron spectroscopy, X-ray photoelectron diffraction near-edge X-ray absorption fine structure studies and *ab initio* calculations, at 140 K by Bondino *et al.* [122] also support the findings of Villarrubia *et al.* and van Tol *et al.*. They found that the NO peak observed at low NO coverage corresponds to a geometry in which the NO molecule is almost parallel to the surface, lying above a Rh{100} hollow site with N and O in asymmetric bridge sites. They also presented density functional based *ab initio* calculations which supported their experimental findings.

In order to understand why Rh{100} acts as a better catalyst for NO dissociation than other metal surfaces, there have been comparative studies (theoretical) on NO adsorption on different metal surfaces [152–154]. A comparative study of NO chemisorption on the {100} surfaces of Rh, Pd and Pt surfaces by Tsai *et al.* [152] suggested that on each metal, the bridge site is energetically favorable, with the atop site becoming increasingly disfavored as one proceeds from Pt→Rh→Pd. However, they were unable to explain why Rh{100} is a better catalyst than other metal surfaces. Hass *et al.* [153] performed spin-polarized (SP) calculations of NO adsorbing vertically on a bridge site on a hypothetical single monolayer and a three-layered slab of Rh, Pd, Pt and Ni to understand the magnetic consequences of NO chemisorption. They found that for the single ML and slabs of all the metals except Ni the magnetic moment is completely quenched upon NO adsorption. Even for the Ni surface, the surface magnetism is suppressed in the presence of NO. Mannstadt *et al.* studied the geometry, electronic and dynamical properties of Pd, Rh and Pt {100} surfaces with NO adsorbed on them using *ab initio*

local-density FLAPW. From their studies they concluded that the electronic properties of the three systems are similar, and therefore could not explain the reason for the observed efficiency of Rh as a catalyst. However, based on their findings of larger buckling of the Pd and Pt surface layers compared to the Rh layer, and stronger binding of NO on Pd and Pt, they speculated that the mobility and chemical reactivity of NO on Pd and Pt surfaces may be hindered. Loffreda *et al.* [183] made a DFT-based study of molecular and dissociative chemisorption of NO on Pd and Rh {100} and {111} surfaces. In an effort to design a cheaper and better catalyst than Rh they studied NO dissociation on Rh, Pd and Pd_3Mn alloy {100} surfaces [133]. They found that while the NO dissociation barrier is lowest on Rh (0.5 eV) and highest on Pd (1.6-1.8 eV), that on Pd_3Mn alloy {100} surface was intermediate (0.9-1.0 eV) suggesting that the addition of Mn to Pd strongly promotes the dissociation of NO. In order to understand the effects of coordination number on NO adsorption and dissociation there have been many studies of NO decomposition on different Rh surfaces. Wolf *et al.* [123] found that among the {100}, stepped {111} and {111} Rh surfaces, Rh{100} is the most reactive while Rh{111} is the least reactive. Loffreda *et al.* [121] performed a comparative study of NO adsorption and dissociation on the close-packed {111}, the more open {100} and the stepped {511} Rh and Pd surfaces. They found that at 300 K, the catalytic activity of the surfaces varied as Rh{100}≥terrace Rh{511}>step Rh{511}>step Pd{511}>Rh{111}>Pd{100}≥terrace Pd{511}>Pd{111}.

6.3 Computational details

The calculations presented in this chapter have been performed using the Quantum-ESPRESSO package [155] which is an implementation of DFT [40]. The Kohn-Sham equations were expanded in a plane wave basis set with a cut-off of 30 Ry. The electron-ion interactions have been approximated with

ultrasoft pseudopotentials [21]. For the augmentation charges introduced by the ultrasoft pseudopotentials, we have used a cut-off of 216 Ry. Exchange and correlation effects were treated with the Perdew-Burke-Ernzerhof form of the Generalized Gradient Approximation (GGA) [14]. For those cases where we have performed spin polarized calculations, we have used the spin polarized version of the above mentioned exchange-correlation In order to improve convergence we have used a Gaussian smearing of 0.03 Ry. For bulk Rh, Brillouin zone (BZ) integrations were done using a 12×12×12 k-point mesh.

For bulk Rh, we obtain a lattice constant of 3.86 Å which is in excellent agreement with the previously calculated value of 3.87 Å [122] and experimentally measured value of 3.80 Å [156]. Our value implies that the Rh-Rh nearest-neighbor (NN) distance is 2.73 Å in the Rh{100} surface. We determine the bulk modulus of Rh as 254 GPa which agrees well with the experimental value of 269 GPa [156]. For NO in its gas phase our calculations yield a N-O bond length of 1.14 Å which agrees well with the experimental value of 1.15 Å [157].

For MgO, we obtain a lattice constant of 4.25 Å, which is again in excellent agreement with a previous theoretical value of 4.25 Å [148] as well as the experimental value of 4.21 Å [158]. Note that this would imply that if a Rh monolayer was to be deposited commensurately with an MgO(100) substrate, the NN Rh-Rh distance within the monolayer would be increased to 3.00 Å, which corresponds to a strain of 9.89%. Of course, this also means that if the Rh/MgO{100} system were to be compressed so that the Rh-Rh distance is reduced to the value of 2.73 Å, the MgO substrate would now be strained by 9.00%

To perform calculations on the Rh{100} surface, we have used a slab of four layers of Rh atoms separated by a vacuum thickness of about 10 Å. The top two layers are allowed to relax and the bottom two are kept fixed at the

bulk separation ('asymmetric slab'). Therefore, all such asymmetric slabs will contain one surface which will be of interest to us while the other side consists of a bulk truncated (unrelaxed) Rh{100} surface. As we will show in the next section that the stretched Rh{100} surface is magnetic. Therefore one needs to worry about having introduced a spurious magnetic interaction between top and bottom surfaces of the slab. To mitigate this, is this case we have deposited a layer of H atoms on the bottom surface, which has the effect of quenching magnetization in that surface. This may introduce a spurious electric dipole. However, on performing a calculation with dipole correction we find the effect of dipoles on the NO adsorption energy to be negligible. For the stretched Rh{100} slab, we have passivated the fixed bottom layer with H atoms. In order to determine the surface energy of the relaxed surface we also perform a calculation on a 'symmetric slab' in which the middle layers are fixed at bulk separation while the top and the bottom layers are allowed to relax. For the Rh/MgO{100} systems, the slab consists of four layers of MgO and one layer of Rh and it is separated from the periodic image along the direction perpendicular to the surface by a vacuum of about 24 Å. The bottom two MgO layers were kept fixed at MgO bulk separation while the remaining two MgO layers and the Rh layer were allowed to relax.

For the clean slab we have used a (1×1) surface unit cell and a k-point mesh of 12×12×1. For calculations of NO adsorbed on the slabs, we have used a (2×3) surface unit cell and a 6×4×1 k-point mesh.

6.4 Results

As mentioned before, we have studied the NO adsorption on four systems to understand the effects of substrate and strain on NO adsorption on Rh. The relaxation of the surfaces results in contraction/expansion of the interlayer

distances. The interlayer relaxation is given by:

$$d_{ij}(\%) = \frac{d_{ij} - d_b}{d_b} \times 100, \tag{6.1}$$

where $d_{ij} = \langle z_i \rangle - \langle z_j \rangle$, $\langle z_i \rangle$ and $\langle z_j \rangle$ being the positions of the centres of mass of the i^{th} and j^{th} layers respectively and d_b is the bulk interlayer separation.

Coordination number presumably influences chemical activity because atoms that are "under-coordinated" would like to optimize the value of the ambient electron density (i.e., that due to other atoms) by forming additional bonds; note that this is the underlying idea behind effective medium [159] or embedded atom [160] theories. However, the loose definition of coordination number (the number of atoms within a certain distance) does not encapsulate this physics precisely, since a given coordination number may correspond to a range of bond lengths and thus ambient electron densities. Due to relaxations of the surface layers the in-plane bond lengths as well as the interlayer distances change resulting in a change in the ambient electron density. Therefore, in order to incorporate these effects and to look for correlations between coordination number and NO adsorption, we define an effective coordination of the i^{th} atom as:

$$N_{eff}(i) = \frac{\sum_{j \neq i} \rho^{at}_{Rh}(R_{ij})}{\rho^{at}_{Rh}(R_{bulk})}, \tag{6.2}$$

where the sum is calculated over all the neighbors j of atom i and $\rho^{at}_{Rh}(R)$ is the computed spherical charge density distribution of an isolated Rh atom at a distance R from the nucleus, R_{ij} is the distance of the j^{th} atom from the i^{th} atom, and R_{bulk} is the bulk NN interatomic distance.

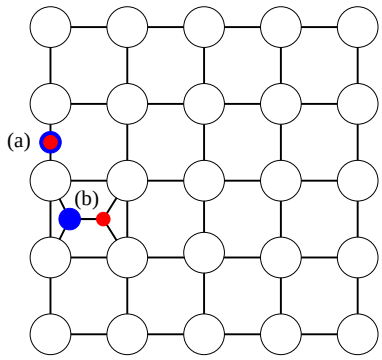

Figure 6.1: Schematic representation of the NO adsorption geometries on Rh{100}. The open circles denote Rh atoms, the red circles denote O atoms and the blue ones denote N atoms. (a) and (b) show the vertical bridge and hollow horizontal adsorption geometry respectively.

6.4.1 Case(i): Unstrained Rh{100} surface

Clean surface

For the unstrained Rh{100} surface, we obtain the value of surface energy to be 1.12 eV/surface atom which matches exactly with a previous calculation by Bondino *et al.* [122] and also agrees reasonably well with the experimental value of 1.27 eV/surface atom [161]. We find that the first interlayer spacing (d_{12}) contracts by 3.17% with respect to the bulk interlayer spacing of 1.93 Å. This is similar to the contraction of 4.0% obtained by Bondino *et al.* [122] but is larger than the experimentally reported values [134, 136, 161]. Note that there is a range in the values of d_{12} reported in the literature. We find that the second interlayer spacing (d_{23}) increases by 0.6% relative to d_b. Upon performing a SP calculation, we find that the surface is non-magnetic, which is in agreement with some previous studies [139, 142], though it disagrees with other reports in the literature [143, 145, 147]. The N_{eff} of the unstrained Rh{100} surface is 8.49.

With NO

NO adsorption on Rh{100} has been previously studied by several groups [122, 133, 183]. They have shown that over a wide range of NO coverage (from 0.125 ML – 0.5 ML), NO prefers to adsorb vertically on the bridge site. We calculate the NO adsorption energy, which is given by:

$$E_{ads} = E_{NO+slab} - E_{slab} - E_{NO}, \tag{6.3}$$

where $E_{NO+slab}$ is the total energy of the slab with NO adsorbed on it, E_{slab} is the total energy of the clean slab and E_{NO} is the total energy of the NO molecule in the gas phase. Schematic representation of the two adsorption geometries suggested by previos studies, namely, vertical bridge and hollow horizontal, are shown in Fig. 6.1. Our results for E_{ads}, and the N-O bond length (d_{N-O}) and Rh-N bond length (d_{Rh-N}) and their comparisons with previous calculations are listed in Table 6.1. In agreement with the previous calculations, we find that at 0.25 ML coverage, NO prefers to adsorb vertically on the bridge site. We obtain $E_{ads} = -2.59$ eV/NO molecule, $d_{N-O} = 1.20$ Å and $d_{Rh-N} = 1.98$ Å. Although the values of d_{N-O} and d_{Rh-N} obtained from our calculations agree well with those of the previous calculations [122, 133], we find that there are slight differences in the values of E_{ads}. Though our calculated value of E_{ads} agrees well with that of Bondino *et al.* [122] (-2.56 eV/NO molecule for vertical bridge geometry), it is slightly different from that of Loffreda *et al.* [133]
(-2.68 eV/NO molecule). These differences are presumably due to differences in computational details. Similarly, while Loffreda *et al.* found that the NO molecule adsorbing vertically on the bridge site is lower in energy than the NO molecule adsorbing horizontally in the hollow site by 0.07 eV, we find that the energy difference between the two above mentioned NO adsorption geometries

Table 6.1: E_{ads} (in eV/NO molecule), d_{N-O} (in Å) and d_{Rh-N} (in Å) for NO adsorbed on different NO adsorption sites on unstretched Rh{100} at 0.25 ML coverage and comparisons with previous calculations.

Authors	Sites					
	Vertical Bridge			Horizontal Hollow		
	E_{ads}	d_{N-O}	d_{Rh-N}	E_{ads}	d_{N-O}	d_{Rh-N}
Ours	-2.59	1.20	1.96	-2.47	1.31	1.98
Ref 122	-2.56	1.20	1.97	-2.44	1.31	1.99
Ref 133	-2.68	1.21	-	-2.61	1.33	-

is 0.12 eV.

6.4.2 Case(ii): Stretched Rh{100} surface

Clean surface

When an in-plane expansion of 9.89% is imposed on a Rh{100} slab, we find that, upon allowing interlayer distances to relax, the first two interlayer spacings d_{12} and d_{23} are reduced to 1.59 and 1.76 Å respectively. These are contracted significantly, with respect to the bulk interlayer distance in unstrained Rh{100}, by 17.31 and 8.92% respectively. The bulk interlayer spacing is also reduced by 11.3% with respect to the unstrained case and becomes equal to 1.71 Å. The net effect of having longer intralayer distances and shorter interlayer distances is a decrease in effective coordination, i.e., N_{eff} reduces from 8.49 for case (i) to 6.65. The reduction in effective coordination or increase in the in-plane Rh-Rh bond length results in making the stretched Rh{100} surface magnetic.

With NO

We determine the NO adsorption geometry on the stretched surface passivated with H. Of the two geometries we tried (vertical bridge and horizontal hollow), we find that like the unstretched surface, NO prefers to adsorb vertically on

the bridge site, with E_{ads} of -2.86 eV/NO molecule. The N-O bond length, after adsorption increases to 1.20 Å. The Rh-N bond length is 1.96 Å. The total energy of NO on the hollow site in a horizontal geometry is higher in energy than the vertical bridge one by 0.15 eV/NO molecule.

In order to determine the effects of magnetism on NO adsorption, we have performed non-spin-polarized (NSP) calculations for NO adsorption on stretched Rh{100} surface. We find that like the SP calculations, NO prefers to adsorb in a vertical bridge geometry. However, the NO adsorption energy is -3.19 eV/NO molecule, which is lower than in the SP case.

6.4.3 Case (iii): 1 ML Rh on MgO{100}, at Rh{100} lattice constant

Clean MgO slab

This is also an artificial system. We start with a four layered slab of MgO{100} which has been compressed in-plane so that it has the same in-plane lattice constant as in case (i). As a result of this compression, d_{12} and d_{23} both increase by 7.98% with respect to that in the unstrained MgO{100}. After optimization, we observe that the Mg^{2+} and O^{2-} ions move in opposite directions, resulting in rumpling of the MgO layers normal to the surface. The rumpling for MgO layers is given by:

$$d^i_{rum}(\%) = \frac{z^i_{in} - z^i_{out}}{d^{MgO}_b} \times 100, \tag{6.4}$$

where z^i_{in} and z^i_{out} are the average positions of the planes of the atoms in the i^{th} layer, moving towards (in) and away (out) from the substrate respectively and d^{MgO}_b denotes the interlayer separation of bulk MgO. The rumpling in the two topmost MgO layers is -2.04% and 0.12% respectively. However, the directions

of rumpling are different: in the topmost layer Mg^{2+} ions move towards the substrate and the O^{2-} ions move away from it, whereas the reverse is true for the second layer.

MgO slab with a ML of Rh

When a monolayer of Rh is pseudomorphically grown on the strained MgO{100} surface, we find that Rh sits on the O^{2-} ions present in the topmost layer of the surface. The binding energy of the Rh atoms is given by:

$$E^1_{bind} = \frac{E_{Rh/MgO\{100\}} - E_{MgO\{100\}} - n_{Rh}E^{gas}_{Rh}}{n_{Rh}}, \tag{6.5}$$

where $E_{Rh/MgO\{100\}}$ is the total energy of 1 ML Rh/MgO{100}, $E_{MgO\{100\}}$ is the total energy of MgO{100}, n_{Rh} is the number of Rh atoms in the unit cell and E^{gas}_{Rh} is the total energy of a single Rh atom in the gas phase. We find the binding energy of Rh atoms to be -3.59 eV/Rh atom. Alternatively, one can also define the binding referenced to a Rh monolayer:

$$E^2_{bind} = \frac{E_{Rh/MgO\{100\}} - E_{MgO\{100\}} - E_{1MLRh}}{n_{Rh}}, \tag{6.6}$$

where E_{1MLRh} is the energy of a free standing Rh monolayer. We find that E^2_{bind} is -0.23 eV/Rh atom. The vertical distance between the Rh monolayer and the topmost MgO layer is 2.40 Å. For the MgO layers, the first two interlayer separations increase by 9.38% and 8.23% respectively, with respect to the MgO bulk interlayer separation. The degree of rumpling too increases upon Rh deposition with d^1_{rum} = 4.24% and d^1_{rum} = -0.69%; note that the direction of rumpling has been reversed upon Rh deposition. We find the Rh monolayer to be magnetic with a magnetic moment of 1.55 μ_B per Rh atom.

In order to investigate whether there is any charge transfer between the

substrate and the Rh monolayer we have calculated the charge density difference, $\Delta\rho$, given by:

$$\Delta\rho = \rho_{1MLRh/MgO\{100\}} - \rho_{1MLRh} - \rho_{MgO\{100\}}, \tag{6.7}$$

where $\rho_{1MLRh/MgO\{100\}}$ is the total charge density of 1 ML Rh on MgO{100} and ρ_{1MLRh} and $\rho_{MgO\{100\}}$ are the charge densities of, respectively, an isolated monolayer of Rh, and an MgO{100} slab in the same geometry as that in 1 ML Rh/Mg{100}. Fig 6.2(a) shows isosurfaces of $\Delta\rho$. We observe that the interaction of the Rh atoms with the MgO surface induces considerable electron density redistribution in the Rh atoms and the O ions just below them. In the MgO substrate, charge redistribution is confined only to the topmost layer, suggesting that the Rh–MgO layer interactions are confined only to that layer. In order to find out the amount of charge transfer between the Rh overlayer and the substrate, we plot the charge density differences integrated over the xy-plane, as a function of z, the coordinate that runs normal to the surface, in Fig 6.3(a). Similar to Fig. 6.2 we find that the charge redistribution is confined to the Rh monolayer and the topmost MgO layer. We find that charge transfer (about 0.015 electrons per Rh atom) takes place from the O^{2-} ions to the Rh atoms. However, the magnitude of charge transfer is negligible.

NO on Rh/MgO

To determine the stable NO adsorption site on the compressed Rh monolayer supported on a MgO{100} substrate, we calculate the E_{ads} on two sites: the vertical bridge site and the horizontal hollow site. The relaxed geometries are shown in Fig 6.4. For both the adsorption geometries there is considerable buckling of the Rh monolayer and the top two MgO layers. When NO adsorbs horizontally in the hollow site, the Rh atoms are also significantly displaced in the xy-plane. NO prefers to adsorb horizontally in the hollow site (see

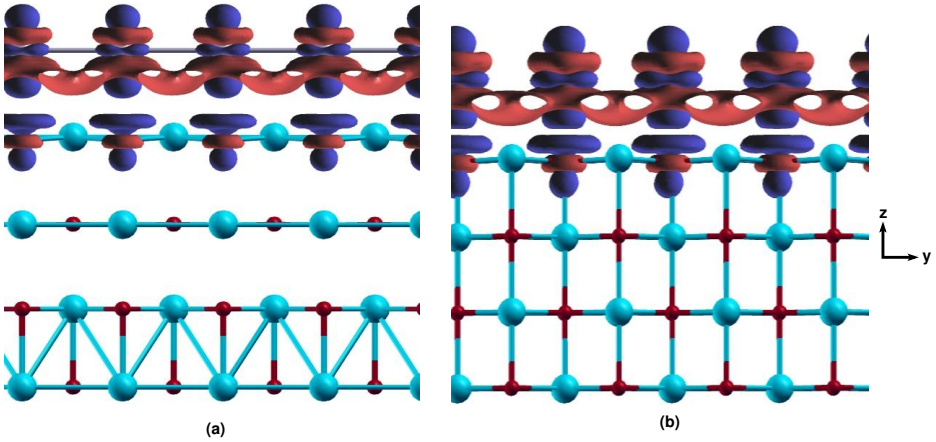

Figure 6.2: Isosurfaces of charge density differences for 1 ML Rh/MgO{100} at (a) Rh lattice constant and (b) MgO lattice constant. The charge density differences are calculated using Eqn. 6.7. Blue, grey, magenta and red balls denote Mg^{2+}, Rh, N and O^{2-} respectively. Red isosurfaces indicate an increase in charge density while blue indicate a decrease in charge density.

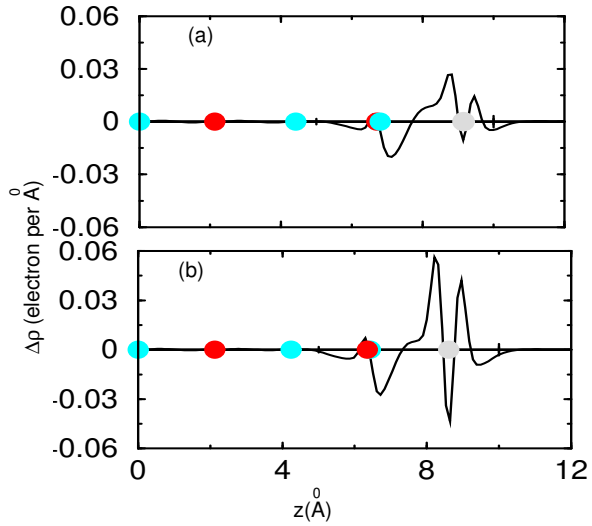

Figure 6.3: Charge density differences ($\Delta\rho$) integrated over the xy-plane, as a function of z, for a ML of Rh on MgO{100} substrate at (a) Rh{100} and (b) MgO{100} in-plane lattice constants. The cyan, red and grey circles indicate the vertical position of the Mg and O ions and the Rh atoms respectively.

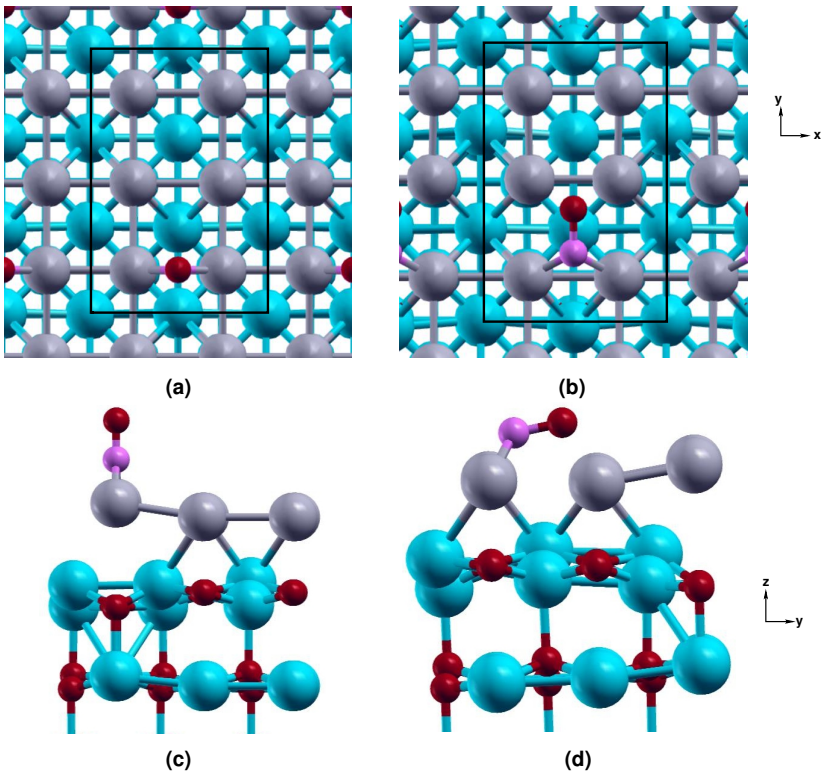

Figure 6.4: NO adsorption geometries on unstrained 1 ML Rh/MgO{100}: (i) vertical atop (top (a) and side (e) views), (ii) vertical bridge (top (b) and side (f) views), (iii) horizontal hollow (top (c) and side (g) views) and (iv) vertical hollow (top (d) and side (h) views). The surface unit cells are marked by solid lines. Blue, grey, magenta and red spheres denote Mg^{2+}, Rh, N and O^{2-} respectively.

Fig 6.4(b)) with an adsorption energy of -3.24 eV/NO molecule. However, we note that E_{ads} of NO adsorbing vertically on the bridge site (Fig 6.4(a), $E_{ads} = -3.17$ eV/NO molecule) is also very close to that for the horizontal hollow geometry. The N-O, Rh-N and Rh-O bond lengths are listed in Table 6.2. We find that for both the adsorption geometries the N-O bond length is substantially increased (d_{N-O} =1.20 and 1.32 Å for the vertical bridge and the hollow horizontal sites respectively) from the value in the gas phase (1.14 Å), suggesting weakening of the NO bond after adsorption. However, the Rh-N bond lengths are almost the same in both the geometries.

Moreover upon adsorbing NO, the magnetization of the Rh atoms is quenched.

For the preferred NO adsorption geometry, out of the six Rh atoms present in the unit cell, the spin polarization of each of the two Rh atoms to which N is attached is reduced by about 74 %, while those to which O is attached is reduced by about 45 % and the spin polarization of the two Rh atoms which are furthest from the NO is reduced by about 8.6 %.

6.4.4 Case (iv): 1 ML Rh on MgO{100}, at MgO{100} lattice constant

Clean MgO slab

For the MgO{100} surface at its natural lattice constant we observe a rumpling of -2.42% in the topmost layer (L1) and 0.33% in the layer below it (L2). Similar to case (iii), on the topmost layer Mg^{2+} ions move towards the substrate and the O^{2-} ions move away from the substrate and vice-versa for the layer below it. Unlike in case (iii), where we have observed large interlayer relaxations for the bare MgO substrate, for the present system, there is a slight expansion (0.16%) in the interlayer distance between L1 and L2 compared to d_b and the distance between L2 and L3 (third layer from surface) is almost the same as d_b. Our results, both for rumpling and relaxation of MgO{100}, agree very well with those of Alfonso *et al.* [162].

MgO slab with a ML of Rh

Upon putting a pseudomorphic layer of Rh atoms on the topmost MgO layer, we find that the Rh atoms prefer to occupy the sites atop O ions. The binding energy of each Rh atom (E^2_{bind}) is -3.27 eV/Rh atom, which is lower than that reported by Nobkin *et al.* [148] (-3.99 eV/Rh atom). We find that E^2_{bind} is -0.67 eV/Rh atom. We find the Rh-O distance to be 2.25 Å, which is larger than the value of 2.10 Å reported in Ref. 148. In comparison with the clean MgO{100}

slab, there is substantial rumpling of L1 (4.04%) and a slight rumpling of L2 (-0.96%). The direction of rumpling is reversed with respect to the MgO{100} slab. Although the direction of displacements of Mg^{2+} and O^{2-} obtained from our calculations are the same as that of Nobkin *et al.*, their value of rumpling is slightly more than ours. The main reason for the differences The differences in the numerical values of Rh binding energy on MgO, Rh-O distance and rumpling of the MgO layer obtained from our calculations and those of Nobkin *et al.* is presumably due to the differences in the details of the calculations. The main difference between their calculations and ours is that while they have performed a NSP calculations, we have done a SP one. In addition to that, while Nobkin *et al.* used a 6×6×1 k-point mesh, smearing width of 0.1 eV and relaxed along z-direction only, we have used a 6×4×1 k-point mesh, smearing width of 0.41 eV and relaxed along all the three directions. The expansion of the interplanar distance between L1 and L2, upon putting Rh on MgO{100}, increases to 1.55% with respect to the MgO bulk interplanar distance. Consistent with the findings of Wu *et al.* [147], we find the monolayer of Rh to be magnetic. However, Wu *et al.* found the magnetic moment to be 1.21 μ_B/atom, which is slightly less than the value of 1.50 μ_B/atom obtained by us.

Similar to case (iii), we observe charge redistribution due to the interaction of the Rh monolayer with the MgO substrate (see Fig 6.2(b)). The charge redistribution is not uniform. Like Nobkin *et al.* [148] we observe some charge accumulation over the Mg^{2+} ions. Fig 6.3(b) shows the charge density differences integrated over the xy-plane, as a function of z. Comparing Fig 6.3 (a) and (b), the effect of strain on charge transfer is seen to be small, with a net transfer of 0.015 electrons/Rh in case (iii) and 0.018 electrons/Rh atom in case (iv). However the slight change is in the direction expected: the Rh atoms in case (iv) have a lower effective coordination (see Eqn. 6.2) than in case (iii), and therefore would like to increase their electron density.

NO on Rh/MgO

In order to determine the preferred NO adsorption site on one monolayer of Rh on an MgO{100} substrate we tried different adsorption sites: (i) atop Rh atoms, (ii) vertical bridge site, (iii) horizontal hollow site and (iv) vertical hollow site; the relaxed geometries are shown in Fig 6.5, and the values of E_{ads}, d_{N-O} and d_{Rh-N} corresponding to the different adsorption geometries are listed in Table 6.2. We find as in case (iii), NO prefers to adsorb horizontally in the hollow site. We obtain E_{ads} = -4.08 eV/NO molecule. The values of d_{N-O} for the four adsorption geometries vary, the largest being the ones in which NO adsorbs in a vertical hollow and horizontal hollow geometry (1.34 Å), while the smallest value is when NO adsorbs in a vertical atop geometry (1.18). For the most favorable adsorption geometry (horizontal hollow) both the N-O and Rh-N bond lengths are almost the same in case (iii) and (iv). Like case (iii), upon adsorbing NO, the magnetization of the Rh atoms is quenched. Out of the six Rh atoms present in the unit cell, the spin polarization of each of the two Rh atoms to which N is attached is negligible, while those to which O is attached is reduced by about 81% and the spin polarization of the two Rh atoms which are furthest from the NO is reduced by about 28%. Similar effects of NO adsorption have been observed by Hass *et al.* [153] in their studies of NO adsorption on a hypothetical monolayer of Rh atoms Unlike ours they did the calculations for NO adsorbing in a vertical bridge geometry, kept the Rh-Rh distance at Rh bulk lattice constant and did not even relax the coordinates of NO While they found that the magnetic moments on all the atoms of the monolayer are negligible, we find that the magnetism of those Rh atoms which are attached to the NO molecule is very strongly suppressed, while in the other Rh atoms there is a slight reduction.

Table 6.2: E_{ads}, d_{N-O} and d_{Rh-N} of NO on different adsorption sites at 1/6 ML coverage on 1 ML Rh/MgO{100}. a denotes the in–plane lattice constant

System	Site and geometry	E_{ads} eV/NO molecule	d_{N-O} (Å)	d_{Rh-N} (Å)	d_{Rh-O} (Å)
a_{MgO}	vertical hollow	-3.19	1.34	2.10, 2.14	-
	vertical atop	-3.24	1.18	1.77	-
	vertical bridge	-3.87	1.21	1.94	-
	horizontal hollow	-4.08	1.34	1.94	2.17
a_{Rh}	vertical bridge	-3.17	1.20	1.93	-
	horizontal hollow	-3.24	1.32	1.96	2.24

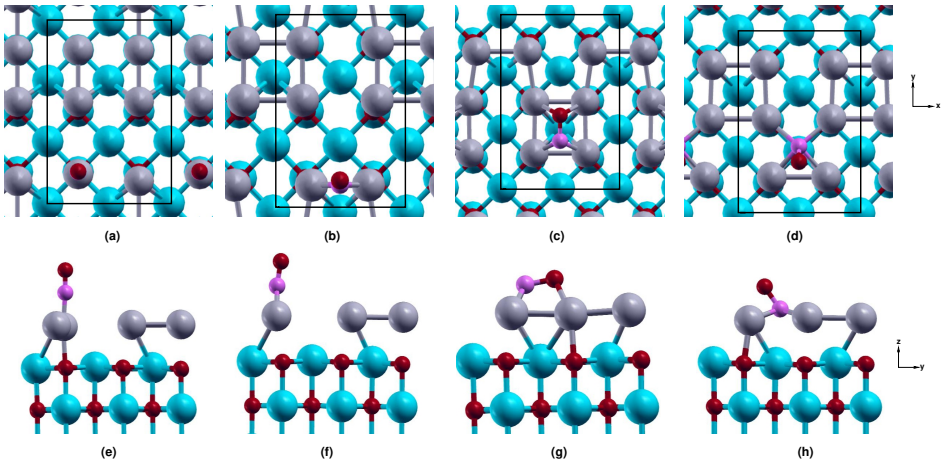

Figure 6.5: NO adsorption geometries on unstrained 1 ML Rh/MgO{100}: (i) vertical atop (top (a) and side (e) views), (ii) vertical bridge (top (b) and side (f) views), (iii) horizontal hollow (top (c) and side (g) views) and (iv) vertical hollow (top (d) and side (h) views). The surface unit cells are marked by solid lines. The color code for the atoms is the same as in Fig. 6.4.

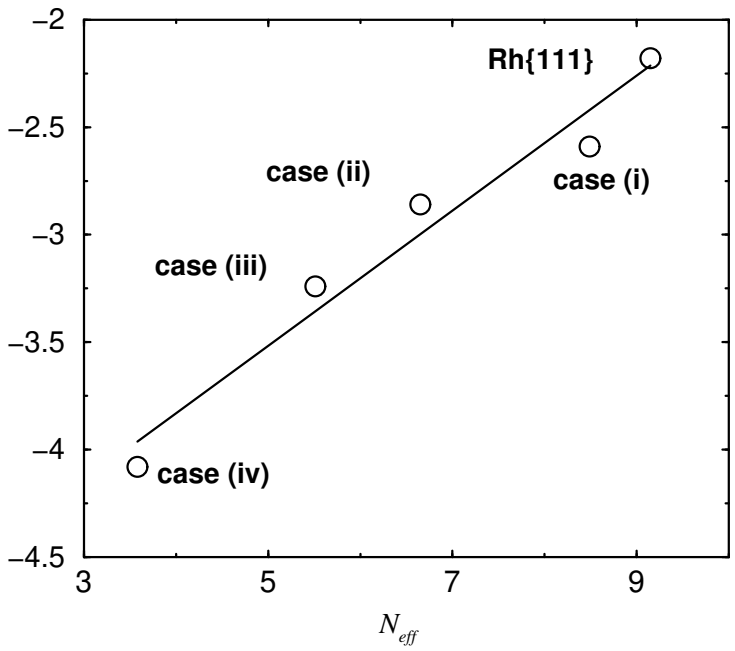

Figure 6.6: E_{ads} vs. N_{eff}. The open circles denote the calculated values and the solid line is a fit to the calculated values.

6.5 Discussion and summary

In an effort to understand the effects of (and estimate the relative importance of) coordination number, magnetism, strain, charge transfer and adsorption geometry on NO adsorption on Rh{100}, we have studied four systems: (i) unstretched Rh{100} surface, (ii) Rh{100} at MgO in–plane lattice constant, (iii) a monolayer of Rh supported on a MgO{100} substrate at Rh in–plane lattice constant, and (iv) same as (iii) but at MgO in–plane lattice constant. Of these four cases, (i) and (iv) are real while (ii) and (iii) are hypothetical. We find that while the clean unstetched Rh{100} surface (case (i)) is non-magnetic, the others (cases (ii), (iii) and (iv)) are magnetic. From a comparative study of the clean systems (i.e., without NO) in (iii) and (iv), we find that (a) the charge transfer is negligible and (b) strain does not have any significant effect on charge transfer. In cases (i) and (ii) NO prefers to adsorb vertically on the bridge site; on the Rh monolayer (both strained and unstrained) supported

on a MgO{100} slab, NO adsorbs horizontally on the hollow site. The change in adsorption geometry can be rationalized: as the effective coordination of Rh atoms is decreased, it becomes favorable for them to form more bonds to compensate for this decrease. This is achieved by moving from a vertical bridge configuration (where two Rh atoms bind to N) to the horizontal hollow geometry (where two Rh atoms bind to N and another two to O). For (ii), (iii) and (iv), the magnetism is strongly quenched upon NO adsorption.

When one moves from (i) to (iv) the E_{ads} is presumably effected by: (a) magnetization, (b) strain, (c) reduction in the number of NN Rh atoms, (d) change in adsorption geometry and (e) charge transfer. Our analysis of the results obtained for (iii) and (iv) shows that the effect of charge transfer is negligible in these systems. The effect of the rest of the factors results in an increase in E_{ads} in case (iv) by about 57% with respect to that in case (i). From (i) to (iv), through (ii) and (iii), the effective coordination number of the Rh atoms decreases because of the above mentioned factors. Accordingly E_{ads} increases, i.e., the Rh-NO molecule bond is strongest when NO adsorbs on 1 ML Rh/Mg{100} and is weakest when NO adsorbs on the unstretched Rh{100} surface. It is known that N_{eff} (see eqn. 6.2) is a reliable descriptor of local electronic structure at the atomic level [163]. Therefore a plot of E_{ads} vs. N_{eff} shows how the local environment affects E_{ads}. The E_{ads} vs. N_{eff} plot (see Fig. 6.6) shows that the NO adsorption energy increases almost linearly with effective coordination number. For the sake of comparison we have also included our results of NO adsorption on the Rh{111} surface in a hcp hollow geometry, which, according to Ref. [183], is the preferred adsorption site on Rh{111}. The almost linear increase with N_{eff} suggests that if one knows the N_{eff} of a system consisting of Rh atoms, one may be able to predict the adsorption energy of NO on that system.

In order to separate out the effects of the different factors influencing E_{ads}

and to determine the most important ones, we compare the four cases separately:

1. *Magnetization:* From the comparison of the NO adsorption energy obtained from the SP and NSP calculations in case (ii), we see that E_{ads} is more in NSP than in NSP. This is because the difference in total energy between the NSP and SP clean surface is much larger than the difference in total energies of the NSP and SP surface with NO on it, due to quenching of magnetism in the latter. Therefore the effect of magnetization is presumably a weakening of the metal-adsorbate bond.

2. *Strain*: In order to understand the effect of strain on E_{ads}, in the absence of magnetization, we compare the E_{ads} of case (i) with the NSP value of case (ii). We find that E_{ads} increases by 23% of its value in case (i), i.e., strain tends to increase the binding of NO with Rh. However, in presence of magnetization, the E_{ads} increases only by 10% [obtained from the difference in E_{ads} between case (i) and that obtained from the SP calculation in case (ii)] due to strain. Therefore the presence of magnetization weakens the effect of strain on E_{ads}.

3. *Reduction in the number of NN Rh atoms*: A comparison of the E_{ads} for (i) with that of the E_{ads} in case (iii), when NO adsorbs in a vertical bridge geometry, will enable us to understand the effect of reduction in the number of NN Rh atoms on E_{ads}. We find that the adsorption energy increases by 22%.

4. *Adsorption geometry*: We compare the adsorption energy between the vertical bridge and hollow horizontal geometry in all the cases. For all the cases, except case (iii) the E_{ads} for the one lower in energy is 5% higher than the other with respect to the E_{ads} of the low energy geometry. In case (iii) the difference is about 2%.

Therefore, combining all the above observations, we note that strain and reduction in the number of NN Rh atoms have the most dominant effects on E_{ads}. As expected both these factors lead to an enhancement in E_{ads} and hence weakening of the N-O bond. We note that there is a synergistic effect, i.e., if there is both strain and change in number of NN Rh atoms, the change in E_{ads} is about 45%. However, the presence of magnetizations tend to have an opposite effect on adsorption energy. Our calculations show that magnetization weakens the metal-adsorbate binding.

In conclusion, our studies suggest that if one aims to design a better catalyst one should look for those systems in which there are fewer NN atoms of the catalyst, the catalyst should be non-magnetic and it should be strained by being supported on a substrate.

Chapter 7

NO Adsorption on Rh Clusters

7.1 Introduction

In continuation of the study of the effects of coordination number and magnetism on reaction barriers, and with the aim of designing nanocatalysts, we have studied NO adsorption on small Rh clusters as a first step towards determining dissociation barriers.

Clusters and nanoparticles have a large surface-to-volume ratio, resulting in a large number of under-coordinated sites which facilitate chemical reactions. Moreover, the properties of clusters show a strong size dependence. The recent progress of experimental nanoscience enables one to now engineer clusters of precisely defined sizes, which possess a large number of such under-coordinated sites. For example, recently there have been several studies, both experimental and theoretical [164–167], of CO oxidation on supported Au catalysts. Although bulk Au and Au surfaces are inert, it has been observed that small clusters of Au (with $\leq$20 Au atoms) supported on magnesia act as catalysts for CO oxidation; the Au cluster with eight atoms being the smallest one to be reactive. It has also been found that the activity of these catalysts strongly depends on their size, shape, substrate, etc. Such studies have to a

new field called "nanocatalysis" [168, 169].

Although bulk Rh is non-magnetic, Rh clusters are known to be magnetic [1, 179]. Moreover as mentioned before, clusters have lots of under coordinated sites. Hence Rh clusters are good candidates to study the interplay between coordination and magnetism. In this chapter, we present the study of NO adsorption on small Rh clusters in the gas phase; the largest cluster having five Rh atoms. In the next section we provide a brief summary of the previous work on bare Rh clusters, and Rh clusters with NO adsorbed on them. In Section 7.3 we present the details of our first-principles calculations. The results for the bare clusters and with NO adsorbed on them have been presented in Sections 7.4.1 and 7.4.2 respectively. In Section 7.5 we discuss the implications of our results, and summarize.

7.2 Previous work

7.2.1 Bare clusters

Rh is one of the few non-magnetic elements whose clusters are, however, magnetic. Reddy *et al.* [170], using *ab initio* DFT, proposed for the first time that a thirteen-atom Rh cluster would be strongly magnetic due to its reduced coordination and high symmetry. To explore such possibilities, Cox *et al.* [1] carried out experimental studies on Rh clusters of sizes varying from twelve atoms to thirty two atoms. They observed that the clusters have giant magnetic moments (0.3-1.1 μ_B/atom) at 93 K. On pursuing further experimental studies on Rh clusters of different sizes [179], they found that the magnetic moments in the clusters decrease with an increase in their size. According to them, the magnetic moments of the clusters become zero when their size exceeds sixty or more Rh atoms. However, the smallest cluster studied by Cox *et al.* has nine atoms. Reddy *et al.* [173], Nayak *et al.* [172], Futschek *et al.* [174]

and Chien *et al.* [175] have determined the structure, binding energies and magnetic properties of small clusters of Rh using DFT. The binding energies (BEs) of the clusters obtained from these calculations vary over a wide range. For example, while the BE of the lowest energy spin state of Rh_2 calculated by Futschek *et al.* is 1.69 eV/atom, that obtained by Reddy *et al.* [173] is 1.88 eV/atom. However the lowest energy spin states obtained from these calculations agree with each other, except for Rh_4 and Rh_6. Calculations in Refs. 172–175 predict a singlet spin state for Rh_4, with a tetrahedral geometry as the ground state of the cluster. However, recent DFT calculations by Endou *et al.* [178] suggested that in the same geometry, Rh_4 prefers a spin septet state. For Rh_6, while some calculations predicted the singlet spin state to be lowest in energy [173], calculations done by other groups [174,175,182] suggested that the ground state had a spin multiplicity of seven. Unfortunately, to the best of our knowledge, there is no experimental data available on clusters with $n \leq 5$ other than Rh_2 [176].

7.2.2 NO adsorbed on Rh_n

Endou *et al.* [177] studied NO adsorption on a two-atom Rh cluster using DFT. They found that there is a back-donation mechanism which transfers electrons to the adsorbate resulting in the elongation of the N-O bond. Later they made a comparative study of NO adsorption on Rh, Pd, Ag, Ir, Pt and Au clusters consisting of four atoms [178]. They found that the adsorption is most favored on Ir_4.

In their Fourier transform ion cyclotron resonance studies of reactions of NO with Rh_6^+, Ford *et al.* [180] have observed biexponential kinetics, which they have interpreted in terms of structural isomerism. Recently, Anderson *et al.* [181] experimentally studied NO decomposition on small charged Rh clusters. They found that for both cationic and anionic clusters the reaction

rate increased smoothly with cluster size. However they found that cationic clusters reacted significantly faster than the anionic ones. As a support to the experimental observations of Ford *et al.*, Harding *et al.* [182] have performed DFT studies of NO adsorption and dissociation on structural and spin isomers of Rh_6^+ clusters. Their studies suggest that the biexponential kinetics observed by Ford *et al.* is indeed due to the presence of structural isomers of Rh_6^+, rather than due to different spin states. Harding *et al.* have also found that the energy barrier for NO dissociation on Rh_6^+ (0.23-0.36 eV depending on the spin state) with a geometry of the trigonal prism is much less than that observed for the same reaction on the Rh{100} surface (about 0.5 eV [133]).

7.3 Computational details

All the calculations presented in this chapter have been done using the Quantum-ESPRESSO package which is an implementation of DFT. Since Rh clusters are known to be magnetic [1, 170–174], and we are interested in studying the effects of magnetism on NO adsorption on Rh clusters, we have performed both spin-polarized and non-spin-polarized calculations. The details regarding the pseudopotential, exchange-correlation functional, the plane wave basis set cut-off and the cut-off used for augmentation charges are the same as those presented in Chapter 6, Section 6.3. The clusters are placed in a box of side 12 Å and periodic boundary conditions are used. This size of the box is large enough to ensure that the interaction between periodic images of the cluster is negligible. We have performed Brillouin zone integrations using only the Γ point. In order to hasten convergence to self consistency, we have used a very small Gaussian smearing of 0.002 Ry; note that larger values of the smearing width lead to errors in the magnetic moment of the lowest energy configuration.

In order to determine the lowest energy structure for the clusters, with

and without NO adsorbed on them, we have tried many initial geometries. In all cases, structural optimization has been performed using the Hellmann-Feynman forces [19, 20] and a BFGS-based method [45] for the minimization of energy. The structural optimization has been done without any symmetry constraints, thus permitting distortion of geometries.

For Rh_1 and Rh_2, the question of choosing initial configurations does not arise. For the bare Rh_3 cluster, we use different triangle-based geometries [equilateral (eq), isosceles (isos) and scalene] as our starting configurations. For Rh_4 and Rh_5 we have used the lowest energy structural isomers reported in the literature [172–174] as our initial configurations: the square (sq) and the tetrahedron (tet) geometry for Rh_4 and the triangular bipyramid (tbp) and the square pyramid (sqp) for Rh_5. Further, we made use of a variety of starting spin states; in a few cases we found that it was necessary to constrain the magnetization in order to find some low-lying states.

When NO adsorbs on Rh_n, the situation becomes more complex. There are a large number of inequivalent adsorption sites, as well as degrees of freedom corresponding to the orientation of the NO molecule relative to the cluster. We have considered a large number of starting configurations. In the majority of cases we found that these relaxed to different local minima of the Rh_nNO complex. The number of inequivalent possibilities that we have to consider increases rapidly as the size of the cluster grows. Therefore it is a challenging task to determine the global minimum structure.

7.4 Results

As mentioned in Section 7.1 above, our work aims to understand the effects of magnetism and coordination number on NO adsorption on small Rh clusters.

To look for correlations between coordination number and NO adsorption

we calculate the effective coordination number for each atom in the cluster using Eqn 6.2. The average coordination $\langle N_{eff} \rangle$ of the cluster is then given by:

$$\langle N_{eff} \rangle = \frac{\sum_i n_e(i)}{n}, \tag{7.1}$$

where n is the total number of atoms in the cluster and i runs over all the atoms in the cluster.

In order to understand the effects of magnetism we have performed both spin-polarized and non spin-polarized calculations. Since it is established that small Rh clusters are magnetic, the spin-polarized calculations give us information about the true ground state. Performing non spin-polarized calculations on Rh clusters is equivalent to suppressing the magnetism of the clusters, therefore enabling us to understand the effects of magnetism through a comparison between results obtained from the spin-polarized and non spin-polarized calculations. In the next two subsections, for bare clusters (Section 7.4.1) and with NO adsorbed on them (Section 7.4.2), we first present results obtained performing spin-polarized calculations followed by those obtained from non spin-polarized calculations.

7.4.1 Bare clusters

Spin-polarized (SP) calculations

Rh atom It is known, both experimentally and theoretically, that the ground state of a Rh atom corresponds to the ^{4}F ($4d^8 5s^1$) state with 5 spin up ($\uparrow$) and 3 spin down ($\downarrow$) electrons in the $4d$ orbital and one $\uparrow$ electron in the 5s orbital. Our calculations yield the same ground state. In this state the magnetic moment of the Rh atom is 3 μ_B/atom.

Table 7.1: Comparison of our results (spin-polarized) on Rh_n with previous calculation and experiments. The abbreviations for the different geometries of the bare clusters have been explained in Section 7.3. The numbers in parentheses against the bond lengths indicate the number of such bonds.

System	Author	Geometry	$\langle N_{eff} \rangle$	BE (eV/atom)	Bond length (Å)	Spin multiplicity (2S+1)
	Present	-	3.61	1.48	2.25	5
Rh_2	Ref. 172	-	-	1.51	2.26	5
	Ref 173	-	-	1.88	2.34	5
	Ref 176	-	-	1.46	2.28	5
	Present	eq	4.75	2.03	2.46	6
	Present	eq	4.67	2.00	2.41	4
	Present	isos	4.14	2.04	2.56, 2.41	6
Rh_3	Ref 172	eq	-	1.99	2.42	4
	Ref 172	isos	-	1.94	2.53, 2.40	6
	Ref 173	eq	-	2.35	2.45	4
	Ref 173	isos	-	2.37	2.52, 2.48	6
Rh_4	Present	sq	5.34	2.37	2.36	5
	Present	tet	5.04	2.42	2.53	7
	Ref 177	tet	-	3.38	2.40	7
	Ref 172	tet	-	2.41	2.49	1
	Ref 173	tet	-	2.91	2.50	1
Rh_5	Present	sqp	5.88	2.74	2.45 (sq base), 2.55	6
	Present	sqp	5.28	2.74	2.44 (sq base), 2.62	8
	Present	tbp	5.57	2.71	2.66 (×3), 2.52 (×6)	8
	Ref 173	sqp	-	3.13	2.48 (sq base), 2.63	8
	Ref 174	sqp	-	3.03		6
	Ref 173	tbp	-	3.11	2.57 (×3), 2.46 (×6)	6
	Ref 174	tbp	-	2.97		8

Rh_2 For the Rh dimer we obtain the BE of Rh as 1.48 eV/atom. We note that in the literature there is a wide variation in the values reported for the BE of Rh_2, depending on the theoretical method used (e.g., configuration interaction, DFT + local density approximation, DFT + GGA, etc). Our calculated value of BE matches excellently with the experimentally determined one (1.46 eV/atom) [176] and that obtained by Nayak *et al.* [172] using GGA. Our value for the Rh-Rh bond length of 2.25 Å is also in good agreement with those of Ref. 176 (2.28 Å) and Ref. 172 (2.26 Å). In agreement with previous calculations and experimental measurements, we obtain the preferred spin multiplicity (2S+1, S being the total spin for the cluster) for Rh_2 as 5, which corresponds to a magnetic moment of 2 μ_B/atom.

Rh_3 All the initial configurations we have tried for Rh_3, after geometry and spin optimization, yield a spin sextet magnetic state. The initial configuration in which the Rh atoms are arranged in a scalene triangle transforms upon relaxation to an isosceles triangle. The two lowest lying isomers of Rh_3, an equilateral triangle and an isosceles triangle, have binding energies of 2.03 and 2.04 eV/atom respectively. They are nearly degenerate in energy, the isosceles triangle being lower in energy than the equilateral triangle by 0.01 eV/atom. There is disagreement in the literature about whether the ground state of Rh_3 is an equilateral triangle with a quartet spin state [172], or an isosceles triangle with a sextet spin configuration [170]; the lowest energy configuration found by us is in agreement with the latter. While the next-lowest-lying isomer found by us is indeed an equilateral triangle, its spin state is sextet, not a quartet. These two lowest lying isomers are separated by 0.03 eV in energy. However for all the cases the energy differences are so small (within the error bars of typical DFT calculations) that it is hard to specify which is the true ground state for Rh_3.

Rh_4 It is the smallest cluster to have a non-planar structure. We find that both the planar structure with a square geometry and the 3D structure with a tetrahedral geometry are magnetic. Our calculations show that Rh_4 in a tetrahedral geometry with a BE of 2.42 eV/atom and in a spin septet state is lowest in energy. For the square geometry we find that the cluster has a spin multiplicity of 5 and a binding energy of 2.37 eV/atom. The ground state geometry and spin configuration of Rh_4 obtained from our calculations are in agreement with that of Endou *et al.* [178]. However, Nayak *et al.* [172], Reddy *et al.* [170] and Futschek *et al.* [174] found that the tetrahedral geometry is non magnetic and is energetically similar to that of the magnetic square geometry. To resolve this issue we calculated the total energy of Rh_4 in tetrahedral geometry with the constraint that it remains in the singlet state. In accordance with Refs. 170, 172 and 174 we find that the square and the tetrahedral geometries are energetically the same, but in contrast to their results we find that the tetrahedral geometry with a septet spin state is lower in energy than the singlet state by 0.05 eV/atom.

Rh_5 Between the two geometries which we have considered for Rh_5, namely, tbp and sqp, we find that the sqp is lower in energy than the tbp. However, the energy difference between them is very small (0.03 eV/atom). Moreover for the sqp, we find two spin isomers, one in a spin octet state and and another in a spin sextet state, both having the same values of total energy. We note that although our results are in agreement with those given in Ref. 173, Futschek *et al.* [174] find the sqp structure with a spin multiplicity of 5 to be the lowest energy structure.

From these results, one can see that even at these very small cluster sizes, there are a large number of nearly degenerate spin and structural isomers. It seems likely that several isomers will be simultaneously present upon experimentally preparing Rh clusters.

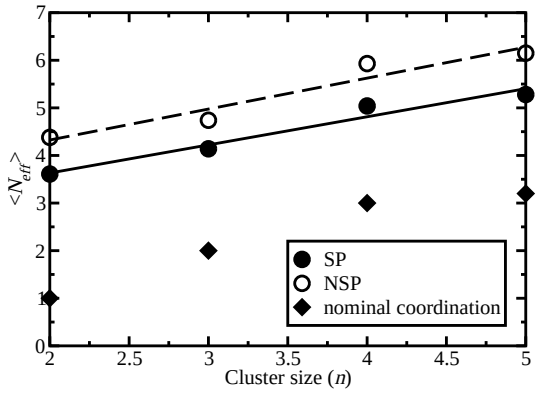

Figure 7.1: $\langle N_{eff} \rangle$ as a function of cluster size for spin-polarized and non-spin-polarized cases. The filled circles and open circles denote the $< N_{eff} >$ of the clusters for SP and NSP cases respectively. The filled diamonds show the nominal coordination in each cluster. The solid and the dashed straight lines are guides to the eye for SP and NSP respectively.

The geometry, $\langle N_{eff} \rangle$, magnetic state, BE and comparisons with previous calculations and experiments of the bare Rh_n clusters (n being the cluster size) have been summarized in Table 7.1. As mentioned previously the values of BEs of the clusters obtained from different calculations show a wide variation. The differences may arise due to differences in theory and other computational details. From our computed values of $\langle N_{eff} \rangle$ for the Rh_n clusters, $n = 2$ to 5, we find that as expected, $\langle N_{eff} \rangle$ increases with n (Fig. 7.1); note however that the values of $\langle N_{eff} \rangle$ differ from the nominal values of the coordination number; e.g., Rh_2 has now $\langle N_{eff} \rangle = 3.61$, even though each atom is bonded to only one other Rh atom.

We observe that the spin multiplicity (total magnetic moment) of the clusters increases monotonically with cluster size (see Fig. 7.2), Rh_5 with a tbp geometry has the largest magnetic moment (7 μ_B). However, the magnetic moment per atom decreases as the number of atoms in the cluster increases, which is in agreement with the expectation that clusters, being more highly coordinated, should display a decreased tendency towards magnetization.

The BE as a function of cluster size is shown in Fig. 7.3. The BE increases

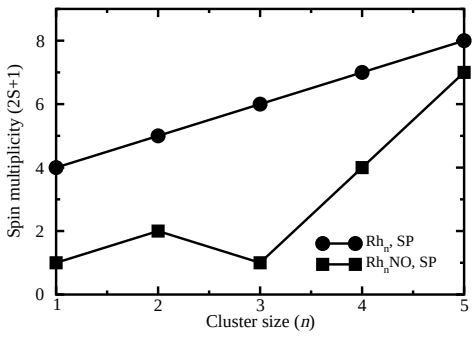

Figure 7.2: Spin multiplicities of the Rh clusters before (filled circles) and after (filled squares) NO adsorption, as a function of cluster size.

monotonically as a function of the cluster size. As n increases, $\langle N_{eff} \rangle$ increases, resulting from an increase in overlap of the electronic wavefunctions of the Rh atoms forming a cluster, thus increasing the BE. However the BEs of the clusters are far lower than that of the bulk, and therefore the clusters are more unstable than Rh bulk. The filled black circles in Fig 7.4 show that the binding energy per atom varies more-or-less smoothly also with $\langle N_{eff} \rangle$.

Non-spin-polarized (NSP) calculations

To understand the effects of magnetism on the BE and $\langle N_{eff} \rangle$ of the clusters we also performed non spin-polarized calculations on the low lying isomers of Rh_n. Table 7.2 gives the values of $\langle N_{eff} \rangle$, BE and Rh-Rh bond lengths of the clusters when non spin-polarized calculations are performed. When the clusters are constrained to be non-magnetic, their BEs are lower than that of their magnetic counterparts. For both the magnetic and the non-magnetic cases, there are several low lying isomers. However, Rh_3 is an exception. When constrained to be non-magnetic, there is only one stable geometry, the equilateral triangle. Unlike the magnetic cases where the energy differences between the isomers are small, if the clusters are constrained to be non-magnetic, there is an increase in the energy difference between the isomers.

Like the spin-polarized case, $\langle N_{eff} \rangle$ of the clusters, when constrained to

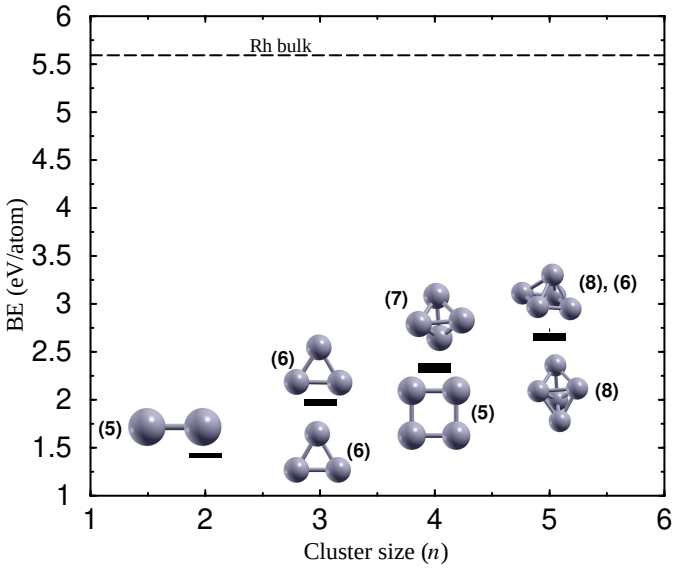

Figure 7.3: Plot of binding energy for the energetically lowest isomers (spin-polarized) vs. cluster size. The horizontal dashed line represents the binding energy per Rh in the bulk. The numbers given in parentheses alongside the structure of the clusters are their spin multiplicities.

be non-magnetic, increases with increase in cluster size (Fig. 7.1). For all the clusters Rh-Rh bond lengths are shorter compared to that of the non-magnetic case. This is because in the SP case, magnetism (which is favored by Hund's rule) is in competition with the tendency to form interatomic bonds; upon suppressing the former, the latter tendency is increased, resulting in shorter interatomic bonds and hence larger values of $\langle N_{eff} \rangle$. In this sense the effects of magnetism may therefore be expected to offset, in part, the effects of lowering coordination; we will explore this theme further below.

The open circles in Fig. 7.4 show that the BE varies monotonically with $\langle N_{eff} \rangle$ also when magnetism is suppressed; this figure makes it clear that allowing magnetism stabilizes the clusters, while decreasing their effective coordination.

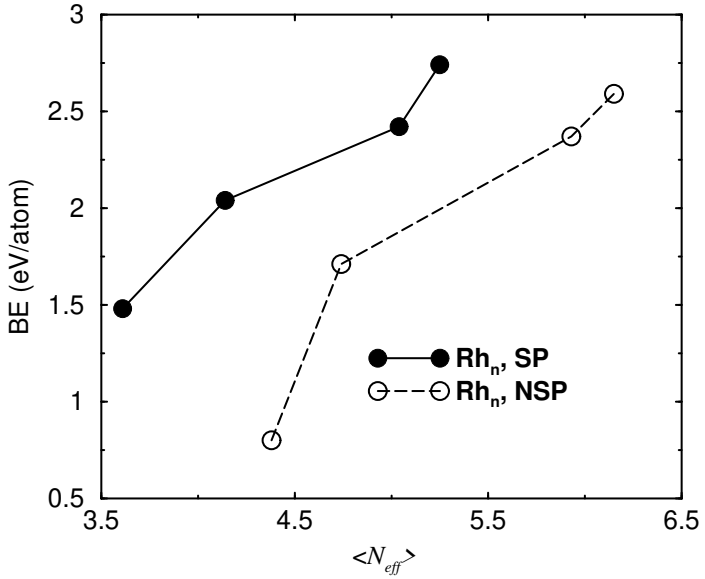

Figure 7.4: Binding energy (BE) vs. effective coordination number $\langle N_{eff} \rangle$ for the bare clusters. The filled and open circles show the BEs of Rh_n for SP and NSP respectively.

Table 7.2: Geometry, effective coordination number $\langle N_{eff} \rangle$, binding energy (BE) and Rh-Rh bond length (d_{Rh-Rh}) of Rh_n (non spin-polarized). The numbers in the parentheses indicate the number of such Rh-Rh bonds present in the clusters. The abbreviations for the different geometries of the bare clusters have been explained in Section 7.3.

System	Geometry	$\langle N_{eff} \rangle$	BE (eV/atom)	d_{Rh-Rh} (Å)
Rh_2	-	4.38	0.80	2.18
Rh_3	eq	4.74	1.71	2.36
Rh_4	sq	5.66	2.24	2.34
	tet	5.93	2.37	2.47
Rh_5	tbp	6.26	2.54	2.49 (×3), 2.53 (×6)
	sqp	6.15	2.59	2.43 (sq base), 2.54

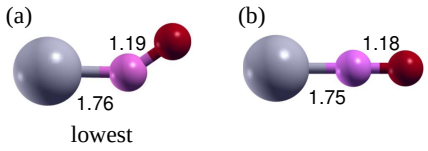

Figure 7.5: Stable NO adsorption geometries on Rh_1 after geometry optimization (for the SP case). The Rh atoms are represented by grey spheres, N atoms by magenta spheres and oxygen by red spheres. The same color convention has been followed in Figs. 7.6, 7.7, 7.8, 7.9 and 7.10. The numbers in the figures are the bond lengths in angstroms.

7.4.2 NO on Rh clusters

We determined the NO adsorption geometries and energies on Rh_n, and the spin state of the Rh_nNO. For Rh_n, the NO adsorption energy (E_{ads}) is given by:

$$E_{ads} = E_{Rh_nNO} - E_{Rh_n} - E_{NO}, \tag{7.2}$$

where E_{Rh_nNO} is the total energy of the Rh_nNO complex, E_{Rh_n} is the total energy of the bare cluster and E_{NO} is the total energy of the NO molecule in the gas phase.

Rh_1NO Out of the initial configurations which we have considered, the one in which the Rh atom was attached to the bridge site between N and O, transforms to the bent geometry [Fig. 7.5(a)]. Our calculations show that the bent geometry is lowest in energy with an NO adsorption energy of -3.23 eV/NO molecule. We note that for both the geometries (linear and bent) the Rh_1NO complex is non-magnetic.

Rh_2NO The relaxed structures of different NO adsorption geometries of the Rh_2NO complex are shown in Fig. 7.6. For the geometry shown in Fig. 7.6(d), even though the NO molecule was initially attached vertically to a Rh atom,

Table 7.3: Geometry, NO adsorption energy (E_{ads}), Rh-N bond length (d_{Rh-N}), N-O bond length (d_{N-O}) and spin multiplicity of Rh clusters with NO adsorbed on them. The lowest energy configuration for each system is given in bold text. For the sake of comparison we also present data on the Rh100 and Rh(111) surfaces.

System	geometry	E_{ads} eV/NO molecule	d_{Rh-N} (Å)	d_{N-O} (Å)	Spin multiplicity (2S+1)
RhNO	**Fig. 7.5(a)**	**-3.23**	**1.76**	**1.20**	**1**
	Fig. 7.5(b)	-3.17	1.75	1.18	1
Rh_2NO	**Fig. 7.6(a)**	**-3.10**	**1.87**	**1.21**	**2**
	Fig. 7.6(b)	-2.67	1.83	1.26	2
	Fig. 7.6(c)	2.22	-1.81	1.18	4
	Fig. 7.6(d)	-2.46	1.81	1.18	4
Rh_3NO	Fig. 7.7(a)	-2.80	1.86	1.22	3
	Fig. 7.7(b)	-2.71	1.81	1.19	5
	Fig. 7.7(c)	-2.21	1.97	1.31	3
	Fig. 7.7(d)	-2.89	1.91, 1.99	1.23	3
	Fig. 7.7(e)	**-2.90**	**1.97**	**1.23**	**1**
Rh_4NO	Fig. 7.8(a)	-2.09	1.99	1.21	6
	Fig. 7.8(b)	-1.69	2.09	1.24	4
	Fig. 7.8(c)	-2.79	1.95	1.21	6
	Fig. 7.8(d)	-3.08	1.21	1.24	6
	Fig. 7.8(e)	**-3.09**	**1.97**	**1.23**	**4**
Rh_5NO	Fig. 7.9(a)	-2.57	1.81	1.19	3
	Fig. 7.9(b)	-2.67	1.95	1.21	7
	Fig. 7.9(c)	-2.50	1.98, 2.03	1.23	7
	Fig. 7.9(d)	-2.48	2.00, 2.02	1.23	7
	Fig. 7.9(e)	-2.42	1.93	1.21	7
	Fig. 7.9(f)	-2.79	1.98, 2.03	1.23	7
	Fig. 7.9(g)	**-2.81**	**1.94**	**1.21**	**7**
Rh(100)	**vertical bridge**	**-2.59**	**1.96**	**1.20**	-
	horizontal hollow	-2.47	1.98	1.31	-
Rh(111)	**hollow hcp**	**-2.18**	**2.10**	**1.20**	-

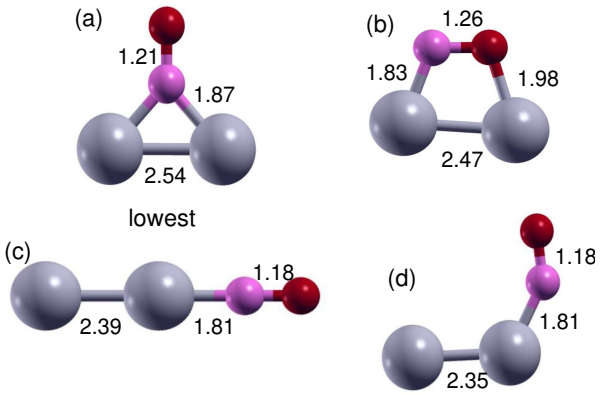

Figure 7.6: Stable NO adsorption geometries on Rh_2 after geometry optimization (SP case). The numbers in the figures are the bond lengths in angstroms. See caption to Fig. 7.5 for color code. The geometry shown in (a) is lowest in energy.

after geometry optimization it prefers a bent configuration. Out of the four configurations in Fig. 7.6, the one in which NO adsorbs vertically on the bridge site [Fig. 7.6(a)] is found to be the most stable one with an adsorption energy (E_{ads}) of -3.10 eV/NO molecule. The NO bond length increases from 1.14 Å in its gas phase to 1.21 Å in Rh_2NO.

Rh_3NO In Fig. 7.7, we have shown some of the stable adsorption geometries obtained by us for Rh_3NO. In the lowest energy configuration NO prefers to sit vertically in the hollow site [Fig 7.7(e)], with a N-O bond length of 1.23 Å. The resulting complex is non-magnetic. However, the Rh_3NO complex shown in Fig 7.7(d), in a spin triplet state, is only slightly higher in energy (by 0.01 eV) compared to the lowest energy structure.

Rh_4NO The final geometries of NO adsorption on both the square and the tetrahedral clusters are shown in Fig. 7.8. The two lowest energy isomers for the Rh_4NO complex are the configurations in which the NO adsorbs vertically at the bridge [Fig. 7.8(d)] and at the hollow site [Fig. 7.8(e)] on the cluster with tetrahedral geometry, with the former lying lower in energy than the latter by

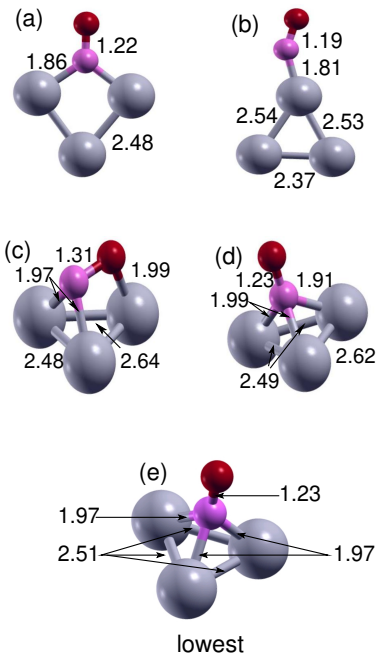

Figure 7.7: Stable NO adsorption geometries on Rh_3 after geometry optimization (SP case). The numbers in the figures are the bond lengths in angstroms. See caption to Fig. 7.5 for color code.

about 0.01 eV.

Rh_5NO For Rh_5NO, the various final geometries obtained after optimization, are shown in Fig. 7.9. Of these geometries, the one shown in Fig. 7.9(g) is the most stable one, the NO adsorption energy being -2.81 eV. We find that, in its lowest energy state, the Rh_5 cluster changes from a sqp to a tbp geometry. Among the Rh_5NO complexes in which Rh_5 remains in a sqp geometry, the one shown in Fig 7.9(b) is lowest in energy. Though these two configurations difer by 0.14 eV, it is possible that the latter configuration may be stabilized by kinetic barriers, and thus may be observed in experiments.

The filled squares in Fig. 7.2 shows the variation of spin multiplicities of the Rh_nNO complexes as a function of n. Note that for all the Rh_nNO complexes, the effect of NO adsorption is to lower the magnetization significantly. RhNO and Rh_3NO are actually found to be non-magnetic. Upon examining

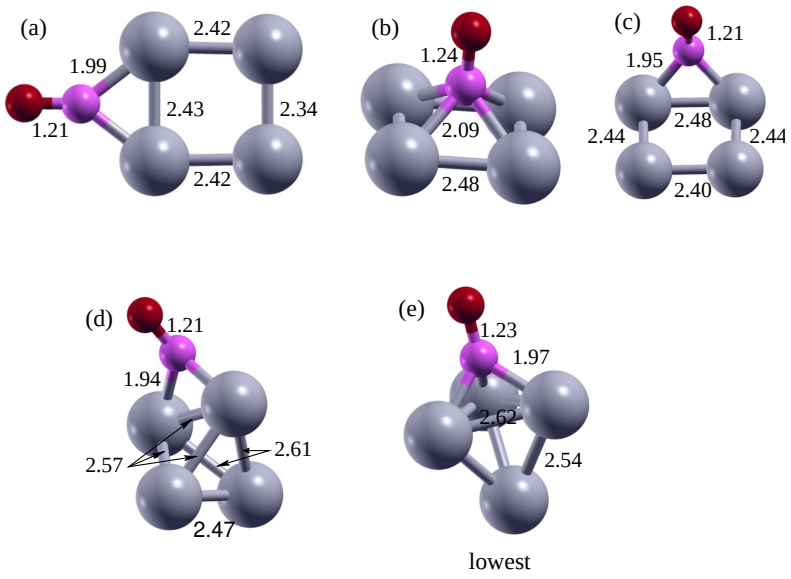

Figure 7.8: Stable NO adsorption geometries on Rh_4 after geometry optimization (SP case). The numbers in the figures are the bond lengths in angstroms. See caption to Fig. 7.5 for color code.

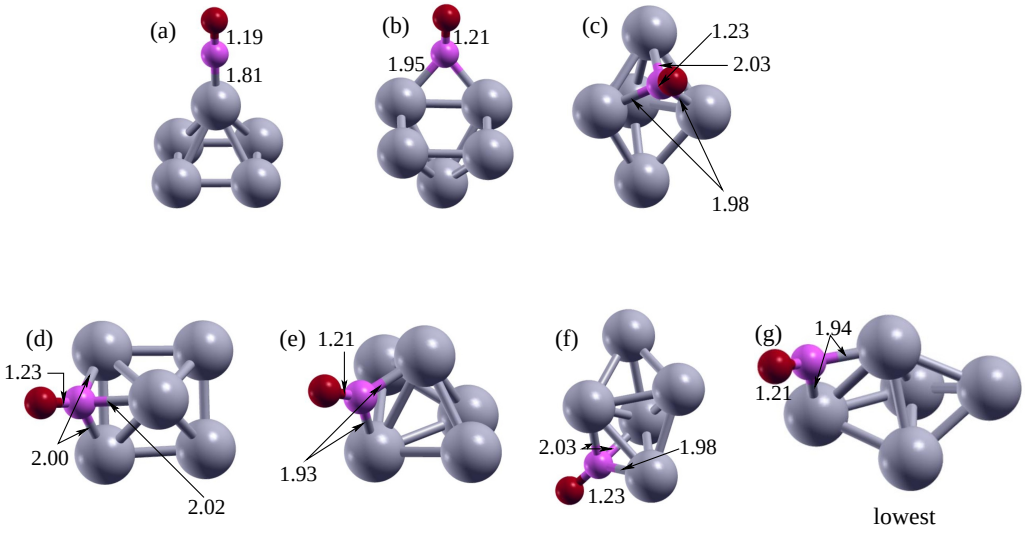

Figure 7.9: Stable NO adsorption geometries on Rh_5 after geometry optimization (SP case). The numbers in the figures are the bond lengths in angstroms. See caption to Fig. 7.5 for color code.

the spin-polarized charge densities, we find that the magnetism is quenched most strongly for the Rh atoms bonded to the NO molecule. The magnetization in the vicinity of other atoms remains either essentially unchanged or, in a few cases, actually increases. As an example, in Fig. 7.10 we have plotted the *difference* between the ↑ and ↓ densities, for (a) the lowest-energy NO-Rh_5 complex, and (b) the Rh_5 cluster, not in its equilibrium geometry but in the same structure as in (a). A visual inspection of the two figures shows that, in Fig. 7.10(a), the spin polarization is reduced significantly in the immediate neighborhood of the NO adsorption site. This becomes even clearer in Fig. 7.10(c), where we have plotted the difference between (a) and (b), i.e., the change in spin-polarized charge density as a result of NO adsorption. In this figure, red and blue indicate an increase and decrease, respectively, in the degree of spin polarization. It is very clear that the five atoms of the Rh cluster fall into three groups: (i) the two Rh atoms bonded to NO show a decrease in spin polarization (by about 34%), (ii) the next two Rh atoms show a redistribution of spin polarized charge density, with one set of d orbitals becoming more spin polarized while another set becomes less spin-polarized; the overall magnetization for these two atoms does not change significantly, (iii) the remaining Rh atom, which is furthest away from NO, exhibits an increase in spin polarization (by about 13%); this is presumably because its bonds to the other Rh atoms are weakened (as they are now bonded to NO), and it is only in this one atom that the competition between magnetism and bonding is won by the former tendency.

We have shown earlier that for the clusters, as n increases, $\langle N_{eff} \rangle$ increases. It is interesting to examine whether the adsorption energy for NO is correlated with n or/and $\langle N_{eff} \rangle$. The solid black line with open circles in Fig. 7.11 shows the variation of E_{ads} of NO on Rh_n as a function of n. We have indicated the calculated E_{ads} on Rh{111} and Rh{100} surfaces. NO prefers to adsorb vertically on the bridge site and on the hexagonal-close-packed (hcp) hollow

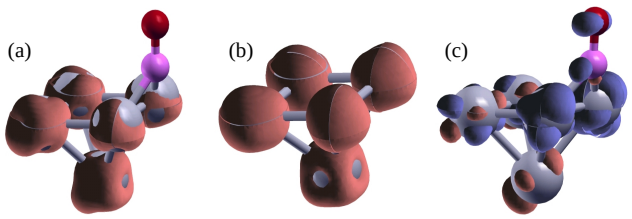

Figure 7.10: Differences between ↑ and ↓ charge densities ($\delta\rho^s$) of (a) Rh_5NO and (b) Rh_5, but in the same geometry as in Rh_5NO. The difference in $\delta\rho^s$ between (a) and (b) is shown in (c). The red isosurfaces in (c) denote an increase in magnetization and the blue isosurfaces represent a decrease in magnetization. Note the quenching of magnetism in the vicinity of NO in (a), which shows up more clearly in the blue lobes in (c).

site on Rh{100} and Rh{111} respectively. The values of $\langle N_{eff}\rangle$ for the surface atoms on Rh{100} and Rh{111} are 8.49 and 9.15 respectively. For all the clusters which we have studied, NO adsorbs more strongly on the clusters than on the surfaces. This can be explained by the fact that the $\langle N_{eff}\rangle$s of clusters are lower than those of the surfaces. However E_{ads} varies non-monotonically with cluster size. Among the clusters (with $n \geq 2$), NO prefers to bind more strongly with Rh_2 and Rh_4 than with the other clusters. The NO adsorption energy as a function of $\langle N_{eff}\rangle$ (Fig 7.12) shows similar trends as that with cluster size. However, for both the cases the variation is small.

In addition to E_{ads}, increasing (decreasing) N-O (Rh-N) bond lengths may be considered to be indications of weakening (strengthening) of the N-O (Rh-N) bonds. We have studied the variation of N-O bond lengths (d_{N-O}) and Rh-N bond lengths (d_{Rh-N}) as a function of cluster size (Fig. 7.13). For d_{N-O}, it is expected that as E_{ads} increases, d_{N-O} should increase. However our calculations show a very weak but opposite trend. We also note that with variation of E_{ads} or cluster size, the change in d_{N-O} is very small (1.20–1.23 Å). We find that d_{Rh-N} is highest for Rh_4NO, consistent with the fact that the NO adsorption energy is lowest on Rh_4. As expected d_{Rh-N} is in anti-correlation with E_{ads}, i.e., the higher the value of E_{ads}, the smaller is the value

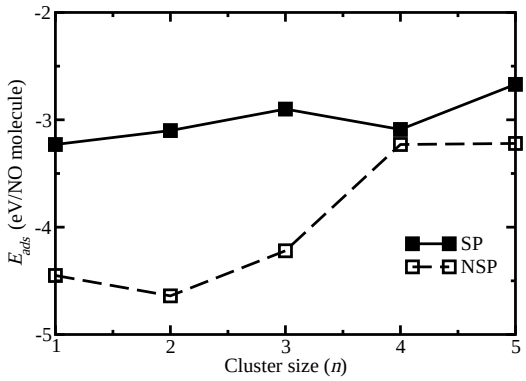

Figure 7.11: NO adsorption energy on Rh clusters, SP (filled squares) and NSP (open squares), as a function of cluster size (n).

of d_{Rh-N}.

Non-Spin-polarized calculations

To understand the effects of magnetism on NO adsorption, we have done non-spin-polarized calculations of the clusters with NO adsorbed on them. The geometry, $\langle N_{eff} \rangle$, E_{ads}, d_{Rh-N} and d_{N-O} of the Rh_n with NO adsorbed on them for the non spin-polarized case are shown in Table 7.4. For the spin-polarized case, the two geometries shown in Fig. 7.8 (d) and (e) are almost degenerate in energy. However in the absence of magnetism, the degeneracy is broken and NO prefers to adsorb vertically on a bridge site Rh_4, which is lower in energy than when NO adsorbs vertically on a hollow site, by 0.16 eV.

For all the non-spin-polarized cases, the NO adsorption energy is lower than that on the spin-polarized ones. For these cases, E_{ads} now varies monotonically with cluster size (Fig. 7.11) or $\langle N_{eff} \rangle$ (Fig. 7.12).

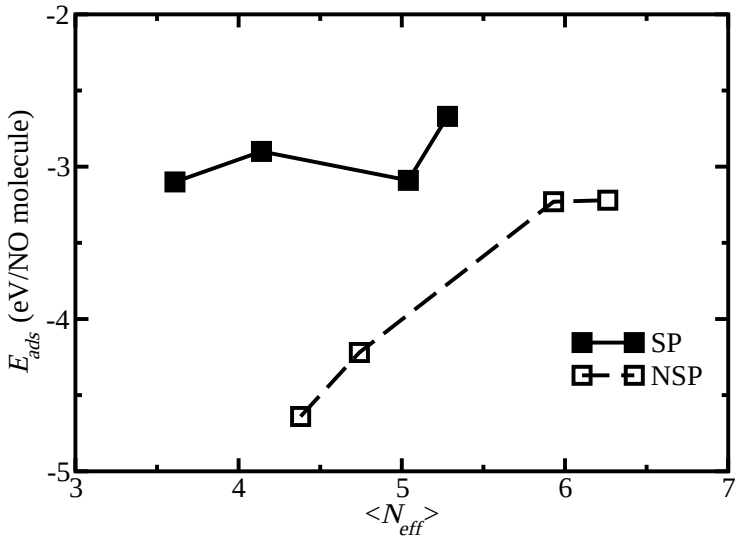

Figure 7.12: NO adsorption energy, both SP (filled squares) and NSP (open squares) as a function of $\langle N_{eff} \rangle$.

Table 7.4: Geometry, adsorption energy of NO (E_{ads}), Rh-N bond length (d_{Rh-N}) and N-O bond length (d_{N-O}) in Rh_nNO in the non-spin-polarized case. The bond topology is similar to those indicated in the second column; however, note that these figures represent the SP and not NSP case. The bond lengths do differ in the two cases.

System	geometry	E_{ads} (eV/NO molecule)	d_{Rh-N} (Å)	d_{N-O} (Å)
RhNO	∼Fig. 7.5(a)	-4.45	1.70	1.20
	∼Fig. 7.5(b)	-4.39	1.75	1.18
Rh_2NO	∼Fig. 7.6(a)	-4.64	1.87	1.21
Rh_3NO	∼Fig. 7.7(e)	-4.22	1.97	1.23
Rh_4NO	∼Fig. 7.8(d)	-3.23	1.89	1.22
	∼Fig. 7.8(e)	-3.07	1.96	1.24
Rh_5NO	∼Fig. 7.9(g)	-3.31	1.94, 1.90	1.22
	∼Fig. 7.9(b)	-3.22	1.98	1.22

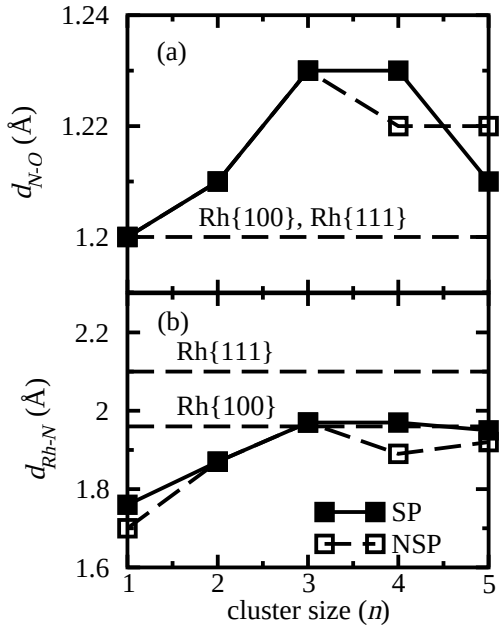

Figure 7.13: (a) N-O bond lengths (d_{N-O}) and (b) Rh-N bond lengths (d_{Rh-N}) after adsorption on Rh_n as a function of cluster size n, for SP (filled squares) and NSP (open squares). The horizontal dashed lines indicates d_{N-O} and d_{Rh-N} when NO adsorbs on the surface.

7.5 Discussion

Our finding that adsorption is weaker in the magnetic (and less effectively coordinated) case than in the non-magnetic one may seem, initally, to contradict the general expectation that lower coordination favors increased binding. However, this apparent contradiction arises from the fact that NO adsorption quenches the magnetism of the Rh clusters. This is similar to what has been observed for CO and NO adsorption on the magnetic Ni(110) surface [184–186], as well as for NO adsorption on a Rh monolayer in a hypothetical (bulk-truncated) structure [153]. However, in the last of these cases (Ref. 153) we note that the adsorption of NO completely removed the magnetization of the Rh atoms, whereas in our case this effect is only partial. For all the Rh_n and Rh_nNO cases we have examined, the lowest-energy SP solution is lower than the lowest-energy NSP solution (except for RhNO and Rh_4NO, where the two are equal in energy, as the magnetization is totally quenched upon adsorption of NO). However, the difference in total energy between the NSP and SP Rh_n clusters is much larger than the difference in the total energies of the NSP and SP Rh_nNO complexes, due to the quenching of magnetism in the latter. As a direct consequence of this, the SP adsorption energies are reduced with respect to the NSP adsorption energies. Our findings are consistent with those of Nayak *et al.* [172], who studied Rh_nH_2 clusters, and found that H_2 binds much more strongly to a non-magnetic isomer of Rh_4 than to a magnetic one.

Thus, lower coordination (which favors binding to adsorbates) also favors magnetism (which disfavors binding to adsorbates). This suggests that for Rh nanocatalysis, there may be an optimally effective cluster size, which is low enough to favor increased binding, while being high enough so that magnetism does not significantly reduce binding. The next step would be to see whether the greater binding to Rh clusters (relative to flat Rh surfaces) will also result in lower barriers for NO dissociation; work in this direction is in progress.

We note that adsorption studies such as the ones presented here could conceivably yield three possible indicators of dissociation barriers: (i) the intramolecular (N-O) bond length (ii) the metal-adsorbate (Rh-N) bond length (iii) the adsorption energy E_{ads}. One would expect that lowering of dissociation barriers might correlate with an increase in magnitude of (i) and (iii), and a decrease in (ii). Of these, it seems likely that (i) will not be a very reliable indicator, given that the N-O distance is almost the same on Rh(100) and Rh(111), even though the dissociation barriers on the two surfaces are different. Indeed, our results show almost no size-dependence for d_{N-O}, in both SP and NSP cases. We find that d_{Rh-N} decreases as n is decreased, possibly indicating a stronger Rh-N and thus weaker N-O bond. However, the values of E_{ads} do not show such a size-dependent trend for the SP case. Thus, calculations of dissociation barriers are needed to resolve the issue of whether or not the barriers will vary significantly as a function of size.

7.6 Summary

In summary, we list the main findings of our study: (i) in accordance with previous reports in the literature we find the clusters to be magnetic, (ii) the magnetic moment per atom (for the lowest energy configuration) decreases monotonically with the size of clusters, (iii) the average effective coordination number and average bond length both increase as the size of the cluster increases, (iv) on suppressing the magnetism of the clusters the bond lengths decrease and effective coordination increases, (v) E_{ads} does not display any clear trend as a function of n or $\langle N_{eff} \rangle$, in the SP case, (vi) however, E_{ads} is larger (in magnitude) for the clusters than on Rh(100) or Rh(111), (vii) the adsorption of NO strongly quenches (and, in some cases, eliminates) the magnetization of the bare clusters, (viii) this effect is local, being most prominent on the Rh atoms bonded to the adsorbate, (ix) repeating the calculations with

spin polarization suppressed leads to still higher adsorption energies.

In conclusion, our results illustrate the fact that in small clusters there can be a competition between the tendencies to bond and to magnetize, with both effects being favored by reduced coordination. This interplay between bonding and magnetism has a significant influence on the size-dependent trends in the chemical behavior of such systems.

Chapter 8

The Nature of Vibrations of a 2-D Disordered Lattice Model with Nano-scale Order

8.1 Introduction

Nano-scale structure of materials has interesting effects on their macroscopic behavior and become yet another control parameter in tuning material properties [191]. For example, relaxor ferroelectrics, such as $PbMg_{\frac{1}{3}}Nb_{\frac{2}{3}}O_3$ (PMN) [187] and $PbSc_{\frac{1}{2}}Nb_{\frac{1}{2}}O_3$ (PSN) [188], have tremendous technological potential in applications based on solid state transducers [189], due to their giant electromechanical and dielectric response. Randomness and nano-scale regions in the ordering of polar fields are known to be central to these interesting properties [192,193]. In contrast to conventional ferroelectrics such as $PbTiO_3$ with a sharp ferroelectric transition, relaxors exhibit a diffuse ferroelectric transition, with a broad peak in dielectric constant as a function of temperature.

Ferroelectricity in conventional ferroelectric materials is essentially a phonon-related property characterized by a soft mode near the ferroelectric phase transition [194, 195]. The soft phonon anomalies in the context of relaxors [196] were observed as "waterfall phonon" recently using neutron scattering, with a speculation that these are linked with nano-polar regions. Further studies of the "waterfall" phenomena based on neutron scattering were explained using a mode-coupling model [197, 198] for the coupling between acoustic and optical modes. While the work of Hlinka *et al.* [198] argued that the wave-vector k of the waterfall phonon is unlikely to be related to the size of nano-polar regions, the origin of coupling between acoustic and optical modes is not known.

A relaxor, for example PSN, PST etc., is a solid solution with a degree of disorder arising from the chemical ordering of Sc and Nb (for PSN) and Sc and Ta (for PST) at the B sites of ABO_3 perovskite lattice. Correlation between such disorder and relaxor properties of PSN and PST were shown experimentally [188, 199]. A region of the size of $\approx$ 2-6 nm [200–202] with a specific kind of chemical ordering defines a nano-ordered region (NOR) with intense local polar fields [193, 203]. Through the coupling with ferroelectric dipoles, they give rise to nano-polar regions (NPR), speculated to be linked with phonon anomalies called "waterfall phonon" in relaxors. Precise knowledge of the nature of phonons in the presence of chemically nano-ordered regions is essential to establish their possible link with the "waterfall phonon".

In this work, we determine the nature of vibrational excitations in a model system which consists of chemically-ordered nano-regions in a percolating disordered matrix. While the models used in our analysis are a great simplification of relaxors, it allows us to determine some general aspects of phonons in a nano-ordered system. Section 8.2 deals with a detailed description of the model system with two different types of interacting potential. In Section II we present the calculation details. Section III contains the results. We summarize

our results and conclude in Section IV.

8.2 Description of the model system.

For the ordered case, our model system consists of two types of atoms A and B, each having unit mass ($m_A = m_B = 1.0$) and occupying (0,0)a and $(\frac{1}{2}, \frac{1}{2})a$ sites of a square lattice respectively, a being the lattice constant. We model the interactions between two neighboring atoms with two types of potentials (U_{ij}^I and U_{ij}^{II}) to show that the results obtained from our calculations are not an artefact of the interaction potential but are the effects of the presence of nano-ordered and disordered regions. We include only harmonic interactions upto second nearest neighbors [(1,1)a]. The interactions between two atoms displaced from their mean positions by $\mathbf{u_i}$ and $\mathbf{u_j}$ are given by:

$$U_{ij}^I = \frac{1}{2}[(\kappa_r - \kappa_\theta)[(\mathbf{u_j} - \mathbf{u_i}) \cdot \hat{\mathbf{r}}_{\mathbf{ij}}]^{\mathbf{2}} + \kappa_\theta |\mathbf{u_j} - \mathbf{u_i}|^{\mathbf{2}}] \quad (8.1)$$

$$U_{ij}^{II} = k_L(\hat{\mathbf{r}}_{\mathbf{ij}}.\mathbf{u_i})(\hat{\mathbf{r}}_{\mathbf{ij}}.\mathbf{u_j}) + k_T(\hat{\mathbf{b}}_\perp.\mathbf{u_i})(\hat{\mathbf{b}}_\perp.\mathbf{u_j}), \quad (8.2)$$

where $\hat{\mathbf{r}}_{\mathbf{ij}}$ and $\hat{\mathbf{b}}_\perp$ are the unit vectors parallel and perpendicular to the line joining the i^{th} and j^{th} atoms respectively. κ_r and κ_θ are the force constants corresponding to bond stretching and bond bending for U_{ij}^I (eqn. 8.1). In eqn. (8.2) k_L and k_T are the longitudinal (parallel) and transverse (perpendicular) force constants respectively. While the model I potential has only 10 interatomic force constants, $\kappa_{r,\theta}^{AAnn}$, $\kappa_{r,\theta}^{AA2nn}$, $\kappa_{r,\theta}^{BBnn}$, $\kappa_{r,\theta}^{BB2nn}$ and $\kappa_{r,\theta}^{ABnn}$, model II has 10 distinct interatomic force constants, $k_{L,T}^{AAnn}$, $k_{L,T}^{AA2nn}$, $k_{L,T}^{BBnn}$, $k_{L,T}^{BB2nn}$, $k_{L,T}^{ABnn}$ and two onsite interactions k_A and k_B; nn and $2nn$ stand for the nearest and second nearest neighbors respectively. Unlike model I, the acoustic sum rule is not inherently imposed in model II. Therefore for model II, the

values of the force constants (lower panel of Table 8.1) have been chosen such that the acoustic sum rule is obeyed. For both the models there are stable modes throughout the Brillouin zone, and acoustic and optical branches are well-separated. The force constants (Table I) are chosen such that both the models produce identical dispersion of the phonon modes. This will facilitate the comparison of the different properties of the phonons obtained from the two models.

Disorder is introduced by randomly selecting two different types of atoms and interchanging their positions, making sure that a given atom is interchanged only once. A configuration with nano-scale order is obtained by excluding such an interchange in the circular nano-ordered regions (NORs) with a fixed diameter of a few nanometers. Centres of these circular regions are taken randomly, but avoiding any overlap between them. The degree of disorder is quantified with a disorder parameter δ defined as:

$$\delta = \frac{N_{nn}}{N_{nn}^{T}} \tag{8.3}$$

where N_{nn} denotes the number of A-A or B-B nearest neighbors and N_{nn}^{T} denotes the total number of nearest neighbors. For a fully ordered case, $\delta = 0.0$, whereas δ is 0.5 for the completely disordered case.

For a disordered configuration, A and B occupy one of the two sites of the square lattice with equal probability, resulting in new types of neighboring pairs of atoms, such as $(\text{A-B})_{2nn}$ and $(\text{A-B})_{3nn}$. For model I the force constants are taken as $\kappa_X^{ABnn}/1.4$ and $\kappa_X^{ABnn}/2.0$ respectively, where $X = r, \theta$, whereas for model 2 they are $(\text{k}_X^{AAnn}+\text{k}_X^{BBnn})/2.0$ and $(\text{k}_X^{AA2nn}+\text{k}_X^{BB2nn})/2.0$ respectively, where $X = L, T$. Similarly, the nearest neighbor atoms of the same type can possibly be separated by $(0.5,0.5)a$, for which the force constants for model I are given by $\kappa_{X,disorder}^{YYnn} = z\kappa_X^{YY2nn}$, where $Y = A, B$ and $z = 4.0$ when $Y = A$ and $z = 2.0$ when $Y = B$. In case of model II, for similar pair of atoms,

the force constants are given by $k^{YYnn}_{X,disorder}$ =2 k^{YY2nn}_{X}, where $Y = A, B$ and $X = L, T$. The (Y-Y)$_{nn}$ and (Y-Y)$_{2nn}$ interactions for the ordered case are now the (Y-Y)$_{2nn}$ and (Y-Y)$_{3nn}$ respectively. In model II, the acoustic sum rule for the disordered case is imposed by correcting the diagonal elements of the force constant matrix [207].

Table 8.1: Force constants (in ar. units) for different interactions along different directions. The force constants in the top panel are for model I while those in the bottom panel are for model II.

Force Constants	Values	Force Constants	Values
κ_r^{ABnn}	3.5	κ_θ^{BBnn}	0.5
κ_θ^{ABnn}	1.0	κ_r^{AA2nn}	1.51
κ_r^{AAnn}	2.0	κ_θ^{AA2nn}	0.99
κ_θ^{AAnn}	0.5	κ_r^{BB2nn}	0.25
κ_r^{BBnn}	2.5	κ_θ^{BB2nn}	0.25
k_A	19.0	k_L^{BBnn}	-2.5
k_B	16.0	k_T^{BBnn}	-0.5
k_L^{AAnn}	-2.0	k_L^{BB2nn}	-0.25
k_T^{AAnn}	-0.5	k_T^{BB2nn}	0.0
k_L^{AA2nn}	-1.25	k_L^{ABnn}	-2.25
k_T^{AA2nn}	0.0	k_T^{ABnn}	-1.25

8.3 Details of calculations

The spectral density function ($S_{\mathbf{k}}(\omega)$), calculated for different configurations, allows us to relate to the constant energy scan and constant momentum transfer scan obtained in neutron scattering experiments. We use the contour plot of $S_{\mathbf{k}}(\omega)$ in visualizing the dispersion of phonon modes for systems with disorder. The spectral density function [208] is given by:

$$S_{\mathbf{k}}(\omega) = \frac{\sum_{j=1}^{2N} |\bar{\alpha}_{\mathbf{k}}^{j}|^2 \delta(\omega - \omega^{j})}{2N}, \tag{8.4}$$

where N is the total number of atoms, ω^j is the frequency of the j^{th} eigenmode and $|\bar{\alpha}^j_{\mathbf{k}}|$ is the Fourier transform of the real space eigenvector of the j^{th} eigenmode.

To probe the extended versus the localized nature of the modes in the presence of disorder and nano-ordered regions we calculate inverse participation ratio (IPR):

$$IPR(\omega_j) = N\frac{\sum_i |\vec{\alpha}^j_i|^4}{(\sum_i |\vec{\alpha}^j_i|^2)^2}, \tag{8.5}$$

where $\vec{\alpha}^j$ are the eigenstates of the phonon modes. IPR is N (1) for a fully localized (extended) mode.

The extended modes can be classified into two categories, the propagons (these propagate ballistically) and the diffusons. Wave vector k is a good quantum number for propagons, but not for diffusons. The Ioffe-Regel (I-R) cross-over [204] separates propagons and diffusons as a function of frequency. In the frequency domain, the full width at half maximum (ζ) of a peak in the spectral density function is used to obtain the decay time τ of a propagating mode due to scattering ($\tau_k^{-1} \simeq \pi\zeta_\omega(k)$) [206]. The crossover point between ω vs. k and τ^{-1} vs. k gives the location (k) of the I-R cross-over.

To further affirm this classification of modes, we studied their level spacing distribution (LSD). LSD, with its foundation in the random matrix theory (RMT), is known to exhibit Wigner-Dyson statistics for diffusons and Poisson statistics for locons [205]. We calculated level spacings distribution using *spectral unfolding*, in which the original spectrum is mapped into an ordered set of numbers with uniform density of states.

In order to explore the mixing among phonon modes due to disorder, we introduce an energy correlation function $f(\omega, \omega')$ as an overlap between the

modes of the ordered system ($|\alpha_n^O\rangle$) with those of the disordered or nano-ordered system ($|\alpha_m^D\rangle$):

$$f(\omega,\omega^{'}) = \sum_{i,j} |\langle\alpha_i^D|\alpha_j^O\rangle|^2 \delta(\omega-\omega_i)\delta(\omega^{'}-\omega_j). \tag{8.6}$$

It is based on the representation of modes of a disordered configuration as a linear combination of the normal modes of a fully ordered system. Contour plots of f enable visual picture in $\omega-$domain of mixing of modes.

8.4 Results

8.4.1 Size dependence

Using model 1, described in Section 8.2, we study vibrational modes of the completely disordered system ($\delta = 0.5$) for different sizes [32×32 unit cells (2048 atoms), 28×28 unit cells (1568 atoms) and 16×16 unit cells (512 atoms)] to test the size dependence of different properties associated with these modes.

The contour plots of the spectral density function for the phonon modes of the model system with three different sizes (Fig. 8.1) show qualitatively similar features. Moreover for the longitudinal and the transverse acoustic modes (LA and TA) ω and k for the I-R cross-over (Fig. 8.2) are size independent. The slight differences in the magnitude of ω and k are within the limits of calculational errors. The IPR plots as a function of the phonon modes energy (ω) for different system sizes (Fig. 8.3) show that the high energy modes ($\omega > 5.5$) are highly localized. Modes having energy lower than the above mentioned value of ω are the extended ones. There is a small hump around $\omega = 3.0$. The numerical value of IPR is system size dependent because of the normalization factor (eqn. 8.5). Thus different properties of the phonon modes

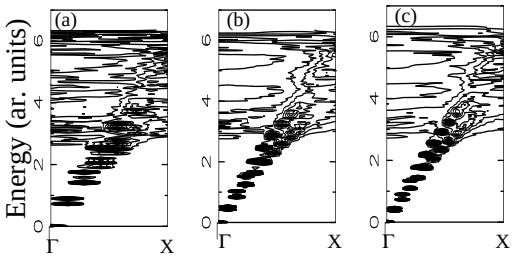

Figure 8.1: Contour plot of spectral density function. (A) 16x16, with 512 atoms, (B) 28x28, 1568 with atoms and (C) 32x32, with 2048 atoms.

are qualitatively same for all the three system sizes we have considered. Hence to study the effects of the NORs on the phonon modes, calculations are done with a system having 32x32 unit cells (2048 atoms).

8.4.2 Choice of δ

In order to observe the effects which we are interested in, the degree of disorder in the system should be sufficient to induce strong mixing of acoustic and optical modes. In order to choose a proper strength of disorder, we calculate, using model 1, the value of k and ω at which I-R crossover takes place in configurations having two different values of δ. At $\delta = 0.3$, the effect of the disorder is not strong enough to induce strong mixing of the phonon modes which is necessary to observe the waterfall phenomenon. For configurations with $\delta \leq 0.3$ no I-R crossover is observed (Fig. 8.4), indicating that the disorder is not strong enough to induce mixing of the phonon modes. Hence for a detailed study of the effect of nano-ordered regions and disorder on the properties of the phonon modes, we choose the configuration with $\delta \simeq 0.4$.

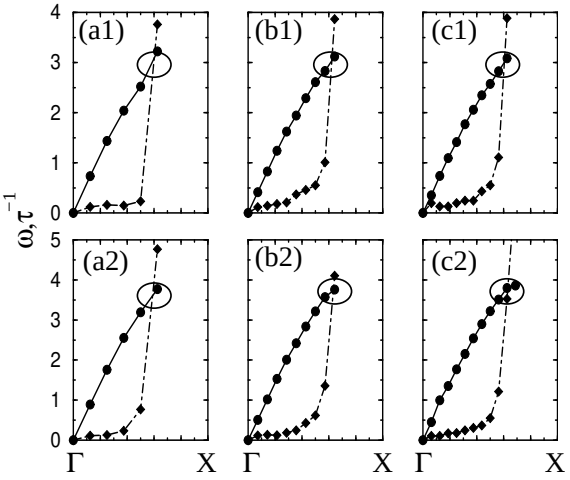

Figure 8.2: Acoustic branch frequency (solid lines) and its inverse decay time (dot-dashed lines) as a function of wavevector for different system sizes ((a) 16x16, (b) 28x28 and (c) 32x32 using model I. Point of their cross-over is indicated by an ellipse. The top panel is for the transverse modes whereas the bottom panel is for the longitudinal ones. The values of ω and k, for different system sizes and polarization, at which cross-over take place are: (a1) 3.08 and 0.30, (a2) 3.60 and 0.30, (b1) 3.03 and 0.31, (b2) 3.73 and 0.32, (c1) 3.01 and 0.30 and (c2) 3.80 and 0.31 respectively.

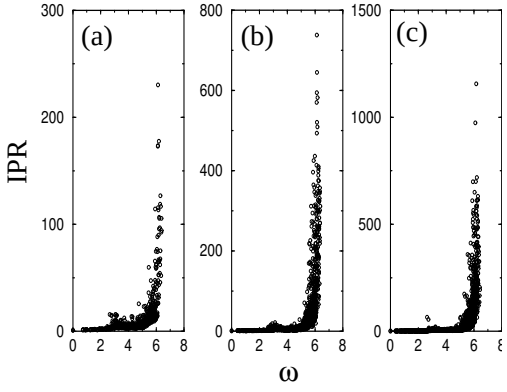

Figure 8.3: IPR as a function of frequency (using model I) of the phonon modes for different system sizes: (A) 16x16, (B) 28x28 and (C) 32x32.

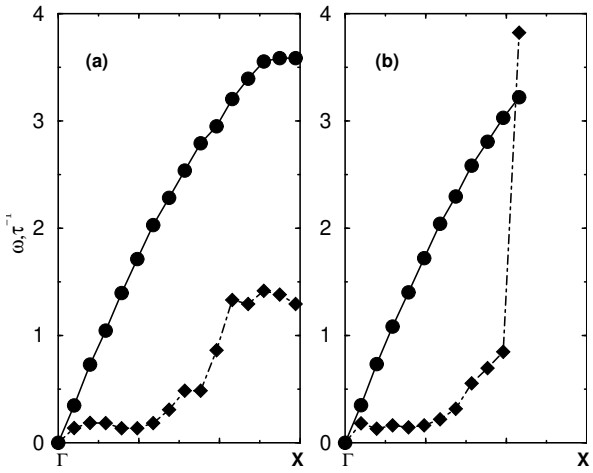

Figure 8.4: I-R crossover for TA modes (obtained using model I): (a) δ =0.3 and (b) δ =0.4. For (b) the I-R crossover takes place at ω =3.18 units and $k = 0.34$ r. l. u.

8.4.3 Effect of disorder and NORs on phonon modes.

Dispersion of phonon modes.

Phonon dispersion of the ordered system along the $\langle 10 \rangle$ direction obtained from dynamical matrix and from $S_k(\omega)$ are compared in Figs. 8.5(a) and 8.5(b) for model 1. At X point, the longitudinal optical branch (LO) has the highest energy, whereas the transverse optical (TO) branch is degenerate with the LA branch. Finite width of the peaks in the contour plot of $S_k(\omega)$ arise from the width of Gaussian used to approximate the delta function in Eqn (8.4). Based on a reasonable agreement between the two descriptions, we use $S_k(\omega)$-based description in the study of phonons of systems with disorder. Our results for phonons of nano-ordered and disordered configurations (Fig. 8.5, (c)-(f)) show that the introduction of disorder results in mixing of the phonon modes and subsequent broadening of peaks in $\mathrm{S}_k(\omega)$ as a function of both k and ω, k is no longer a good quantum number to describe these modes. With the increase in the number of NORs the mixing of the modes increases (Fig. 8.5, (c)-(e)). While new modes with intermediate energies appear near the Γ point, long

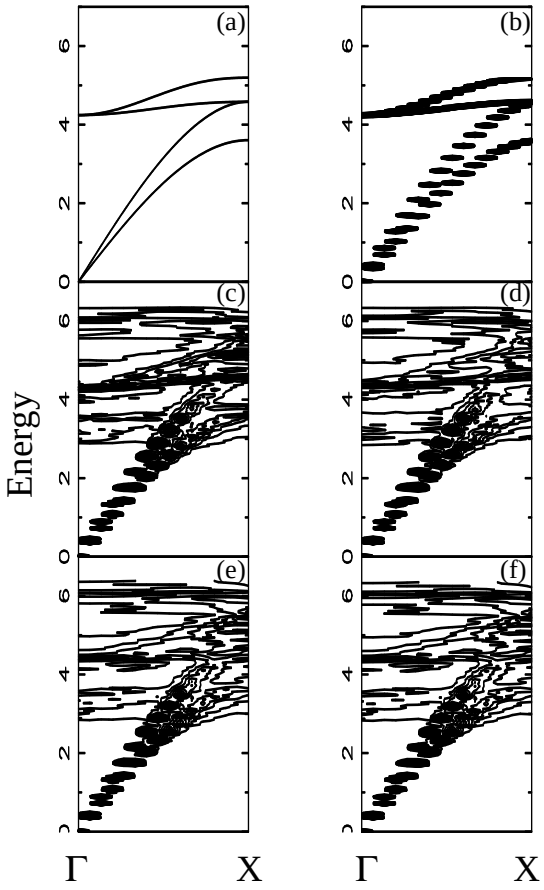

Figure 8.5: Phonon dispersion obtained from (a) the dynamical matrix of ordered system, and (b, c, d, e, f) contour plots of $S_{\mathbf{k}}(\omega)$ for the ordered system, a nano-ordered system with two NORs (each of radius $\approx 5.0\ a$), eight NORS (each of radius $\approx 3.0\ a$), fourteen NORs (each of radius $\approx 2.2\ a$) and a fully disordered system respectively. All these calculations are done with the interaction potential given in Eqn. 8.1.

wavelength acoustic modes for $k \lesssim 0.33$ are least affected. This is consistent with the error-bars on phonon measurements using inelastic neutron scattering technique [196].

IPR, I-R crossover and the level spacing distribution.

The IPR plots as a function of energy for the nano-ordered and disordered configurations show qualitatively similar features (Fig. 8.6). The modes having $\omega < 5.5$ are extended whereas those beyond $\omega \geq 5.5$ are highly localized. Moreover with the increease in the number of NORs, the number of localized modes increases. Thus the presence of the NORs strengthens the effect of the disorder in the system.

In order to classify the extended modes into propagons and diffusons we find out the I-R crossover. For the LA modes the cross-over occurs at $3.81 \leq \omega \leq 3.95$ and $k \approx 0.33$ r.l.u. (Fig. 8.7) for different configurations of the nano-ordered system and disordered system. The I-R crossover for the TA modes occurs at $3.18 \leq \omega \leq 3.25$ and $k \approx 0.33$ r.l.u. (Fig. 8.8). Hence all the modes below $\omega \leq 3.18$ are propagons, i.e., this modes propagate ballistically and k is a good quantum number to describe them. However for the modes with $\omega \geq 3.18$, k is no longer a good quantum number. Among these modes for which the IPR values are very small, $3.18 < \omega < 5.5$, are called extendons because they are not completely localized.

To further affirm this classification of modes, we studied their level spacing distribution (LSD). We find that the LSD for modes with $3.18 < \omega < 5.5$ obey Wigner-Dyson statistics (Fig. 8.9) whereas those with $\omega > 5.5$ obey Poisson statistics (Fig. 8.10) with slight deviation near zero spacing. For the locons we get a bad fit of the LSD to the Poisson statics. This is because of two reasons: firstly diffusons are also present among the modes with $\omega > 5.5$ and secondly it is hard to draw a distinct boundary between ω of diffusons and locons. For

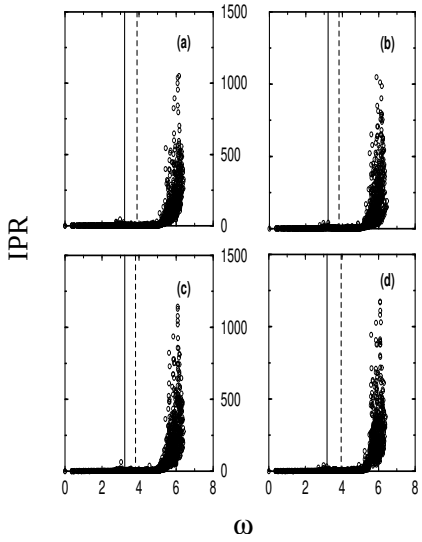

Figure 8.6: IPR as a function of energy for model I, (a) n=2, (b) n=8, (c) n=14 and (d) n=0.

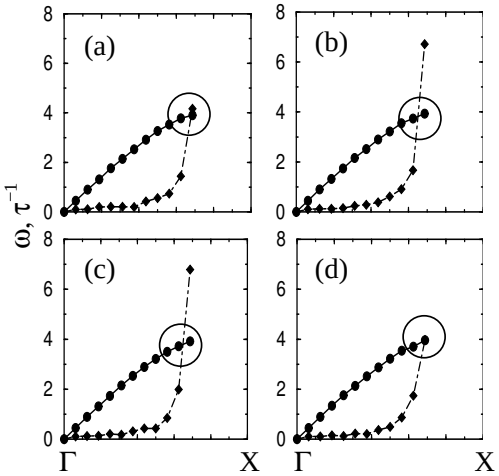

Figure 8.7: IR cross-over (using model I) for LA modes, (a) n=2, (b) n=8, (c) n=14 and (d) n=0. The values of ω and k at which the cross-over take place are (a) 3.89 and 0.34, (b) 3.82 and 0.33, (c) 3.81 and 0.33 and (d) 3.95 and 0.34 respectively.

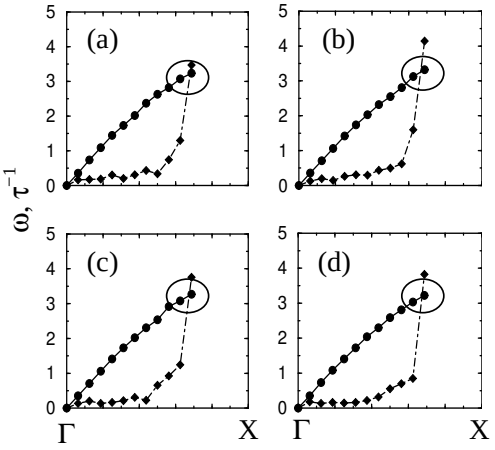

Figure 8.8: IR cross-over (using model I) for TA modes, (a) n=2, (b) n=8, (c) n=14 and (d) n=0. The values of ω and k at which the cross-over take place are (a) 3.22 and 0.34, (b) 3.25 and 0.33, (c) 3.23 and 0.33 and (d) 3.18 and 0.34 respectively.

those modes with $\omega > 5.5$ if we filter out the diffusons (we excluded those modes whose IPR is less than or equal to the maximum value of IPR for the modes with $3.18 < \omega < 5.5$), the peak of the curve shifts towards the origin.

Energy correlation

The contour plots of $f(\omega, \omega^{'})$ (Fig. 8.11) clearly show that the acoustic modes of nano-ordered system in the IR-crossover region ($\omega \sim 2.4$) emerge from mixing of optical modes ($\omega \sim 4.2$) of the ordered system. At a fixed degree of disorder, this mixing becomes stronger with the number of nano-ordered regions. Secondly, diffuson modes in the optical region of the spectrum of a nano-ordered system arise mainly from mixing among optical modes with different wave vector.

Optical modes at Γ point

To understand the nature of diffusons, we show in Fig. 8.12 the $k-$dependence of $S_\omega(k)$ for $\omega \simeq 4.34 \pm 0.05$ corresponding to peaks of S at the Γ point for a

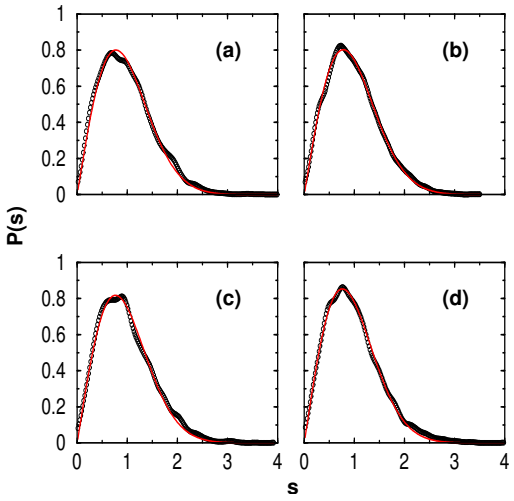

Figure 8.9: LSD for U_{ij}^{I}-model diffusons (3.18< ω <5.5), (a) n=2, (b) n=8, (c) n=14 and (d) n=0. The black circles represent the calculated value of LSD whereas the red line represents the data obtained from fitting the calculated value to the desired statistics (For the present case the data has been fitted to Wigner-Dyson statistics.)

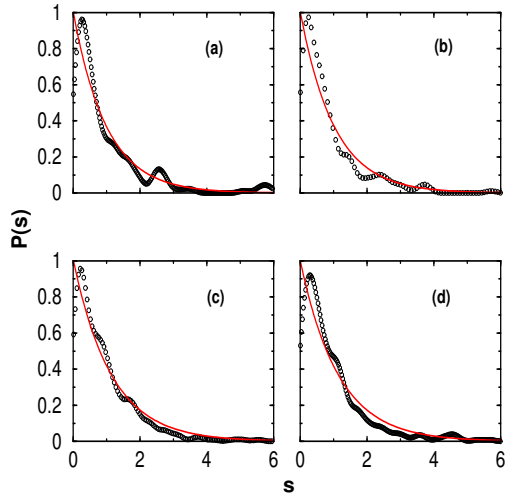

Figure 8.10: LSD of locons (for U_{ij}^{I}, ω >5.5). (a) n=2, (b) n=8, (c) n=14 and (d) n=0.

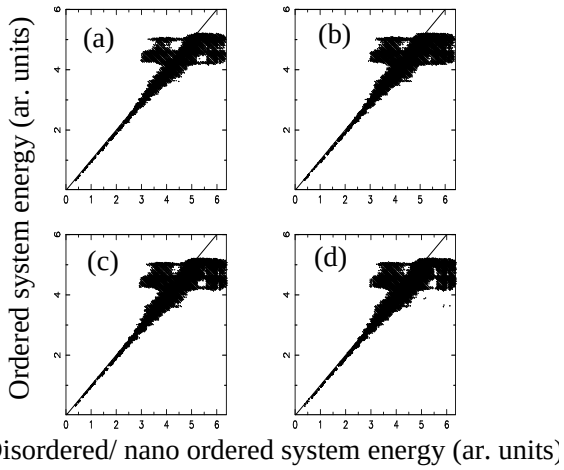

Figure 8.11: Energy correlation between the modes of ordered system and that of a configuration having (a) n=2, (b) n=8, (c) n=14 and (d) n=0 NORs. The straight line shows perfect correlation or *NO* mixing. The interaction between two atoms is described by Eqn. 8.1.

given configuration. It shows that the probability of finding a long wavelength optical mode decreases as the number of nano-ordered regions increases, as many of these degrees of freedom precipitate into the acoustic branches due to strong mixing. Correspondingly, the uncertainty in momentum $\hbar k$, which is given by the full width at half maximum (FWHM) of a peak in spectral-density also increases. For configurations having fourteen or more nano-ordered regions, there is no well-defined peak for which the FWHM can be estimated.

8.4.4 Comparison with model *II*

For the different properties of the phonon modes discussed above, we compare them with model 2 to confirm that the effects which we have observed so far are not artefact of the potential we are using to describe the interaction between the two atoms. Fig. 8.13 shows that the dispersion of phonon modes obtained from model 2 (Eqn. 8.2). A comparison of Figs. 8.13 and 8.5 shows that the dispersion of the phonon modes obtained from the models have qualitatively similar features. The IPR of the phonon modes obtained from model 2 (Fig.

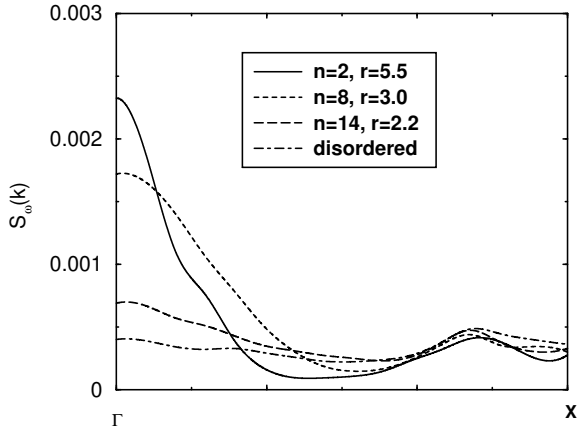

Figure 8.12: Probability of finding an optical mode in the long wavelength limit (using model I). "r" denotes the radius of each nano-ordered region. These modes have energy ω=4.34±0.05 units.

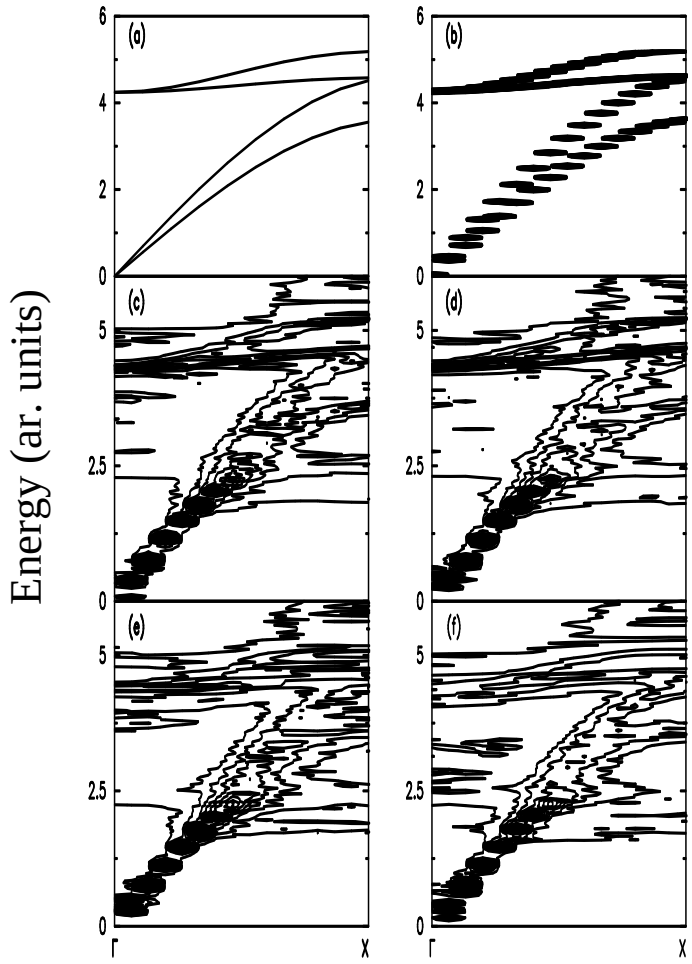

Figure 8.13: Phonon dispersion for the same configurations described in Fig. 8.5 but with interaction potential given in Eqn. 8.2.

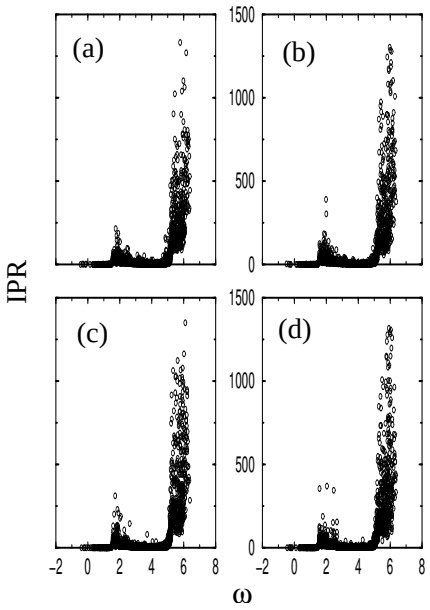

Figure 8.14: IPR as a function of energy for model II, (a) n=2, (b) n=8, (c) n=14 and (d) n=0. The solid line and the dashed one show the positions of I-R crossover for TA and LA modes respectively.

8.14) is also qualitatively similar to that obtained from model 1 (Fig. 8.6). The difference between the two models is that for model 2 the I-R cross-over takes place at a lower value of ω ($2.22 \leq \omega \leq 2.32$ for the LA modes) and k (k=0.23 r. l. u.). The lowering of k and ω values at which the I-R crossover takes place for model 2, suggests that the effect of disorder is stronger in model 2 compared to model 1. Like model 1 the probability of finding the optical modes at Γ point (Fig. 8.12 and 8.16) decreases with the increase in the number of NORs. The fact that both the models show qualitatively similar results strengthens our claim that the different properties of the phonon modes are not the artefact of the model under consideration but are the true effects of presence of nano-ordered regions in the disordered matrix.

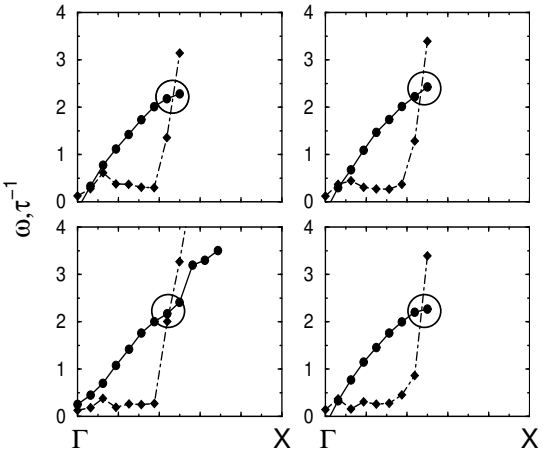

Figure 8.15: IR crossover for LA modes with U_{ij}^{II} as the interaction potential between the atoms for (a) n=2, (b) n=8, (c) n=14 and (d) n=0 configurations and $\delta = 0.4$. The values of ω and k (in r. l. u.) for which the IR crossover takes place are (a)2.22 and 0.23, (b)2.32 and 0.23, (c) 2.22 and 0.22 and (d)2.23 and 0.23 respectively.

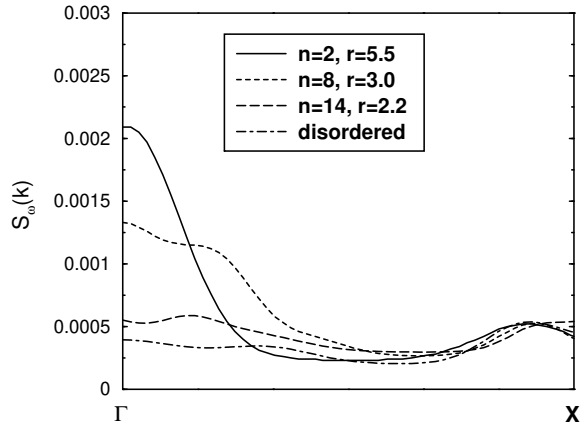

Figure 8.16: Probability of finding an optical mode in the long wavelength limit (using model II). "r" denotes the radius of each nano-ordered region. These modes have energy ω=4.292±0.034 units.

8.5 Discussion and summary

Due to scattering from chemical disorder, optical modes (propagons) of the ordered system become diffusive. We suggest that the diffusons should be relevant to the diffuse dynamical properties of relaxors or diffuse phase transition behavior in ferroelectrics. While the phonons considered here are hard (high frequency) and treated within harmonic approximation, those in real ferroelectrics are soft and exhibit strong anharmonicity. Scattering of soft modes due to disorder is expected to be even stronger and their anharmonicity will lead to scattering among phonons. As the present work is on a 2-D system and some of its features are likely to be qualitatively different in 3-D, precise implications for the real relaxors need further investigation.

In connection with the waterfall phonon anomaly, our results show that nano-ordered regions of large enough size *are* essential for the observation of phonons with a definite wave-vector. Secondly, their size does affect the strength of mixing between optical and acoustic modes, though not the wavevector corresponding to the I-R crossover. The former is the basis of mode-coupling model and latter is consistent with the conclusion of Hlinka et al [198]. We note that the NPR's (not NORs) are present in conventional ferroelectrics too (like the chain-like dynamic polar distortions in $KNbO_3$ [209]) over a narrow temperature range above T_c and "waterfall phenomenon" should be more general. As the acoustic modes essentially span configurations with inhomogeneous strain, the coupling of inhomogeneous strain with polar optical modes seems to be the common origin of "waterfall phonons" and also the relaxor dynamics [210].

In summary, we find that chemical disorder on a 2-D lattice results in phonon modes of type: propagons, diffusons and locons. A detailed study of the properties of phonon modes with different system sizes and with two different interacting potentials suggest that the results shown here are neither

the effect of finite system size nor are they the artefact of the potential in use. At the fixed degree of disorder, reduction in the size of nano-ordered regions results in increase (decrease) in the width (height) of peaks corresponding to long wavelength optical modes as a function of k. This correlates with corresponding increase in the mixing between optical and acoustic modes. While the length-scale of chemical ordering needs to be large enough (a few nanometre) for observing optical phonon modes with a definite momentum, it also has to be small to give adequate mixing with acoustic modes responsible for the "waterfall phonons".

Bibliography

[1] A. J. Cox, J. G. Louderback, and L. A. Bloomfield, Phys. Rev. Lett. **71**, 923 (1993).

[2] S. Titmuss, A. Wander and D. A. King, Chem. Chem., **96**, 1291 (1996).

[3] Y. Ji and J. A. Yeomans, J. Mat. Sc. **37**, 5229 (2004).

[4] P. Hohenberg and W. Kohn, Phys. Rev. **136**, 864B (1964).

[5] W. Kohn and L. J. Sham, Phys. Rev. **140**, 1133A (1965).

[6] Ujjal K. Goutam and C. N. R. Rao, J. Mater. Chem., **14**, 2530 (2004).

[7] Zhaoping Liu, Shu Li, You Yang, Zhaokang Hu, Sheng Peng, Jianbo Liang and Yitai Qian, New J. Chem., **27**, 1748 (2003).

[8] Shaswati Sen *et al.*, BARC, India, Private communication.

[9] R. M. Martin, Electronic Structure , Cambridge University Press.

[10] D. M. Ceperley, Phys. Rev. Lett. **45**, 566 (1980).

[11] J. P. Perdew and A. Zunger, Phys. Rev. B **23**, 5048 (1981).

[12] A. D. Becke, Phys. Rev. A **38**, 3098 (1988).

[13] Y. Wang and J. P. Perdew, Phys. Rev. B **43**, 8911 (1991).

[14] J. P. Perdew, K. Burke, and M. Ernzerhof, Phys. Rev. Lett. **80**, 891 (1998).

[15] P. P. Ewald, Ann. Phys. (Leipzig) **54**, 519 (1917).

[16] P. P. Ewald, Ann. Phys. (Leipzig) **54**, 557 (1917).

[17] P. P. Ewald, Ann. Phys. (Leipzig) **64**, 253 (1921).

[18] P. Pulay, Mol. Phys. **17**, 197 (1969).

[19] H. Hellmann, *Einfuhrung in die Quantumchemie*, Franz Deutsche, Leipzig (1937).

[20] R. P. Feynman, Phys. Rev. **56**, 340 (1939).

[21] D. Vanderbilt, Phys. Rev. B. **41**, 8412 (1990).

[22] Hendrik J. Monkhorst and James D. Pack, Phys. Rev. B **13**, 5188 (1976).

[23] C.-L. Fu and K.-M. Ho, Phys. Rev. B **28**, 5480 (1983).

[24] M. Methfessel and A. T. Paxton, Phys. Rev. B **40**, 3616 (1989).

[25] N. Marzari, D. Vanderbilt, A. De Vita and M. C. Payne, Phys. Rev. Lett. **82**, 3296 (1999).

[26] O. H. Nielsen and R. M. Martin, Phys. Rev. Lett. **50**, 697 (1983).

[27] O. H. Nielsen and R. M. Martin, Phys. Rev. B **32**, 3780 (1985).

[28] M. Born and K. Huang, Dynamical Theory of Crystal Lattices, Oxford University Press (1954).

[29] E. N. Zein, Fiz. Tverd. Tela (Leningrad), **26**, 3024 (1984) [Sov. Phys. Solid State, **26**, 1825 (1984)].

[30] S. Baroni, P. Giannozzi and A. Testa, Phys. Rev. Lett. **58**, 1861 (1987).

[31] S. Baroni, S. de Gironcoli, A. D. Corso, P. Giannozzi, Rev. Mod. Phys. **73**, 515 (2001).

[32] P. D. De Cicco and F. A. Johnson, Proc. R. Soc. London, Ser. A **310**, 111 (1969).

[33] R. Pick, M. H. Cohen, R. M. Martin, Phys. Rev. B, **1**, 910 (1970).

[34] (a) H. M. Huang, S. Mao, H. Feick, H. Yan, Y. Wu, H. Kind, E. Weber, R. Russo, P. Yang, Science **292**, 1897 (2001). (c) S.-W. Chung, J.-Y. Yu, J. R. Heath, Appl. Phys. Lett. **76**, 2068 (2000).

[35] (a) J. Hu, T. W. Odom, C. Lieber, Acc. Chem. Res. **32**, 435 (1999). (b) S. M. Prokes, K. L. Wang, MRS Bull., **24 No.8**, 13 (1999). (c) Z. L. Wang, Adv. Mater., **12**, 1295 (2000).

[36] (a) E. Gerlach and P. Grosse, The physics of selenium and tellurium, Springer-Verlag, Berlin Heidelberg, (1979), (b) E. D. Cooper, Tellurium, Van Nostrand Reinhold Co., New York, 1974.

[37] (a) A. A. Kudryavstev, The Chemistry and Technology of Selenium and Tellurium, Collet's Ltd., London, 1974, (b) P. Tangney and S. Fahy, Phys. Rev. B, **65** 54302 (2002).

[38] X. Gonze, J.-M. Beuken, R. Caracas, F. Detraux, M. Fuchs, G.-M. Rignanese, L. Sindic, M. Verstraete, G. Zerah, F. Jollet, M. Torrent, A. Roy, M. Mikami, Ph. Ghosez, J.-Y. Raty, D.C. Allan., Computational Materials Science **25**, 478-492 (2002). URL http://www.abinit.org.

[39] S. Goedecker, SIAM J., Scientific Computing, **18**, 1605 (1997).

[40] M.C. Payne, M.P. Teter, D.C. Allan, T.A. Arias and J.D. Joannopoulos, Rev. Mod. Phys. **64**, 1045 (1992).

[41] A. M. Rappe, K. M. Rabe, E. Kaxiras, and J. D. Joannopoulos, Phys. Rev. B **41**, 1227 (1990).

[42] URL http://opium.sourceforge.net/guide.html

[43] J. P. Perdew, K. Burke, and M. Ernzerhof, Phys. Rev. Lett., **77**, 3865 (1996).

[44] J. P. Perdew, K. Burke, and M. Ernzerhof, Phys. Rev. Lett. **78**, 1396 (1997).

[45] (a) C. G. Broyden, J. Inst. Math Appl. **6**, 76 (1970), (b) R. Fletcher, J. Comput. **13**, 317 (1970), (c) D. Goldfarb, Math. Comp. **24**, 23 (1970), (d) D. F. Shanno, Math. Comp. **24**, 647 (1970).

[46] Kazuma Nakamura and Atsushi Ikawa, Phys. Rev. B **66**, 024306 (2002).

[47] E. Hernandez and Angel Rubio, Newsletter **32**, 48, April 1999; http://psi-k.dl.ac.uk/newsletters/News_32/newsletter_32.pdf.

[48] Matteo Cococcioni, Francesco Mauri, Gerbrand Ceder and Nicola Marzari, Phys. Rev. Lett. **94**, 145501 (2005).

[49] We also evaluated the radius of Te-h, Te-w1 and Te-w2 using the definition given in Ref. 48. Using this definition, we obtain radii of Te-h, Te-w1 and Te-w2 as 3.1 Å, 6.39 Åand 10.22 Årespectively. With these values of radii, the surface energy (γ_s) for the three systems are 0.10 J/m^2, 0.13 J/m^2 and 0.15 J/m^2 respectively and the Young's modulus (Y) are 34.46 GPa for Te-h and 40.69 GPa for Te-w1. Although the values of γ_s and Y change depending on the definition of the radius we use, their trends as a function of the radius of nanowires are similar to our results.

[50] http://www.webelements.com

[51] N. Troullier and Jose Luis Martins, Phys. Rev. B **43**, 1993 (1991).

[52] G. Kresse, J. Furthmuller and J. Hafner, Phys. Rev. B **50**, 13181 (1994).

[53] D. R. McCann and L. Cartz, J. Appl. Phys. **43**, 4473 (1972); W.Lingelbach, J. Stuke, G. Weiser and J. Trensch, Phys. Rev. B **5**, 243 (1972).

[54] C. Kittel, Introduction to Solid State Physics, 7th ed. (Wiley, New York, 1996), p. 57, 59.

[55] J. D. Joannopoulos, M. Schluter and M. L. Cohen, Phys. Rev. B **11**, 2186 (1975).

[56] C. Kittel, Introduction to Solid State Physics, 7th ed. (Wiley, New York, 1996), p. 201.

[57] A. Kokalj, XCrySDen–a new program for displaying crystalline structures and electron densities, J. Mol. Graphics Modelling, 1999, **17**, 176-179. Code available from http://www.xcrysden.org/.

[58] R. Kubo, J. Phys. Soc. Jpn. **12**, 570 (1957).

[59] D. A. Greenwood, Proc. Phys. Soc. London **71**, 585 (1958).

[60] S. Tutihasi, G. G. Roberts, R. C. Keezer and R. E. Drews, Phys. Rev. **177**, 1143 (1969).

[61] Th. Starkloff and J. D. Joannopoulos, Phys. Rev. B **19**, 1077 (1979).

[62] R. Steudel, Z. Anorg. Allg. Chem. **139**, 478 (1981).

[63] R. Steudel and E. M. Strauss, Adv. Inorg. Chem. Radiochem. **135**, 35 (1984).

[64] K. F. Willey, P. Y. Cheng, T. G. Taylor, M. B. Bishop and M. A. Duncan, J. Phys. Chem. **94**, 1544 (1990).

[65] A. Benamar, D. Rayane, P. Melinon, B. Tribollet, and M. Z. Broyer, Phys. D: At. Mol. Clusters **19**, 237 (1991).

[66] H. Ito, T. Sakurai, T. Ichihara and I. Katakuse, Surf. Rev. Lett. **3**, 577 (1996).

[67] P. Hassanzadeh, C. Thompson and L. Andrews, J. Phys. Chem. **96**, 8246 (1992).

[68] G. Igel-Mann, H. Stoll and H. Preuss, Mol. Phys. textbf80, 341 (1993).

[69] J. D. Goddard, X. Chen and G. Orlova, J. Phys. Chem. A **103**, 4078 (1999).

[70] Z. Q. Li, J. Z. Yu, K. Ohno, B. L. Gu, R. Czajka, A. Kasuya, Y. Nishina and Y. Kawazoe, Phys. Rev. B **52**, 1524 (1995).

[71] B. C. Pan, Phys. Rev. B **65**, 085407 (2002).

[72] J. Bhattacharjee and U V Waghmare, Phys. Rev. B **71**, 045106 (2005).

[73] R. M. Martin and G. Lucovsky, Phys. Rev. B **13**, 1383 (1976).

[74] P. Ghosh, M. U. Kahaly and U. V. Waghmare, Phys. Rev. B **75**, 245437 (2007).

[75] J. H. Rose, J. R. Smith, F. Guinea and J. Ferrante, Phys. Rev. B **29** 2963 (1984).

[76] J. T. Kumar, J. Phys. Chem., **90**, 4747 (1986).

[77] K. C. Taylor, Catal. Rev. Sci. Eng., **35**, 433 (1993).

[78] R. Dumpelmann, N. W. Cant and D. L. Trimm, Catal. Lett., **32**, 357 (1995).

[79] Z-P. Liu, Pure Appl. Chem., **76**, 2069 (2004).

[80] S. Hagstrom, H. B. Lyon and G. A. Somorjai, Phys. Rev. Lett. , **15**, 491 (1965).

[81] M. A. Van Hove, R. J. Koestner, P. C. Stair, J. P. Bibérian, L. L. Kesmodel, I. Bartŏs and G. A. Somrjai, Surf. Sci., **103**, 189 (1981).

[82] N. Bickel and K. Heinz, Surf. Sci., **163**, 435 (1985).

[83] E. Lang, K. Muller, K. Heinz, M. A. Van Hove, R. J. Koestner and G. A. Somorjai, Surf. Sci., **127**, 347 (1983).

[84] G. Gilarowsky, J. Méndez and H. Niehus, Surf. Sci., **448**, 290 (2000).

[85] M. Gruyters, A. T. Pasteur, and D. A. King, J. Chem. Soc., Faraday Trans. **92**, 2941 (1996).

[86] A. Schmidt, W. Meier, L. Hammer, and K. Heinz, J. Phys.: Condens. Matter **14**, 12353 (2002).

[87] S. Lehwald, J. G. Chen, G. Kisters, E. Preuss and H. Ibach, Phys. Rev. B, **43**, 3920 (1991).

[88] V. Fiorentini, M. Methfessel and M. Scheffler, Phys. Rev. Lett., **71**, 1051 (1993).

[89] A. Filippetti and V. Fiorentini, Surf. Sci., **377-379**, 112 (1997).

[90] Q. Ge, D. A. King, N. Marzari, and M. C. Payne, Surf. Sci. **418**, 529 (1998).

[91] P. A. Thiel, R. J. Behm, P. R. Norton, and G. Ertl, Surf. Sci. **121**, L553 (1982).

[92] A. Hopkinson, J. M. Bradley, X. C. Guo, and D. A. King, Phys. Rev. Lett. **71**, 1597 (1993).

[93] A. Hopkinson, X. C. Guo, J. M. Bradley, and D. A. King, J. Chem. Phys. **99**, 8262 (1993).

[94] E. Ritter, R. J. Behm, G. Pötschke, and J. Wintterlin, Surf. Sci. **181**, 403 (1987).

[95] P. van Beurden, B. S. Bunnik, G. J. Kramer, and A. Borg, Phys. Rev. Lett. **90**, 066106 (2003).

[96] T. Ali, B. Krotzer, A. V. Walker, and D. A. King, J. Chem. Phys.**109**, 10996 (1998).

[97] T. Ali, B. Krotzer, A. V. Walker, Q. Ge, and D. A. King, J. Chem. Phys. **109**, 9967 (1998).

[98] A. Deskins, J. Lauterbach, and K. T. Thomson, J. Chem. Phys. **122**, 184709 (2005).

[99] Y.Y. Yeo, C.E. Wartnaby and D.A. King, Science **268**, 1731 (1995).

[100] S. Khatua, Z.-P. Liu and D. A. King, Surf. Sc. **584**, 214 (2005).

[101] R. J. Behm, P. A. Thiel, P. R. Norton, and G. Ertl, J. Chem. Phys. **78**, 7437 (1983).

[102] T. E. Jackman, K. Griffiths, J. A. Davies, and P. R. Norton, J. Chem. Phys. **79**, 3529 (1983).

[103] H. Hopster, H. Ibach, and G. Comsa, J. Catalysis **46**, 37 (1977).

[104] A. Borg, A.-M. Hilmen, and E. Bergene, Surf. Sci. **306**, 10 (1994).

[105] P. van Beurden and G. J. Kramer, J. Chem. Phys. **121**, 2317 (2004).

[106] S. Khatua, S.J. Pratt and D.A. King, to be submitted.

[107] A. Hopkinson and D. A. King, Chem. Phys. **177**, 433 (1993).

[108] A. Hopkinson and D. A. King, Faraday Discuss **6**, 255 (1993).

[109] M. Gruyters, T. Ali, and D. A. King, Chem. Phys. Lett. *232*, 1 (1995).

[110] M. Gruyters, T. Ali, and D. A. King, J. Phys. Chem. *100*, 14417 (1996).

[111] A. V. Walker, M. Gruyters, and D. A. King, Surf. Sci. **384**, L791 (1997).

[112] G. Nicolis and F. Baras, Chemical Instabilities (Reidel, Dordrecht, 1984).

[113] A.T. Anghel, R.B. Hoyle, I.M. Irurzun, M.R.E. Proctor and D.A. King, to be published.

[114] D. Passerone, F. Ercolessi, and E. Tosatti, Surf. Sci. **454-456**, 947 (2000).

[115] K. Heinz and G. Besold, Surf. Sci. **125**, 515 (1983).

[116] CRC Handbook of Chemistry and Physics, editor-in-chief David R. Lide, 84th edition (2003-2004).

[117] Y. Y. Yeo, L. Vattuone, and D. A. King, J. Chem. Phys. **104**, 3810 (1996).

[118] G. P. Brivio and M. I. Trioni, Rev. Mod. Phys. **71**, 231 (1999).

[119] J. L. Whitten and H. Yang, Surf. Sci. Rep. **218**, 55 (1996).

[120] B. Hammer and J. K. Norskov, Adv. Cat. **45**, 71 (2000).

[121] D. Loffreda, D. Simon and P. Sautet, J. Cat. **213**, 211 (2003).

[122] F. Bondino, G. Comelli, A. Baraldi, R. Rosei, A. Goldoni, S. Lizzit, C. Bungaro, S. de Gironcoli and S. Baroni, J. Chem. Phys. **119**, 12525 (2003).

[123] R. M. Wolf, J. W. Bakker and B. E. Nieuwenhuys, Surf. Sci. **246**, 135 (1996).

[124] M. Shelef and G. W. Graham, Catal. Rev. Sci. Eng. **36**, 433 (1994).

[125] B. E. Nieuwenhuys, Adv. Catal. **44**, 259 (1999).

[126] K. C. Taylor, Catal. Rev. Sci. Eng. **35**, 457 (1993).

[127] M. Date, H. Okuyama, N. Takagi, M. Nishijima and T. Aruga, Surf. Sci. **350**, 79 (1996).

[128] S. M. Vesecky, D. R. Rainer and D. W. Goodman, J. Vac. Sci. Technol. A **14**, 1457 (1996).

[129] C. T. Campbell and J. M. White, App. Surf. Sci. **1**, 347 (1978).

[130] S. B. Schwartz, G. B. Fisher and L. D. Schmidt, J. Phys. Chem. **92**, 389 (1998).

[131] H. J. Borg, J. F. C.-J. M. Reijerse, R. A. van Santen and J. W. Niemantsverdriet, J. Chem. Phys. **101**, 10052 (1994).

[132] D. N. Belton, C. L. DiMaggio, S. J. Schmieg and K. Y. Simon, J. Catal. **157**, 559 (1995).

[133] D. Loffreda, F. Delbecq, D. Simon, and P. Sautet, J. Chem. Phys. **115**, 8101 (2001).

[134] P. R. Watson, F. R. Shepherd, D. C. Frost and K. A. R. Mitchell, Surf. Sci. **72**, 562 (1978).

[135] W. Oed, B. Dötsch, L. Hammer, K. Heinz and K. Müller, Surf. Sci. **207**, 55 (1988).

[136] A. M. Begley, S. K. Kim, F. Jona and P. M. Marcus, Phys. Rev. B **48**, 12326 (1993).

[137] P. J. Feibelman and D. R. Hamann, Surf. Sci. **234**, 377 (1990).

[138] M. Methfessel, D. Hennig and M. Scheffler, Phys. Rev. B **46**, 4816 (1992).

[139] J.-H. Cho and M.-H. Kang, Phys. Rev. B **52**, 13805 (1995).

[140] D. Menzel, Surf. Sci. **318**, 437 (1994).

[141] I. Morrison, D. M. Bylander and L. Kleinman, Phys. Rev. Lett. **71**, 1083 (1993).

[142] J.-H. Cho and M. Scheffler, Phys. Rev. Lett. **78**, 1299 (1997).

[143] A. Goldoni, A. Baraldi, G. Comelli, S. Lizzit and G. Paolucci, Phys. Rev. Lett. **82**, 3156 (1999).

[144] S. Blügel, Phys. Rev. Lett. **68**, 851 (1992).

[145] N. Stojić, N. Binggeli and M. Altarelli, Phys. Rev. B **73**, 100405(R) (2006).

[146] R. J. Emrich, A. N. Mansour, D. E. Sayers, S. T. McMillan and J. R. Katzer, J. Phys. Chem. **89**, 4261 (1985).

[147] R. Wu and A. J. Freeman, Phys. Rev. B **51**, 5408 (1995).

[148] S. Nobkin, J. Limtrakul and K. Hermansson, Surf. Sci. **566-568**, 977 (2004).

[149] J. S. Villarrubia and W. Ho, J. Chem. Phys. **87**, 750 (1987).

[150] J. S. Villarrubia, L.J. Richter, B.A. Giurney and W. Ho, J. Vac. Sci. Technol. A **4**, 1487 (1986).

[151] M.F.H. van Tol and B.E. Niuwenhuys, Appl. Surf. Sci. **67**, 188 (1993).

[152] M.-H. Tsai and K. C. Hass, Phys. Rev. B **51**, 14616 (1995).

[153] K. C. Hass, M.-H. Tsai and R. V. Kasowski, Phys. Rev. B **53**, 44 (1996).

[154] W. Mannstadt and A. J. Freeman, Phys. Rev. B **55**, 13298 (1997).

[155] S. Baroni, A. Dal Corso, S. de Gironcoli, P. Giannozzi, C. Cavazzoni, G. Ballabio, S. Scandolo, G. Chiarotti, P. Focher, A. Pasquarello, K. Laasonen, A. Trave, R. Car, N. Marzari, A. Kokalj, http://www.pwscf.org/.

[156] P. Villars and L. D. Calvert, *Pearson's Handbook of Crystallographic Data for Intermetallic Phases*, American Society for Metals, Metals Park, OH, 1985.

[157] B.G. Johnson, P.M.W. Gill, and J.A. Pople, J. Chem. Phys. **98**, 5612 (1993).

[158] R. W. G. Wyckoff, Crystal Structures (Interscience, New York, 1964), Second Ed.

[159] K.W. Jacobsen, J.K. Norskov and M.J. Puska, Phys. Rev. B **35**, 7423 (1987).

[160] M. S. Daw and M. I. Baskes, Phys. Rev. Lett. **55**, 2618 (1985).

[161] G. Teeter and J.L. Erskine, Surf. Rev. Lett. **6**, 813 (1999).

[162] D. R. Alfonso, J. A. Snyder, J. E. Jaffe, A. C. Hess and M. Gutowski, Phys. Rev. B **62**, 8318 (2000).

[163] A. Baraldi, L. Bianchettin, E. Vesselli, S. de Gironcoli, S. Lizzit, L. Petaccia, G. Zampieri, G. Comelli and R. Rosei, N. J. Phys. **9**, 143 (2007).

[164] A. Sanchez, S. Abbet, U. Heiz, W.-D. Schneider, H. Häkkinen, R. N. Barnett and U. Landman, J. Phys. Chem. A **103** 9573 (199).

[165] B. Yoon, H. Häkkinen, U. Landman, A. S. Wörz, J.-M. Antonietti, S. Abbet, K. Judai and U. Heiz, Science **307**, 403, 2005.

[166] H. Häkkinen, S. Abbet, A. Sanchez, U. Heiz and U. Landman, Angew. Chem. Int. Ed. **42**, 1297 (2003).

[167] M. Walter and H. Häkkinen, Phys. Rev. B **72**, 205440 (2005).

[168] A. T. Bell, Science **299**, 1688 (2003).

[169] R. Schlögl and S. B. A. Hamid, Angew. Chem. Int. Ed. **43**, 1628 (2004).

[170] B. V. Reddy, S. N. Khanna and B. I. Dunlap, Phys. Rev. Lett. **70**, 3323 (1993).

[171] Y. Jinlong, F. Toigo and W. Kelin, Phys. Rev. B **50**, 7915 (1994).

[172] S. K. Nayak, S. E. Weber, P. Jena, K. Wildberger, R. Zeller, P. H. Dederichs, V. S. Stepanyuk and W. Hergert, Phys. Rev. B **56**, 8849 (1997).

[173] B. V. Reddy, S. K. Nayak, S. N. Khanna, B. K. Rao and P. Jena, Phys. Rev. B **59**, 5214 (1999).

[174] T. Futschek, M. Marsman and J. Hafner, J. Phys. Condens. Matt. **17**, 5927 (2005).

[175] C.-H. Chien, E. B.-Barojas and M. R. Pederson, Phys. Rev. B **56**, 2196 (1998).

[176] K. A. Gingerich and D. L. Cocke, J. Chem. Soc. Chem. Commun. **1**, 536 (1972).

[177] A. Endou, R. Yamauchi, M. Kubo, A. Stirling and A. Miyamoto, App. Surf. Sc. **119**, 318 (1997).

[178] A. Endou, N. Ohashi, K. Yoshizawa, S. Takami, M. Kubo, A. Miyamoto and E. Broclawik, J. Phys. Chem. B **104**, 5110 (2000).

[179] A. J. Cox, J. G. Louderback, S. E. Apsel and L. A. Bloomfield, Phys. Rev. B **49**, 12295 (1993).

[180] M. S. Ford, M. L. Anderson, M. Barrow, D. P. Woodruff, T. Drewello, P. J. Derrick, S. R. Mackenzie, Phys. Chem. Chem. Phys. **7**, 975 (2005).

[181] M. L. Anderson, M. S. Ford, P. J. Derrick, T. Drewello, D. P. Woodruff and S. R. Mackenzie, J. Phys. Chem. A **110**, 10992 (2006).

[182] D. Harding, S. R. Mackenzie and T. R. Walsh, J. Phys. Chem. B **110**, 18272 (2006).

[183] D. Loffreda, D. Simon and P. Sautet, J. Chem. Phys. **108**, 6447 (1998).

[184] Q. Ge, S.J. Jenkins and D.A. King, Chem. Phys. Lett. **327**, 125 (2000).

[185] S.J. Jenkins, Q. Ge and D.A. King, Phys. Rev. B **64**, 012413 (2001).

[186] F. Favot, A. Dal Corso and A. Baldereschi, Phys. Rev. B **63**, 115416 (2001).

[187] L. E. Cross, Ferroelectrics **76**, 241 (1987).

[188] F. Chu, I. M. Reaney and N. Setter, J. App. Phys, **77**, 1671 (1995).

[189] R. F. Service, Science **275**,1878 (1997).

[190] M. Born and J. R. Oppenheimer, Ann. Physik, **84**, 457 (1927).

[191] S. Seal and M.-I. Barton, MRS Bulletin **29**, 9 (2004).

[192] R. Pirc and R. Blinc, Phys. Rev. B **60**, 13470 (1999).

[193] V. Westphal, W. Kleemann and M. D. Glinchuk, Phys. Rev. Lett. **68**, 847 (2000).

[194] W. Cochran, Adv. Phys. **10**, 401 (1961)

[195] P. W. Anderson, Fizika Dielektrikov (ed. G. I. Skanavi), Akad. Nauk USSR, Moscow (1960).

[196] P. M. Gehring, S.-E. Park, and G. Shirane, Phys Rev. Lett. **84**, 5216 (2000).

[197] P. M. Gehring, S.-E. Park, and G. Shirane, Phys. Rev. B **63**, 224109 (2001).

[198] J. Hlinka *et al.*, Phys Rev. Lett. **91**, 107602 (2003).

[199] N. Setter and L. E. Cross, J. Appl. Phys. **51**, 4356 (1980).

[200] H.B. Krause, J.M. Cowley and J. Wheatley, Acta. Cryst. **A35** 1015 (1979).

[201] C. Perrin, N. Menguy, O. Bidault, C. Y. Zahra, A.-M. Zahra, C. Caranoni, B. Hilczer and A. Stepanov, J. Phys. Condens. Matter, **13** 10231 (2001).

[202] H. Z. Jin, J. Zhu, S. Miao, X. W. Zhang and Z. Y. Cheng, J. App. Phys **89**, 5048 (2001).

[203] H. Quian and L.A. Bursill, Int. J. of Mod. Phys. **10**, 2027 (1996).

[204] A. F. Ioffe and A. R. Regel, Prog. Semicond. **4**, 237 (1960).

[205] P. B. Allen, J. L. Feldman, J. Fabian and F. Wooten, Phil. Mag. B **79**, 1715 (1999).

[206] S. N. Taraskin and S. R. Elliot, Phys. Rev. B **61**, 12031 (2000).

[207] X. Gonze, Phys. Rev. B **55**, 10337 (1997).

[208] S. N. Taraskin and S. R. Elliot, Phys. Rev. B **61**, 12017 (2000).

[209] H. Krakauer, R. Yu, C.-Z. Wang, K. M. Rabe and U. V. Waghmare, J. Phys: Cond. Matt. **11**, 3779 (1999).

[210] M. Glinchuk, A. Morozovska and E. Eliseev, Integrated Ferroelectrics **64**, 17 (2004).